University of California
Santa Barbara

Niobium and Oxygen: A First Principles Study of Phase Stability and Solute Behavior

A dissertation submitted in partial satisfaction
of the requirements for the degree

Doctor of Philosophy
in
Materials

by

Colleen Reynolds

Committee in charge:

Professor Anton Van der Ven, Chair
Professor Tresa M. Pollock
Professor Carlos G. Levi
Professor M. Scott Shell

September 2023

The Dissertation of Colleen Reynolds is approved.

Professor Tresa M. Pollock

Professor Carlos G. Levi

Professor M. Scott Shell

Professor Anton Van der Ven, Committee Chair

August 2023

Niobium and Oxygen: A First Principles Study of Phase Stability and Solute Behavior

Colleen Reynolds

Acknowledgements

These past five years have been quite the journey. This dissertation and all that it took to get here would not have been possible without the constant help and support of so many people from all different parts of my life. First and foremost, I must acknowledge the academic support of my advisors, Professors Anton Van der Ven and Tresa Pollock, who have taught me so much and shaped my research over the years. I would also like to thank the UCSB staff, AJ Johnson, Alexandria Huddleston, Rosalind Robertson, Jennifer Thorndyke, Mike Craig, and Michelle Veal who help us graduate students navigate the day to day details of life at UCSB. Additionally, thank you to Wendy Ibsen, Frank Kinnaman, and Dotti Pak who organize so many outreach opportunities on campus and in the community which have been source of joy and inspiration. I am also particularly indebted to Fuzzy Rogers and Paul Weakliem for all the work they have done maintain the computational resources on campus.

I am eternally grateful to my research groups, both the Pollock group and the AVDV group, past and present. Not only have you always been helpful and kind, but you have become close friends and a great source of support everyday. Muna, Sesha, and Elizabeth, I will miss our afternoon walks along the bluffs and chats over coffee which have definitely kept me a little bit sane this past year.

These past five years would not have been nearly as pleasant if I had not had the dumb luck to start at the same time as the other women in my cohort. From book clubs to camping trips, weekly lunches and trivia nights, you have been possibly the best part of graduate school. My roommate Carolina, you have been an incredible friend and such a calming presence in our home. Thank you for embarking on elaborate baking projects with me and letting me talk your ear off while you are trying to knit.

It is doubtful that I would ever have set out for UCSB if it had not been for the

amazing people who had come into my life so many years before. My friends from Penn, you are a constant source of inspiration and I am so proud of us all for staying close over all of these years. So in no particular order, Bianca, Maggie, Leah, Danielle, Rowana, Ray, Brandon, Steph, Debby, Mike Citrin, Abby, Fran, Trish, Denise, and Meghan, thank you for always making time to stay in touch, with a special thank you for all those who have visited me or let me crash at your home. While on the topic of visitors, I am beyond grateful to the Jenkins family who have always been so kind and generous each time I have visited and overstayed my welcome at Tremethick.

In my previous working life, I also was lucky to make a great friend in Mary Catherine DeCristoforo who not only sent me numerous care-packages during lockdown, but is taking good care of our cat Ana. Thank you also to Brian Holloway not only for the recommendation letters without which I certainly would not be here, but also for the many pep talks and unsolicited advice which have been invaluable.

My family has played such a significant role shaping my values and ambitions throughout my life. I have been fortunate to have two loving parents, Michael and Joyce, who have instilled in me the importance of education and hard work. My older siblings, Jen, Michael, and Cara, have always been a source of inspiration, humour, and support over the years, and my nieces, Avery and Madeline, a constant source of laughter and joy. We have been far apart while I was in graduate school, but I hope that we will get to spend more time together in the coming years.

A special thanks to all the neighborhood cats, the cats I've been lent, and all my friends' pets that my friends have let me pet, especially Muna Saber's Califer and Sophie who have been excellent writing buddies, and Hazel the Cat our office manager.

And finally, Harry, there are not enough words to express how lucky I am that you are a part of my life. You are the best part of my day, everyday, and I cannot way to start the next chapter of our lives together.

Curriculum Vitæ
Colleen Reynolds

Education

2023	Ph.D. in Materials (Expected), University of California, Santa Barbara.
2014	M.S.E. in Materials Science and Engineering, University of Pennsylvania
2014	B.S.E. in Materials Science and Engineering, University of Pennsylvania

Publications

2023	M. Saber, **C. Reynolds**, T.M. Pollock, and A. Van der Ven. (2023) "Chemical and structural factors affecting the stability of Wadsley-Roth block phases." *Submitted.*
2023	**C. Reynolds**, T.M. Pollock, and A. Van der Ven. (2023) "Prediction of Nb-O phase stability and analysis of common defects in BCC Nb and vacancy ordered rocksalt NbO." *In Preparation.*
2023	**C. Reynolds**, T.M. Pollock, and A. Van der Ven. (2023) "Solute-Solute Interactions in Dilute Nb-X-O Alloys From First Principles." *In Preparation*
2023	L.T.W. Fey, L. T., **C. Reynolds**, A. Hunter, and I.J. Beyerlein. (2023). "Phase-field modeling of dislocation-interstitial interactions." *Journal of the Mechanics and Physics of Solids*, 105370.
2020	P.R. Chowdhury, **C. Reynolds**, A. Garrett, T. Feng, S.P. Adiga, and X. Ruan. (2020). "Machine learning maximized Anderson localization of phonons in aperiodic superlattices." *Nano Energy*, 69, 104428.
2019	**C.M. Reynolds**, D.N. Coar, M.C.C. Decristoforo, L.N. Egan, and J.C. Russo. Lockheed Martin Corp, 2019. AC vector magnetic anomaly detection with diamond nitrogen vacancies. U.S. Patent 10,338,162.

Abstract

Niobium and Oxygen: A First Principles Study of Phase Stability and Solute Behavior

by

Colleen Reynolds

Niobium oxides and alloys are of growing interest to both battery engineers and high temperature structural alloy designers in recent years. The niobium oxide Wadsley-Roth crystallographic shear phases are promising next generation Li-ion battery anode materials while a new class of refractory multi-principal metals alloys is of interest for extreme temperature aerospace applications. The phase stability of niobium and oxygen was originally studied during alloy development efforts in the 1950s and 1960s, but has not been recently revisited with modern first principles and statistical mechanics tools. Both niobium and other refractory metals used in these alloys can dissolve significant quantities of oxygen and readily react to form complex and often highly non-protective oxide scales. It is thus of great interest to revisit and evaluate the phase stability and defect behavior of niobium alloys and related oxides.

Throughout this work, a computational approach was applied to determine not only thermodynamic phase stability, but to illuminate the underlying structural and chemical factors which drive this behavior. From first principles and statistical mechanics, a revised phase diagram of the Nb-O system is proposed. This includes a solubility curve determined from a Bayesian cluster expansion approach which allowed the uncertainty of the solubility curve to be directly probed. We also determined a systematic way to classify and enumerate Wadsley-Roth block structures and then identified electrostatic repulsion and lattice relaxations as the key factors determining phase stability. At the other compositional extreme, the multifaceted interactions between interstitial oxygen

atoms dissolved in niobium were analyzed. Notably, closed-shell hybridization between oxygen-oxygen pairs drives strong repulsion at short distances which leads to the suppression of high energy pair clusters which persists to high temperatures. Similar closed-shell hybridization is also observed in some repulsive oxygen-solute interactions in dilute alloys, though frequently electrostatic interactions are dominant in this scenario. Finally, through first principles calculations we found that the topology of generalized stacking fault energy curves in BCC Nb are drastically altered when interstitial oxygen atoms are contained within a glide plane. These findings suggest that mechanical deformation mechanisms may be impacted by interstitial oxygen in unexpected ways.

Contents

Chapter 1

Introduction

In both structural and functional applications, many of our technologies are fundamentally limited by the properties of the materials which make them up. As we as a society strive to reduce the environmental footprint of our electrical grid and transportation sectors we seek new technologies which can improve efficiency of traditional power generation methods and power density and safety of energy storage technology. Niobium alloys and oxides are key in both of these worthy goals.

Lithium ion batteries are an essential technology for converting our power grid to renewable sources and switching to electric vehicles. In particular, finding battery materials with greater power density and faster charge rates which are also safer to operate are key to expanding the electric vehicle market. Niobium oxides, particularly the Wadsley-Roth block structures, are promising candidates for next generation battery anode materials [1, 2]. These materials have a high power density and can cycle both quickly and repeatedly, features made possible by their unique crystal structure. These niobium oxides are stable across several oxidation states and contains large tunnel features through which lithium can quickly diffuse [2]. Additionally, these oxides operate at a higher voltage than typical graphite anode which significantly reduces the risk of thermal runaway and

dangerous fires[1].

The efficiency of traditional combustion engines, used in both aerospace and utility scale power generation, are thermodynamically limited by the maximum operating temperature. This temperature is determined by the phase stability and mechanical performance of the materials they are made out of. Currently, turbine blade in the hot section of jet engines are composed of Ni superalloys which, with the help of some active cooling and thermal barrier coating, can operate at temperatures above the alloy's solidus temperatures. Clearly, new materials are needed to realized even higher peak engine temperatures.

Researchers are now pursuing a new promising class of alloys for these high temperature applications, called refractory multi-principal element alloys (RMPEAs). Traditional niobium alloys, as well as other refractory metal alloys were initially studied as part of the space race in the mid 20th century and have found uses in specialty applications such as the nozzle flaps on rockets [3]. These high melting temperature metals, often with a body-centered cubic crystal structure, have proved challenging to optimize due to manufacturing restrictions and oxidation behavior[3, 4]. In contrast, RMPEAs can with stand high temperatures, have been shown to have increased oxidation resistance, and maintain mechanical properties suited to various applications including nuclear reactor walls and turbine blades in gas combustion engines. RMPEAs consists of five or more elements which as present in near equiatomic amounts, such that there is no small number of base elements. These are the cousins of the "high entropy" alloys (HEAs) which were first reported by Ye and Cantor [5, 6].

Niobium is an essential constituent element to RMPEA alloys, due to its relatively high melting point to density ratio[7] and affordability. However, alloys containing high concentration of Nb as well as other early transition metals such as Ti, Zr, Hf, V and Nb can dissolve significant amounts of oxygen,[8, 9, 10, 11] both during manufacturing

and use. Interstitial oxygen typically causes embrittlement in refractory alloys [12]. It is therefore essential to understand, predict and control oxygen behavior and solubility in these alloys.

1.1 Overview

Over the following chapters, we will use first principle and statistical mechanics approaches to study first the phase stability of the entire Nb-O binary system. Chapter 2 presents an overview of the Nb-O system and the crystallographic phases commonly observed across the compositional range and their applications. Chapter 3 will then provide a brief discussion of the basic theory and methods which will be used through out the following chapters. Next, a study of the phase stability across the Nb-O system with a particular focus on the interstitial O-O interactions in BCC niobium and defects in the rocksalt monoxide phase will be covered in Chapter 4. Chapter 5 will then examine the underlying factors which drive phase stability in the Wadsley-Roth niobium oxides. Next, in Chapter 6 the solute-solute interactions in BCC niobium will be examine both between oxygen interstitial solutes in pure niobium, and between interstitial oxygen and substitutional alloyed elements. Lastly, a preliminary study of the impact of interstitial oxygen on deformation mechanisms in BCC Nb will be reported in Chapter 7 before some concluding remarks in Chapter 8.

1.2 Permissions and Attributions

1. The content of Chapter 4 and Appendix A is adapted from reference [13] an article in preparation for publication in *Physical Review Materials*: C. Reynolds, T.M. Pollock, and A. Van der Ven. (2023) "Prediction of Nb-O phase stability and

analysis of common defects in BCC Nb and vacancy ordered rocksalt NbO." *In Preparation.*

2. The content of Chapter 5 and Appendix B is adapted from reference [14] an article submitted for publication in *Inorganic Chemistry*: M. Saber, C. Reynolds, T.M. Pollock, and A. Van der Ven. (2023) "Chemical and structural factors affecting the stability of Wadsley-Roth block phases." *Submitted.*

3. The content of Chapter 6 and Appendix C is adapted from reference [15] an article submitted for publication in *Acta Materialia*: C. Reynolds, T.M. Pollock, and A. Van der Ven. (2023) "Solute-Solute Interactions in Dilute Nb-X-O Alloys From First Principles." *Submitted.*

4. Many of the crystal structure images throughout this work were generated with VESTA.

5. The author of this work was supported by the National Science Foundation Graduate Research Fellowship under Grant No. 2139319. .

6. We are grateful for computing resources from the National Energy Research Scientific Computing Center (NERSC), a U.S. Department of Energy Office of Science User Facility, operated under Contract No. DE-AC02-05CH11231 using NERSC award BES-ERCAP0023147.

7. This work also made of computational facilities purchased with funds from the National Science Foundation (CNS-1725797) and administered by the Center for Scientific Computing (CSC). The CSC is supported by the California NanoSystems Institute and the Materials Research Science and Engineering Center (MRSEC; NSF DMR 2308708) at UC Santa Barbara.

8. This work is also made possible by the support of the ONR BRC Program, Grant Number N00014-18-1-2392.

Chapter 2

Niobium Oxides and Alloys

Over the past century, researchers have evaluated the thermodynamic stability of phases in the niobium oxygen binary system across the full the range of compositions. The commonly excepted phase diagram in the literature (Figure 2.1) contains four main solid phases in addition to the gaseous oxygen phase that have been identified. At the niobium rich extreme pure niobium adopts a bcc crystal structure which can dissolve oxygen interstitially into octahedral sites. As oxygen concentration increases a monoxide phase forms with a cubic crystal structure related to rocksalt, but with 25% vacancies on each sublattice. Next, NbO_2 has a high temperature metallic rutile phase which undergoes a metal-insulator transition to a monoclinic phase as low temperatures. Finally, a number of different polymorphs have been observed for the highest oxidation states at the composition Nb_2O_5, though many of these could be described as belonging to the family of Wadsley-Roth crystallographic shear structures. Additionally, a number of off-stoichiometric Wadsley-Roth structures with compositions between NbO_2 and Nb_2O_5 have been observed and are sometimes included on phase diagrams[16].

In this chapter, we will discuss each of these phases, key characteristics and relevant application requirements. We will start with a discussion of the oxygen-rich Wadsley-

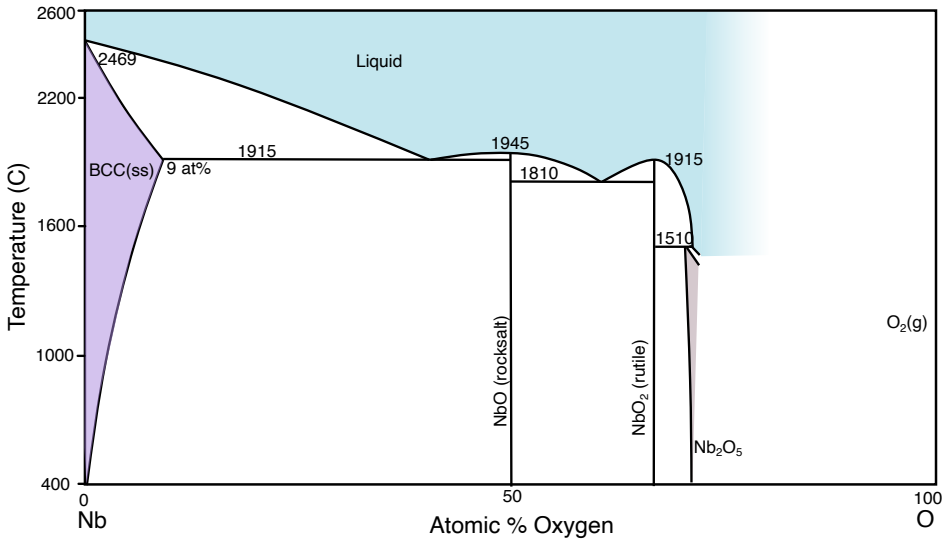

Figure 2.1: The niobium-oxygen binary phase diagram available in the literature adapted from [17, 18]

Roth phases and their role as lithium-ion battery anodes. We will then discuss the other oxide phases with increasing niobium composition. Finally we will focus on the BCC NbO_x interstitial solid solution and its relations to alloy properties.

2.1 Niobium Oxides for Lithium Ion Batteries

Many modern technologies from electric cars to the cell phone in your pocket are powered with lithium ion batteries. These devices consist of two electrodes, and anode and cathode, separated by an electrolyte material. When discharged, the lithium ions move from the anode through the electrolyte to the cathode while an electron travels through an external circuit powering a device. During charging the process is reversed. Intercalation materials are typically used as electrode, which can accommodate the additional lithium ions in the interstices of the crystal. Should the voltage of the anode becomes too low, as may occur during fast charging rates, lithium dendrites can grow into the electrolyte causing a short which can result in dangerous fires[1, 2]. Thus researchers

are motivated to find safe, fast charging anode materials, preferably with high specific capacity. Wadsley-Roth block structures have been one of the most promising class of materials studied [2].

Wadsley-Roth phases, first characterised in the mid-20th century [19, 20, 21, 22, 23, 24], are a set of crystallographic shear phases found most commonly in the Nb-O, Nb-W-O, and Ti-Nb-O systems [20, 21, 22, 23, 24] though a number of other phase with other cations have also been synthesized [25, 26, 27, 28]. They are composed of regions of corner-sharing octahedra separated by a planes of edges-sharing octahedra. These plane of edge sharing octahedra are are also called crystallographic shear planes, which refers only to the relative geometry of the crystal structure and not mechanical shear. The blocks of corner sharing octahedra may be different sizes and can tile together to generate a wide variety of related structures with different compositions and geometries.

Wadsley-Roth block phases have shown lots of promise as next generation anode materials, and have been studied as such since the 1980s [29]. As one of the primary components, niobium can undergo multiple redox events amplifying the storage capacity of the materials. Niobium remains stable in the octahedral site across multiple charge states. Furthermore, the open channels between the corner sharing octahedra provide a low barrier for diffusion resulting in fast charging and discharging kinetics. These oxides also have a higher relative voltage than the graphite alternative, making then a much safer alternative [2]. One such oxide, $TiNb_2O_7$ has even been commercialized by Toshiba for automotive applications [30]. However, between the broad geometric and compositional design space there still much room to better understand and improve these materials.

2.2 Other Stable Nb Oxides

Both NbO_2 and NbO are experimentally observed oxides of niobium and typically included on the phase diagram. The NbO_2 phase is an rutile crystal structure at high temperatures which undergoes a metal to insulator transition at lower temperature as it transforms to a related but distorted monoclinic phase at 808°C [31, 32, 33]. The NbO phase has a unique cubic crystal structure which is composed a three dimensional net of square planar Nb atoms. Alternatively, this crystal structure can be considered related to rocksalt but with 25% vacancies which are well ordered on both the metal and oxygen sublattices. [34, 35, 36]. Both of these phase only grow at very low oxygen pressures and not typically a major component of oxide scales.

2.3 The BCC Interstitial Solution

Oxygen can dissolve into BCC niobium by occupying interstitial octahedral sites (Figure 2.2). In the BCC crystal structure this site is asymmetric with one of the three major axis being shorter than the others in the ideal BCC lattice. For each niobium atom in a bcc lattice there are three interstitial octahedral sites which may have this shorter axis can be aligned with the $\hat{x}$, $\hat{y}$, or $\hat{z}$ axis of the cubic cell. Due to this asymmetry, the interstitial atom imposes a tetragonal distortion on the surrounding lattice Figure 2.2. Since the sites are occupied randomly in a dilute solution, the oxygen concentration has been linked to a volumetric expansion and increase in the lattice constant. One of the first methods used to measure oxygen solubility by measuring the lattice parameter with x-ray diffraction methods [37, 38]. When strain is applied, one of the interstitial orientations becomes preferred in what is called the Snoek effect. Internal friction measurements make use of this effect by applying an oscillating strain and measuring to effectively

measure oxygen concentration[39, 40]. However, this methods is difficult to interpret beyond the dilute limit after which multi-body interstitial interactions can complicate measurements [40, 41]. Oxygen has also been long shown to increase the hardness of niobium, so hardness tests have also been used to measure oxygen concentration [42]. Other properties measures as a proxy for oxygen concentration include electrical resistivity and electromotive force measurements [43].

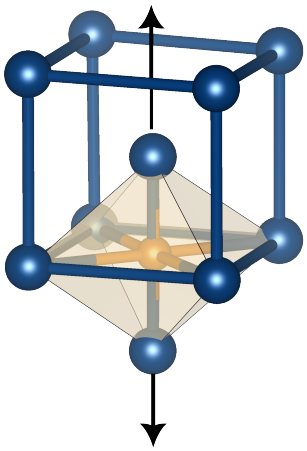

Figure 2.2: Interstitial oxygen atoms prefer asymmetric octahedrally coordinated interstitial sites in BCC niobium. This leads to a tetragonal distortion along the axis illustrated here. These octahedral sites can be found on the face center and edge center sites in the BCC conventional cell with three orthogonal orientations. Here the niobium atoms are dark blue while the interstitial oxygen atom is orange.

Over the past 75 years several attempts have been made to measure the solubility of oxygen in niobium as a function of temperature using the above mentioned methods. Massih and Perez [44] reviewed the Nb-O phase stability data in the literature for a CALPHAD study and found that some of the most successful and reliable have been by Bryant [42], Gehardt and Rothenbacher [45], and Nickerson&Altsetter [46] were considered the most accurate. Nickerson and Altsetter also proposed a model to extend their measurements to higher temperatures [46]. Their CALPHAD results closely mirror the solubility curve of the phase diagram by [18], with a maximum solubility of 9% [44].

It is worth noting that out that several of these early measurements are published in German, and therefore difficult to independently evaluate. There have also been only limited measurements at elevated temperatures.

2.4 High Temperature Structural Alloys

Traditional niobium alloys, as well as other refractory metal alloys were initially studies as part of the space race in the mid 20th century [4]. However, these high melting temperature BCC metals were challenging to optimize because alloys which had high strength at high temperatures typically proved too brittle to form into parts at lower temperatures limiting their use [4, 47, 48]. Additionally, a high oxygen solubility could also lead to embrittlement while non-protective oxide scale formation was difficult to suppress. Ultimately, the niobium alloy C103(Nb-10Hf-1Ti) is became the most commercially successful refractory alloys and was used, along with a silicide coating to prevent corrosion, for the nozzle flaps of jet engines and rockets [4, 48]. Without this coating, the alloy would rapidly oxide to form a nonprotective coating of Nb_2O_5. With the coating a mixture of Nb_2O_5 and SiO_2 form below a niobium silicide coating which oxidizes through a pesting mechanism[49].

In recent years, there has been a revival in refractory alloy development thanks to the advent of advanced manufacturing techniques such as additive manufacturing and a new class of materials called refractory multi-principal element alloys (RMPEAs)[53]. While additive manufacturing methods can help circumvent some of the limitations of traditional methods, RMPEAs open the door to a new space of alloy design. The field of RMPEAs grew as an extension of the study of multi-principal element alloys, originally termed high entropy alloys [54, 6, 53, 55], which initially focused on late transition metals such as Co, Ni, and Fe. Figure 2.3 illustrates the difference between traditional alloys

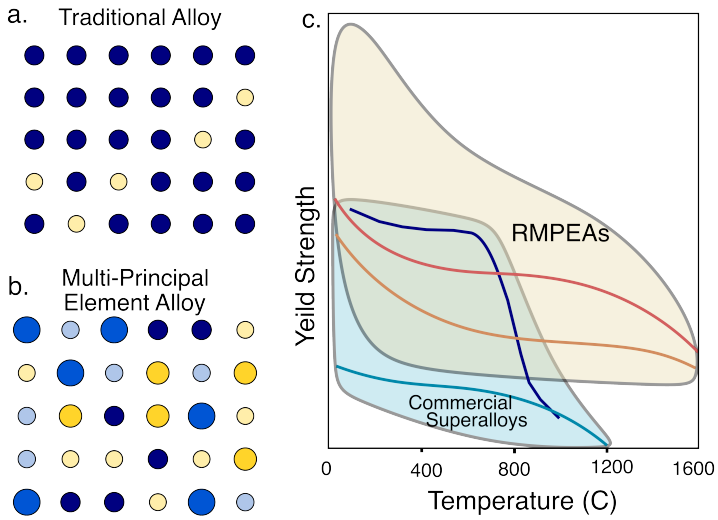

Figure 2.3: Schematics compare the disordered decorations of traditional alloys (a) and RMPEAs(b). (c)The class of RMPEA alloys have significantly higher temperature strength than state-of-the-art superalloys. This illustration of the relationship between yield strength and temperatures based on work by [50, 51, 52]

(Figure 2.3a) in which small alloy additions are randomly dispersed in a matrix which contains a small number of base elements and multi-principal element alloys (Figure 2.3b) which contain a mixture of 5 or more elements in roughly equiatomic quantities. Senkov et al took the critical step to expand the field to refractory metal alloys in 2010 [56] which had high strength at elevated temperatures. This initial study focused on alloys in the W-Nb-Ta-Mo-V family which have a high density of greater than 12 g/cm^3 [56] A year later, the W and Mo were swapped for Hf and Zr and the equiatomic TaNbHfZrTi "Senkov alloy" was introduced[50]. This formulation has high specific strength and room temperature ductility [50]. Figure 2.3c illustrates how the high temperature yield strength of these RMPEAs can greatly exceed commercial alloys used aerospace applications opening new opportunities for increasing the operating temperatures and efficiency of combustion engines. Since this initial work, hundreds of RMPEAs have been synthesized and studied, some of which form a single phase BCC solid solution like the Senkov alloy and many more multiphase materials comprised of disordered phases (BCC, HCP,

or FCC) or intermetallic phases (such as laves phases and B2)[53, 55]. More recent work has focused on multiphase materials such as BCC-B2 "refractory super alloys" [57, 55], so named for their morphology reminiscent of nickel superalloys. Niobium is an essential constituent element to RMPEA alloys due to its relatively high melting point to density ratio[7] and affordability. Alloy designers explore and refine this RMPEA compositional space with the goal of balancing a number of often conflicting criteria such as high specific strength at high temperatures, sufficient room temperature ductility, affordability, good creep properties, acceptable oxidation behavior.

However, alloys with high concentrations of Nb as well as other early transition metals such as Ti, V, Zr and Hf can dissolve significant amounts of oxygen,[8, 9, 10, 11] which can greatly impact their performance. Several refractory elements such as Nb and Ta for oxides scales which are known to be non-protective while others for oxides which volatilize (MoO_3 and WO_3)[58]. Despite this affinity for oxygen and unfavorable individual oxidation behaviors, some RMPEAs have shown improved oxidation resistance compared to traditional refractory alloys [59, 53, 60].

Even in traditional niobium alloys, the addition of other elements can change the oxygen solubility [61, 62] and oxidation rate [63]. Refractrory alloys and RMPEAs have complicated oxidation reaction behaviors which are currently the subject of ongoing research. The oxidation kinetics and reaction mechanisms can vary significantly as the composition of the alloy is altered at times significantly surpassing the performance of commercial alloys [10, 64, 53] Typically the oxidation kinetics of RMPEAs are driven by oxygen diffusion into the metal substrate where an internal oxidation occurs [64, 10, 65]. Controlling oxygen solubility, diffusion, and oxidation reactions with these materials are thus key challenges to developing RMPEAs for real-world applications.

More favorable oxidation rates in RMPEAs and related alloys are sometimes associated with a multiphase oxide scale which contain complicated oxide phases, many with

Wadsley-Roth crystal structures that have a mixture of cation species which may be disordered [10, 65, 66]. To date it has been challenging to predict the formation of these more complicated phases due to the wide range of structural and compositional complexity which must be considered. Additionally, uncertainty of the cation ordering in complex oxides which make computational evaluation difficult to rely on [64]. While the oxidation mechanisms are still a subject under study, a multi-step process has been proposed in which the simple binary oxides form rapidly first, then these react with one another and/or the metal substrate to generate more complex oxide phases [10].

Though while of great interest, the underlying mechanisms through which composition and local atomic environments impact oxygen solubility and diffusion are not yet well understood. Computational tools are needed to facilitate the study of complex oxide phase in a predictive manner that does not rely solely on the slow, expensive, and labor-intensive process of fabricating and testing each individual alloy composition. The following work will attempt to provide tools to facilitate systematic study of the complex crystal structures, by focusing the niobium oxides which form many crystal structures common to the chemical complex RMPEA oxide scales. The following work seeks to generate mechanistic insight into the factors which stabilize these complicated crystal structures and the behavior of interstitial oxygen in BCC niobium.

Chapter 3

Methods and Theoretical Background

In the following chapters, computational methods are used to investigate the formation energies, finite temperature properties, and features of the electronic structure. Density Functional Theory (DFT) is a powerful methods based on quantum mechanics which can be used to probe properties such as formation energy, lattice parameters, and electronic structure from first principles, which is to say without experimental inputs. This method is applied to determine the properties of the ground state system at 0 Kelvin. Statistical mechanics approaches such as grand canonical Monte Carlo simulations are then used to extend the results to finite temperature properties. These simulations require millions of evaluates of energies of systems consisting of thousands of atoms. DFT is computationally expensive and thus not suitable for such taxing applications. Instead, we use a cluster expansion model as a surrogate model.

Over the following chapter, the theoretical foundation of DFT will be briefly discussed. Then the cluster expansion formalism will be explained. Next, the application of statistical mechanics to calculate thermodynamic quantities will be discussed. Lastly,

the CASM software package [67], which was used to execute this workflow, is described.

3.1 Electronic Structure Theory

DFT calculations are based on the basic quantum mechanics and electron structure theory which were developed in the early 20th century. The following two sections summarize the electronic structure theory following "Electronic Structure: Basic Theory and Practical Methods" by Martin [68] and "Materials Modeling using Density Function Theory" by Giustino [69]. The ground state energy of a system is determined by the time-independent Schrödinger equation for the many-body wavefunction $\mathbf{\Psi}$.

$$E\,|\mathbf{\Psi}\rangle = \hat{H}\,|\mathbf{\Psi}\rangle \tag{3.1}$$

This is an eigenvalue problem where the eigenfunction is the many body wavefunction which describes the electronic states. The energy of the system is then defined by the expectation value of the Hamiltonian $\hat{H}$ for the given wavefunction Ψ. The Hamiltonian for a system of non-relativistic interacting electrons and nuclei can be expanded as [68]

$$\begin{aligned}\hat{H} = &-\frac{\hbar^2}{2m_e}\sum_i \nabla_i^2 - \sum_{i,I}\frac{Z_I e^2}{|\mathbf{r}_i - \mathbf{R}_I|} + \sum_{i\neq j}\frac{e^2}{|\mathbf{r}_i - \mathbf{r}_j|} \\ &-\sum_I \frac{\hbar^2}{2M_I}\nabla_I^2 + \frac{1}{2}\sum_{I\neq J}\frac{Z_I Z_J e^2}{\mathbf{R}_I - \mathbf{R}_J},\end{aligned} \tag{3.2}$$

where the r and R indicates the position of electrons and nuclei respectively and m_e and M are their masses. Compared to size and speed of the electrons in the system, the nuclei are very massive and stationary. As the mass of the nuclei M_I approximately approaches ∞, the forth term of the Hamiltonian, which represents the kinetic energy of the nuclei, becomes negligible. This is called the Born-Oppenheimer approximation [70].

The Hamiltonian can then be rewritten more compactly as

$$\hat{H} = \hat{T} + \hat{V}_{ext} + \hat{V}_{int} + E_{II} \tag{3.3}$$

The Hamiltonian thus contains terms for the kinetic energy for the electrons ($\hat{T}$), the potential energy due to the electrostatic interactions between the electrons and the fixed charged nuclei ($\hat{V_{ext}}$), the potential energy due to the interactions with other electrons($\hat{V_{int}}$), and the classical interactions between the nuclei (E_{II}) [68].

One simplification called the "Hartree" approach [68] is to treat the electrons as independent and noninteracting such that each electron could be represented by a non-interacting wavefunction ψ_i.

This method was later augmented by Fock [71] to use a Slater determinant to define the wavefunction which enforces that the wavefunctions are antisymmetric. In this way the Hamiltonian is directly solvable and can provide reasonable approximations of the energy for small molecules. Unfortunately essential quantum mechanical effects such electron correlations are entirely missing from this Hamiltonian making it unsuited for the study of extended solids.

3.2 Density Functional Theory

In 1964, Hohenberg and Kohn proposed two key theorems [72] which became the foundation of Density Functional Theory (DFT):

1. The Hamiltonian for a system can be fully determined with the specification of $V_{ext}(\mathbf{r})$ which is uniquely determined by the ground state electron density $n_0(\mathbf{r})$

2. There exists a universal functional $E[n]$ which for a given V_{ext} is at a global minimum at the ground states density $n_0(\mathbf{r})$.

From these statements we can recast the Hamiltonian as a function of electron density, greatly simplifying the problem from 3N dimensions which describe each of N electrons to 3 dimension to describe one electron density. An electron density operator can be defined as follows.

$$\hat{n}(\mathbf{r}) = \sum_{i=1,N} \delta(\mathbf{r} - \mathbf{r}_i) \tag{3.4}$$

The energy of the many body electron system can then be rewritten as

$$E[n(\mathbf{r})] = T_s[n(\mathbf{r})] + E_{ext}[n(\mathbf{r})] + E_{Hartree}[n(\mathbf{r})] + E_{XC}[n(\mathbf{r})] \tag{3.5}$$

The first three terms have already been introduced. They are the single electron kinetic energy,

$$T_s[n(\mathbf{r})] = -\frac{\hbar^2}{2m_e} \sum_i \int \psi_i^*(\mathbf{r}) \nabla^2 \psi_i(\mathbf{r}) dr \tag{3.6}$$

the energy due to Coulombic interactions with an external potential, which includes the nuclear charges

$$E_{ext}[n(r)] = \int V_{ext}(r) n(r) dr, \tag{3.7}$$

and the classical Coulomic interactions between the electrons proposed by Hartree which can be written in terms of the electron density The $\hat{V}_{int}$ term is then replaced by a Hartree potential

$$E_{Hartree} = \frac{1}{2} \int \frac{n(\mathbf{r}) n(\mathbf{r}')}{|\mathbf{r} - \mathbf{r}'|} d^3\mathbf{r} d^3\mathbf{r}' \tag{3.8}$$

The final term is called the exchange-correlation functional and it accounts for all other quantum mechanical effects which are not captured by these classical interactions[68]. This functional is simply defined as follows.

$$E_{XC}[n(\mathbf{r})] = E[n(\mathbf{r})] - T - E_{ext} - E_{Hartree} = \int d\mathbf{r} n(\mathbf{r}) \epsilon_{XC}([n], \mathbf{r}) \tag{3.9}$$

Here ϵ_{XC} is an energy density at the point r that depends on the electron density near r[68]. A variational minimization of the above equations would result in an exact value of the ground state energy and the ground state electron density. However the exact form of the exchange-correlation functional is unknown which has prompted the development of a number of approximations over the past several decades[68]. The local density approximation (LDA) uses an exchange-correlation functional which depends only on the local charge density[73]. A more exact approximation uses an additional dependence on the gradient of electron density in the $\epsilon[n(r)]$ and is called the generalized gradient approximation (GGA)[74, 75]. GGA functionals were used for the calculations in the following chapters though a number of increasingly complex approximations have been developed[68].

The most common method for minimizing the energy as a function of the electron density was proposed by Kohn and Sham in 1965 [73]. They proposed an ansatz that there exists a non-interacting system which has the same electron density as the interacting system. Since the energy of these two systems would be only a function of the electron density, finding the electron density of the simpler non-interacting system could be more straight forward. The non-interacting electrons could be described by a set of single electron wave functions and the energy of the system would thus be [73]

$$\left(-\frac{\hbar^2}{2m_e} + V_{KS}(\mathbf{r})\right)\psi_i^{KS}(\mathbf{r}) = E_i\psi_i^{KS}(\mathbf{r}) \tag{3.10}$$

$$V_{KS}(\mathbf{r}) = V_{ext}(\mathbf{r}) + V_{Hartree}(\mathbf{r}) + V_{XC}(\mathbf{r}) \tag{3.11}$$

For a system of N electrons, there would then be N simultaneous of these Kohn-Sham equations[73]. These equations, however, cannot be solved directly since the Hartree and exchange-correlation potentials are both dependant on the electron density. Instead,

an iterative self-consistent method is used. An initial guess for the electron density is proposed and the equations are solved until a convergence criterion is met [73, 68].

To simplify the computational cost of solving the Kohn-Sham equations, a pseudopotential approach is often used [68, 75]. Since the important physics is not strongly dependant on the core electrons, these electrons are not explicitly included in the calculations, but become part of the external Coulombic potential along with the atomic nuclei. This effectively reduces the number of Kohn-Sham equations which need to be solved. The planewave basis is also practically limited by a planewave cutoff energy. Practical implementations of DFT calculations often use reciprocal space integration methods which require the user to also specify a grid of points in reciprocal space called k-points [68]. Both of these user specified parameters are typically chosen by testing for a minimum energy and k-point grid which satisfies a convergence criteria.

Throughout the following work, the Vienna Ab initio Simulation Package (VASP) [76, 77] was used to perform DFT calculations. Projected Augmented Wave (PAW) [78, 79] psuedopotentials were implemented with a GGA functional parameterized by PBE [75]. In general, DFT calculations are effective and efficient for calculating the ground state energies of relatively few atoms in a periodic unit cell. Later sections will discuss other methods which can probe large systems at finite temperatures.

3.3 Ground States from First Principles

DFT calculations of the total energy of a system can be directly used to learn about the ground states in a multicomponent system. The formation energy of a crystal structure can be calculated by referencing to the total energies of reference crystals of each component (eg the total energy of BCC Nb and gaseous O_2 as calculated by DFT). The formation energies of many structures can be plotted as a function of their composition.

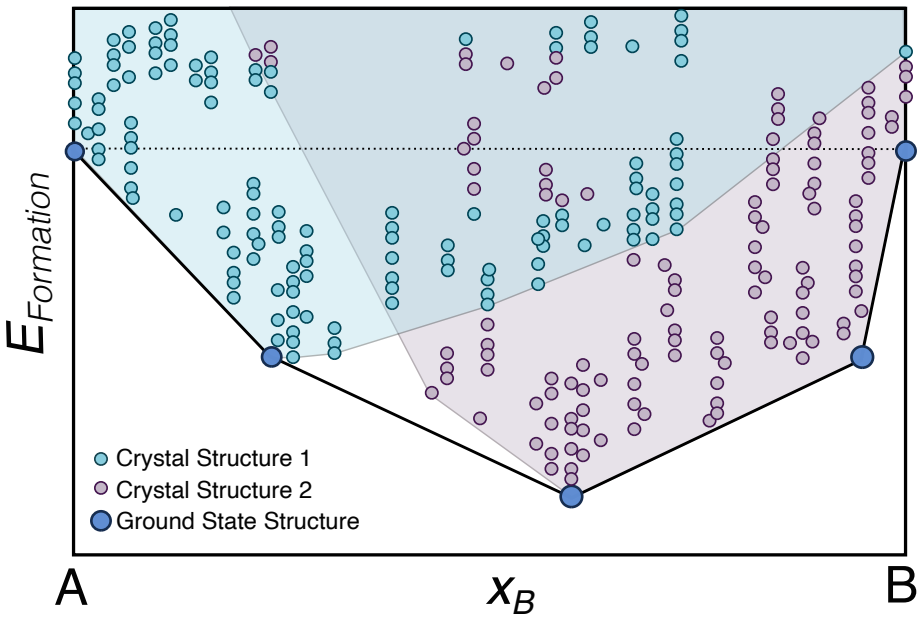

Figure 3.1: Shown above is a convex hull for a binary system of materials A and B. The dashed horizontal line is the reference energy used to calculate the formation energy of each configuration and is based on the reference states of pure A and B. Each point represents the formation energy as a function of composition for a configuration on one of two crystal structures.Local convex hulls enclose the shaded region for each crystal structure while the global convex hull is outlined in black. The ground states on the global hull include configurations on both crystal structure 1 and 2.

A convex hull for a binary system is illustrated in Figure 3.1. An envelope of the lowest energy structures can be drawn which is commonly referred to as the convex hull. The structures which intersect this convex hull are the stable ground state structures for the system at 0K. At any composition along the convex hull between vertices, a two phase equilibrium between the two structures of the surrounding vertices is predicted at 0K. If multiple crystal lattices are considered across a compositional range, their formation energies can be directly compared to determine the relative stability of each phase, as long as the formation energies were calculated relative to the same reference states. If we consider only one phase at a time, a local convex hull can be drawn around the lowest energy structures which can be described by the same crystal lattice. The point on the

local hull would be the ground states in the event that the formation of other crystal lattices was suppressed. If no systems are suppressed then the global convex hull, which is the convex envelope enclosing data from all relevant crystal systems, will intersect the true ground states of the system.

3.4 Cluster Expansion Formalism

To calculate finite temperature thermodynamic properties of the systems of interest, we have used semi-grand canonical Monte Carlo simulations. This method requires many energy evaluations of systems with thousands of atoms which is clearly beyond the capabilities of DFT, and motivates the use of a fast and accurate surrogate model for calculating the energy of a system. The cluster expansion model has been the surrogate model of choice for this work.

First described by Sanchez [80], the cluster expansion formalism is a rigorous way to systematically describe the energy of a crystal as a function of site degrees of freedom. These may be descriptions of the elemental occupation, magnetic moment, atomic displacements, or other descriptors at each crystal site [81]. To study the energy of an alloy as a function of compositional changes and atomic ordering on a crystal lattice, the site occupational degrees of freedom are most important. The alloy is first described by a parent crystal lattice which has a lattice with the vectors $\vec{l}_x, \vec{l}_y, \vec{l}_z$ and some set of basis sites are locations $\vec{b}_1, \vec{b}_2, ...\vec{b}_B$. In a binary alloy, site i could be occupied by either an atom of type A or B as represented by a site variable such as σ_i of 0 or 1. All site variables for a given configuration are denoted by the vector $\vec{\sigma}$. A cluster basis function for each cluster of sites, α can be defined according to [80]

$$\Phi_\alpha = \prod_{i \in \alpha} \sigma \tag{3.12}$$

The infinite collection of all cluster basis functions, one for each cluster of sites ina crystal, form a complete basis. Any extensive property, such as the formation energy, can then be calculated via the following [80, 82]

$$E(\vec{\sigma}) = \sum_{\alpha} V_{\alpha} \Phi_{\alpha} \tag{3.13}$$

Here the sum over α is over the set of all clusters, and V_{α} are the effective cluster interactions (ECI). Each ECI captures the contribution of a given cluster to the total extensive property of the structure. In practical applications, this sum is truncated at a finite cluster size since interactions which involve many atoms and which span a large distance tend to be weaker. The cluster expansion expression can be further reduced by taking advantage of the symmetry of the crystal. All clusters which are symmetrically equivalent should have equivalent contributions to the energy (or which ever scalar property has been expanded). By calling the set of symmetrically equivalent clusters in orbit Ω_{β}, equations 3.13 can be rewritten [80, 82]

$$E(\vec{\sigma}) = \sum_{\vec{\Omega_{\alpha}}} V_{\alpha} \sum_{\beta \in \Omega_{\alpha}} \Phi_{\beta} \tag{3.14}$$

A training set of configurations for which the formation energy has been calculated via DFT can then be use to fit a cluster expansion for the formation energy as function of site occupation. A number of linear regression methods could be applied to determine the ECI values for this model.

3.5 Thermodynamics and Statistical Mechanics

The fundamental equation of thermodynamics is a differential form of the total energy [83]

$$dU = TdS - PdV + \sum \mu_i dN_i \tag{3.15}$$

This formula indicates that the total energy is a function of each of extensive properties. However, under various circumstances it can be interesting to vary intensive properties. In this case, a Legendre transform can change this internal energy into a characteristic potential for a given boundary conditions. For instance, when temperature and pressure are constant, the characteristic potential is the Gibbs free energy, G [83].

$$G = U - TS + PV \tag{3.16}$$

In computational methods it is also possible to specify and control the chemical potential of one or more species. For each characteristic potential, we can rewrite a differential form such as in the case of the Gibbs free energy,

$$dG = -SdT + VdP + \sum_{i=1}^{n} \mu_i dN_i \tag{3.17}$$

Taking partial derivatives with respect to each natural variable of the ensemble, in this case T, P and N, we derive the equations of state [83].

$$S = -\left(\frac{\partial G}{\partial T}\right)_{P,N_i} \tag{3.18}$$

$$V = -\left(\frac{\partial G}{\partial P}\right)_{T,N_i} \tag{3.19}$$

$$\mu_i = -\left(\frac{\partial G}{\partial N_i}\right)_{T,P,N_{j\neq i}} \tag{3.20}$$

Closely related to the grand canonical ensemble is the condition where the number of unit cells is fixed and the largest number of chemical potentials are controlled, called the semi-grand canonical ensemble [84]. While this is not relevant to experimental conditions, in computational methods such as lattice based Monte Carlo methods, simulations are performed on a fixed lattice. The characteristic potential of these boundary conditions is the semi-grand canonical potential Φ. For this ensemble, the natural variable is the intensive variable which is conjugate to a parametric composition $\vec{x}$. The parametric composition can be defined generally as [84]

$$\vec{n} = \vec{n}_0 + \sum_{i=1}^{m} x_i \vec{q}_i = \vec{n}_0 + \mathbf{Q}\vec{x} \tag{3.21}$$

Here the vectors $\vec{q}_i$, which are then rewritten as $\mathbf{Q}$, span the compositional subspace and are defined in reference to the composition at a reference point $\vec{n}_0$[84]. To determine the conjugate variables to the parametric composition we can turn to the Gibbs-Duhem relation

$$G = \sum_{i=1}^{n} \mu_i N_i = N_u \vec{\mu}^T \vec{n} \tag{3.22}$$

Here the variable N_u is the number of unit cells. Combining equations 3.21 and 3.22 we obtain

$$G = N_u \vec{\mu}^T (\vec{n}_0 + \mathbf{Q}\vec{x}) = N_u (\vec{\mu}^T \vec{n}_0 + \tilde{\mu}^T \vec{x}) \tag{3.23}$$

From here it is apparent that the variable $\tilde{\mu}$ can be defined as

$$\tilde{\mu} = \mathbf{Q}^T \vec{\mu} \tag{3.24}$$

This variable $\tilde{\mu}$ is the vector of parametric chemical potentials, or exchange chemical potentials[81, 84]. These are natural variables of the semi grand canonical ensemble. The semi grand canonical free energy can then be written

$$\Phi = G - N_u \vec{\tilde{\mu}}^T \vec{x} \tag{3.25}$$

It can be useful to normalize this by the number of unit cells as follows.

$$\phi = g - \vec{\tilde{\mu}}^T \vec{x} \tag{3.26}$$

In thermodynamic equilibrium at 0 K only the lowest energy ground state of a system is observed. However, at finite temperatures, other states can be access via thermal excitations. In each state sampled by the system, some degrees of freedom of the system may be altered, and each of these unique states is called a microstate [83]. For instance, in a binary alloy system, the each site i on the lattice may be occupied by either and A or B atom as indicated by an order parameter $\sigma_i \pm 1$ and given microstate may be described by a vector of order parameters which indicate which element occupies each site. Each possible microstate $\mathbb{C}$, thus has a unique vector $\vec{\sigma}$ which describes the unique configuration. Additional degrees of freedom such as magnetic spin or displacements may also be described with variables for each site. The probability of a given state being sampled by the system at some temperate T is equal to [83]

$$P(\mathbb{C}) = \frac{e^{-\beta \Omega_c}}{Z} \tag{3.27}$$

where $\beta = \frac{1}{k_B T}$, Ω_c is the characteristic potential energy of the microstate $\mathbb{C}$, and Z is

the partition function.

$$Z = \sum_{\mathbb{C}} e^{-\beta\Omega_{\mathbb{C}}} \tag{3.28}$$

At finite temperatures, many microstates are expected to be sampled but the overall observed properties of the system are ensemble average properties. These ensemble average property of system can be calculated with the partition function

$$\langle X \rangle = \frac{1}{Z} \sum_{\mathbb{C}} X_{\mathbb{C}} e^{-\beta\Omega_{\mathbb{C}}} \tag{3.29}$$

The partition function is related to the semi-grand canonical free energy as follows

$$\beta\phi = -\ln Z \tag{3.30}$$

Grand canonical Monte Carlo can be used to calculate thermodynamic averages $\langle x \rangle$ of quantities such as potential energies and composition [**?**]. Free energy integration techniques can then be used to calculated free energies[**?**].

3.6 The CASM Project

To facilitate the first principles thermodynamics approach to study phase stability of the Nb-O system, the Clusters Approach to Statistical Mechanics (CASM) [67, 85]software package was used. This package is designed to managed the entire workflow from systematic configuration enumeration for DFT calculations, basis set enumeration and evaluation, and semi grand canonical Monte Carlo simulation. Each CASM project starts with a parent crystal structure which has a set of crystal lattice vectors and basis sites, along with a list of possible degrees of freedom which can be varied such as site occupation, magnetic moments, displacements. In one project, the parent crystal

structure was a BCC Nb primitive cell with an occupational degree of freedom on each interstitial site such that they could be occupied by either a vacancy or an oxygen atom. In another project, an ordered NbO rocksalt parent structure was used which included two sublattices, one which could be occupied by either niobium or a vacancy and one which could be occupied by either an oxygen atom or a vacancy.

Given these parent structures, CASM takes advantage of the symmetry of the crystal to systematically enumerate unique structures in small supercells [86]. There is then a built in framework of the software package to enable submission of DFT jobs with a number of commonly used DFT codes, including VASP. CASM also includes efficient methods for enumerating a basis set which can be used to describe these configurations. Once these basis sets and DFT formation energies are calculated, the user can fit the cluster expansion model. Once a set of ECI values have been determined for the cluster expansion model, CASM has an efficient grand canonical Monte Carlo code which can quickly evaluate cluster expansion at each step of the algorithm and ensure convergence given a set of user specified criteria while recording ensemble average thermodynamic properties. These properties are used to determine free energies as a function of temperature and generate a phase diagram as a function of temperature and composition.

Chapter 4

Prediction of Nb-O Phase Stability and Analysis of Common Defects in BCC Nb and Vacancy Ordered Rocksalt NbO

4.1 Introduction

High temperature structural alloys are needed to improve the efficiency of gas turbine engines used in both aerospace applications and utility scale power generation. Niobium and its alloys are of great interest, particularly in the context of refractory multi-principal element alloys (MPEAs) [87, 56, 88]. Compared to the other refractory materials, niobium has a high melting point to density ratio[7] and is relatively cheap, making it a popular and important constituent element in MPEAs. However, MPEAs containing high concentrations of early transition metals such as Ti, Zr, Hf, V and Nb tend to dissolve oxygen,[8, 9, 10, 11] both during manufacturing and use. Niobium metal exhibits

a fairly high oxygen solubility, with a maximum experimentally reported value of approximately 9 at.% oxygen [18, 17]. Interstitial oxygen can have deleterious effects on mechanical properties, alter phase stability, and lead to the formation of corrosive oxides [89, 7, 90].

Niobium oxides are also of technological interest due to their ability to rapidly intercalate Li ions. The oxygen rich niobium oxides adopt complex crystal structures known as Wadsley-Roth phases [20, 91]. The open crystal structures of Wadsley-Roth phases make them attractive anode materials for Li-ion batteries[92, 93, 29, 94, 95], where durability and charge rates of electrode materials remain limiting factors in the widespread adoption of battery-powered automobiles [96, 97, 98].

The technological importance of Nb and its oxides motivates a fundamental study of the thermodynamic and electronic properties of phases in the Nb-O binary. In this work, we report on a first principles and statistical mechanics study of the the Nb-O system. First principles calculations were used to determine stable ground states and to train cluster expansion models of the energy as a function of configurational degrees of freedom. The cluster expansion models were then applied in Monte Carlo simulations to determine phase stability at elevated temperatures and to calculate a temperature versus composition phase diagram. A Bayesian approach was used to fit the cluster expansion model[99] and to perform uncertainty quantification [100, 101] on the predicted oxygen solubility limit in BCC Nb as a function of temperature.

A high oxygen solubility limit is predicted in BCC Nb, while the vacancy ordered rocksalt NbO phase is predicted to accommodate excess oxygen at elevated temperature through the introduction of Nb vacancies. Short range repulsion between interstitial oxygen is predicted in BCC Nb leading to short range ordering at elevate temperatures. An analysis of the formation energies and the electronic structure of interstitial solutes reveals that electrostatic repulsions and closed shell bonding interactions dominate at

short range while strain mediated interactions extend to longer distances. In the vacancy ordered rocksalt NbO monoxide, the costs of introducing a niobium vacancy raises the energy of nonbonding states when bonds are broken, but does not increase antibonding state occupancy as is the case in other defects. These distinct defect preferences in the Nb-O binary are essential to understand diffusion and phase transformation pathways in Nb and its oxides. The electronic interactions that determine the stability of certain defects in the Nb-O system provide a foundation from which to understand similar interactions in other BCC and rocksalt materials.

4.2 Methods

The reader is referred to Chapter 3 for more details and background on the first principles methods used in this chapter. A combination of first principles calculations and statistical mechanics methods were applied to evaluate finite temperature thermodynamic properties and analyze electronic structure of the Nb-O binary. Density Functional Theory (DFT) calculations were performed with the VASP package [76, 77] using the Perdew, Burke, Ernzehof (PBE) exchange correlation functional [75]. The projector augmented wave method (PAW) [78, 79] pseudopotentials (Nb_sv, O) were used to describe the interactions between core and valence electrons. A plane wave cut-off energy of 575 eV was used for all calculations along with a Γ-center grid with a k-point density of 45 Å to achieve energy convergence within 1.0 meV/atom. All calculations were spin polarized and final static calculations used the tetrahedron method with Blöchl corrections. Similar DFT calculations were performed to obtain densities of states (DOS) and partial charge densities. Bader charges were calculated using the methodology of Henkelman et al[102, 103, 104, 105]. Crystal Orbital Hamilton Population (COHP) analysis was performed using the LOBSTER [106, 107, 108, 109] software package to determine the

energies and distribution of electronic states in the NbO monoxide material.

Alloy cluster expansion Hamiltonians were used to interpolate first-principles DFT energies within Monte Carlo simulations to calculate finite temperature thermodynamic properties. Alloy cluster expansions describe the dependence of the energy of a crystal on the degree of order among its chemical constituents and thereby enable a rigorous treatment of configurational excitations with Monte Carlo simulations. Cluster expansions were constructed to treat oxygen-vacancy disorder over the interstitial sites of BCC Nb and vacancy disorder over the Nb and O sublattices of the rocksalt NbO compound. The expansion coefficients of the cluster expansion Hamiltonians were sampled from a Bayesian posterior distribution that was informed by a training set of DFT energies. The Bayesian Ridge regression method implemented in scikit-learn, which follows the methodologies by Tipping[110] and McKay[111], was used to obtain a mean vector of cluster expansion coefficients and an accompanying covariance matrix to generate a Gaussian posterior distribution of cluster expansion models. The CASM software package [67] was used to enumerate structures, evaluate cluster expansion basis sets, and perform semi-grand canonical Monte Carlo simulations [85, 81]. Free energy integration techniques were applied to data generated by the semi-grand canonical Monte Carlo simulations. The phase boundaries of the temperature versus composition phase diagram were determined with a common tangent construction applied to the calculated free energies.

4.3 Results

4.3.1 Grounds States of the Nb-O Binary System

Figure 4.1a shows the formation energies for a large number of structures in the Nb-O binary as calculated with DFT-PBE. Formation energies per atom are referenced to

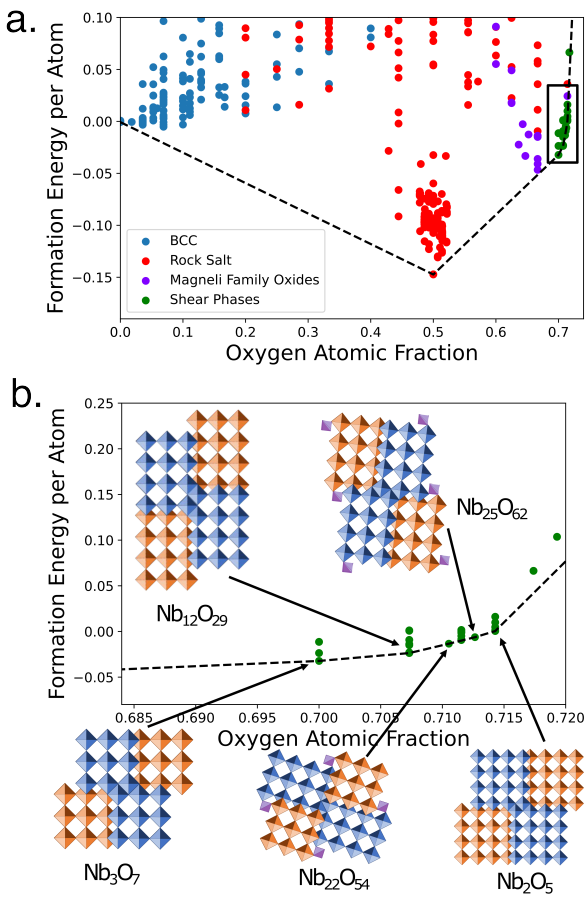

Figure 4.1: The global convex hull is shown in part a with the boxed region enlarged in part b. The structures for the Wadsley-Roth ground states are illustrated.

pure Nb and the lowest energy Nb_2O_5 structure. The structures with formation energies that reside on the lower convex hull, shown as dashed lines, correspond to the predicted ground states in the Nb-O binary. The zero-Kelvin DFT-PBE ground states include BCC Nb, a rocksalt NbO compound with an ordered arrangement of vacancies and a variety of Nb_pO_q oxides that adopt Wadsley-Roth crystal structures shown as insets in Figure 4.1(b).

Each data point in Figure 4.1 is color-coded to indicate the parent crystal structure from which it is derived. The blue points represent formation energies of different oxygen-vacancy orderings over the interstitial sites of BCC Nb. Oxygen prefers the octahedral

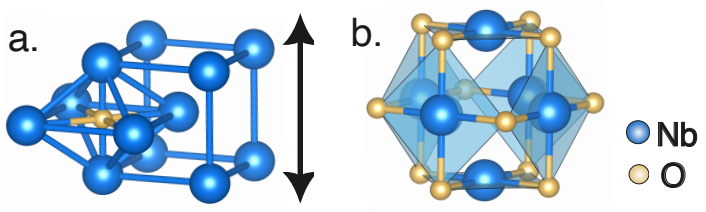

Figure 4.2: (a) Oxygen occupies the octahedral insterstitial sites of BCC Nb. (b) The NbO compound has a rocksalt crystal structure in which one fourth of both the Nb and O sublattices are vacant. The vacancies order, resulting a four-fold planar coordination of Nb by O and of O by Nb.

interstitial sites in BCC Nb, (Figure 4.2a), an asymmetric site that tends to undergo a tetragonal distortion along its shortened axis when occupied. The formation energies of 215 oxygen-vacancy orderings over the octahedral sites of BCC Nb were calculated, including 98 structures with 16, 27, or 54 Nb atoms having dilute oxygen concentrations.

The first oxide that forms upon the addition of oxygen to Nb is a vacancy ordered rocksalt phase (Figure 4.2b). One fourth of the Nb and the O sublattices of NbO are vacant, with the vacancies adopting an ordered arrangement that leads to four-fold planar coordination of the Nb by O and of O by Nb (Figure 4.2b). The red points in Figure 4.1b correspond to the formation energies of configurations in which additional vacancies were introduced on the Nb and O sublattices of NbO or a subset of the vacant sites of the NbO ground state were filled with Nb and/or oxygen.

The rutile form of NbO_2 as well as low temperature distorted rutile structure is experimentally observed to form in the Nb-O binary. Both rutile NbO_2 and its low temperature derivative, along with the closely related Magnéli structures, were also considered in this study. The formation energies of these structures are shown in purple in Figure 4.1a. None of the rutile derived structures appear on the convex hull and are, therefore, not predicted as ground states using DFT-PBE. The formation energy of the low-temperature distorted rutile NbO_2 structure is predicted to be about 5 meV/atom above the convex hull.

Many of the experimentally observed niobium oxide structures belong to the family of Wadsley-Roth shear structures. These phases are derived from a perovskite-like structure adopted by ReO_3 and consist of $n \times m \times \infty$ blocks of corner-sharing octahedra that are connected to each other along edge-sharing "shear boundaries". Algorithmic approaches have been developed to systematically enumerate a subset of Wadsley-Roth phases [14] and was used to generate Wadsley-Roth crystal structures that augment those found in the literature and the ICSD.[112] Energies of five additional structures studied by Koçer et al [92] were also included in this study. A total of five Wadsley Roth structures having stoichiometries Nb_3O_7, $Nb_{12}O_{29}$, $Nb_{25}O_{62}$, $Nb_{22}O_{54}$, and Nb_2O_5, are predicted to reside on the DFT-PBE convex hull of Figure 4.1.

4.3.2 Finite Temperature Predictions

BCC Nb can dissolve high concentrations of interstitial oxygen at elevated temperature. The vacancy order rocksalt form of NbO is also able to tolerate some degree of off-stoichiometry that is stabilized at elevated temperature by configurational entropy. We performed first-principle statistical mechanics calculations to assess the role of configurational entropy on phase stability between BCC Nb and rocksalt NbO at finite temperatures. As described in Sec. 4.2, cluster expansion Hamiltonians were used to interpolate DFT-PBE formation energies within Monte Carlo simulations. A Bayesian approach was used to sample 100 cluster expansion models describing the configurational energy of oxygen-vacancy disorder over the interstitial sites of BCC Nb. A total of 215 DFT-PBE formation energies were used as part of the likelihood distribution used to construct the posterior Bayesian distribution of cluster expansion models. A cluster expansion describing dilute defects within the vacancy ordered rocksalt NbO phase was constructed using a L2-regularized least square approach with leave one out cross-

validation. The training set used to parameterize the rocksalt cluster expansion consisted of the NbO ground state structure, FCC oxygen, FCC Nb, and $2 \times 2 \times 2$ and $3 \times 3 \times 3$ supercells of the vacancy ordered ground state structure with point and pairs defects enumerated up to a distance of 3 Å.

Figure 4.3 shows the calculated temperature versus composition phase diagram. The light blue single-phase domain corresponds to BCC Nb containing dissolved oxygen while the yellow domain corresponds to the rocksalt NbO phase. The Wadsley-Roth phases were modeled as line compounds and are stable up to high temperatures. The oxygen solubility within BCC Nb is predicted to increase substantially with increasing temperature, reaching a maximum predicted solubility of 9.7 at.% at 1915 . The vacancy ordered rocksalt NbO phase is also predicted to exhibit some degree of oxygen solubility at elevated temperatures.

Uncertainty bounds on the predicted oxygen solubility were estimated by calculating the solubility limit for each of the 100 cluster expansions sampled from the posterior Bayesian distribution of cluster expansion models for oxygen-vacancy disorder on the BCC Nb. A red region in Figure 4.3 is centered on the mean of the 100 solubility limits highlights with a range of ± 1 standard deviation. The solubility limit in blue is determined from the average solubility limit calculated from the 100 sampled cluster expansion models, while the dashed black line indicates the solubility limit based on experimental studies.[18, 17, 44]

4.3.3 Interstitial Solutes in BCC Niobium

The high solubility of oxygen in BCC Nb makes O-O pair interactions an important contribution to the thermodynamic properties of the metal. In this section, we first examine isolated oxygen interstitial atoms to generate insight about the electronic and

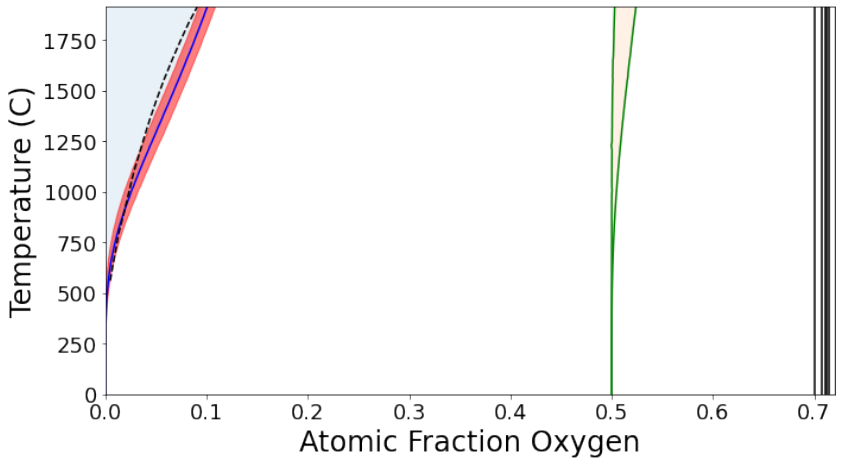

Figure 4.3: The single phase BCC Nb and vacancy ordered NbO phases are indicated by the blue and yellow regions respectively. The red region near the phase boundary between the BCC single phase region and the two phase BCC Nb and NbO region indicated the variability in the oxygen solubility predicted by the distribution of cluster expansion models in the Bayesian BCC cluster expansion. The black red line is from a phase diagram reported in the literature [18, 17, 44] which predicts a somewhat lower oxygen solubility than was predicted in this work. The five additional ground states were all treated as line compounds.

elastic interactions between the solute and the Nb matrix. We next analyze the nature of interactions between pairs of oxygen solutes as they are brought closer together.

Electronic Structure of an Isolated Interstitial

We first consider the electronic structure of an isolated solute in BCC Nb. Figure 4.4 shows the density of states (DOS) of one such oxygen in an octahedral site in a supercell of 128 BCC niobium atoms. The projected density of states show two narrow peaks at about 7.38eV below the Fermi level with very localized electronic charge densities having p character that are centered on the interstitial oxygen. These states hybridize negligibly with the Nb host, but split into two distinct peaks due to the asymmetry of the octahedral site in BCC. The higher energy peak corresponds to a p-orbital having lobes that are aligned with the short axis of the octahedral site, while the lower energy peak corresponds to the two orthogonal p-orbitals that in combination produce a ring-like charge density

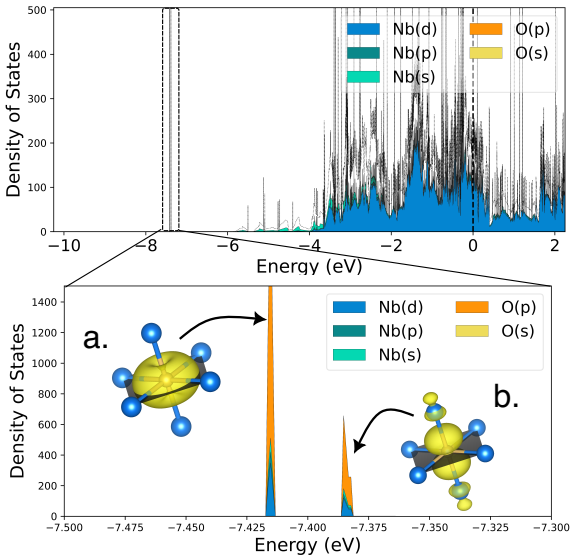

Figure 4.4: A single oxygen atom in an octahedral site in 128 atom BCC niobium supercell results in two p states at 7.38 eV below the Fermi level which are mostly non-bonding in character. The boxed region in part a. is enlarged in part b.

within the plane spanned by the two long axes of the octahedral site. Since these p-states lie far below the Fermi energy, they are filled by electrons from the niobium host. The oxygen atom is thus negatively charged while the surrounding niobium atoms acquire a slight positive charge. This is confirmed by a Bader charge calculation of a lone oxygen atom, which gains a Bader charge of -1.08 while the surrounding nearest neighbor Nb atoms lose electron density having Bader charges that range between +0.40 to +0.77.

Strain field of an Isolated Interstitial

The octahedral site in the BCC crystal structure shown in Figure 4.2a is asymmetric and imposes a tetragonal distortion on the surrounding matrix when occupied by an interstitial atom such as oxygen. The displacement field of the neighboring Nb atoms that surround an interstitial oxygen produce an overall dilational elastic dipole with tetragonal symmetry. However, the Nb atoms along the waist of the octahedron actually move slightly closer to the oxygen atom (Appendix A Figure A.1).

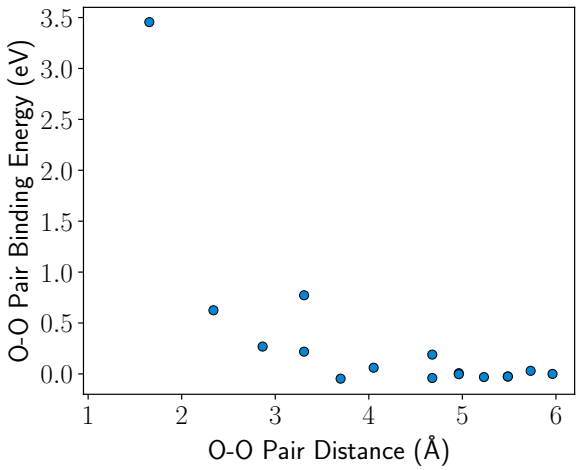

Figure 4.5: The energy of idealized pair structures are plotted as a function of the oxygen-oxygen distance and referenced to the energy of the 12th nearest neighbor pair.

Pair interactions in the absence of relaxations

We next seek to identify the dominant interactions between pairs of oxygen dissolved in BCC Nb. To isolate chemical and electronic interactions from strain interactions, we start with an analysis of the energies for the ideal BCC crystal in the absence of structural relaxations. The dependence of the energy of a pair of interstitial oxygen atoms as a function of distance was calculated using a 128 atom super cell of BCC Nb. Figure 4.5 shows the unrelaxed energy as a function of distance relative to the energy of a 12^{th} nearest neighbor O-O pair. A positive (negative) energy signifies a repulsive (attractive) interaction compared to the 12^{th} nearest neighbor pair. The results are in good agreement with similar calculations by Blanter et al [113, 114]. Figure 4.6 shows the geometries of the first six nearest neighbor pairs. The pair energies of Figure 4.5 differ negligibly from zero beyond a distance of 5 Å. They become increasingly repulsive at short distances, but the dependence on distance is not monotonic. For example, there are two symmetrically distinct fourth nearest neighbor pair configurations (Figure 4.6(d) and (e)), with oxygen separated by 3.3 Å in both unrelaxed configurations, that have

appreciably different energies.

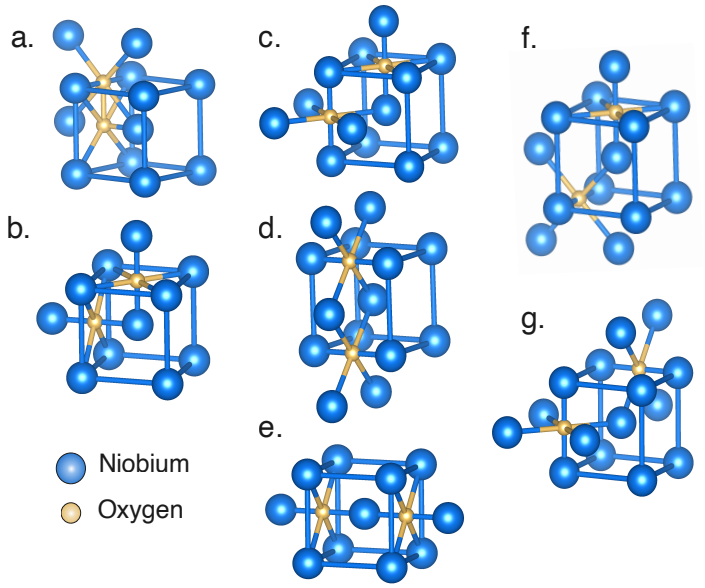

Figure 4.6: Depicted are the idealized pair clusters for the first 6 nearest neighbor where a is the first nearest neighbor pair and g is the 6th nearest neighbor. The pair clusters d and e are the two fourth nearest neighbor pairs, 4a and 4b respectively. The two fourth nearest neighbor pairs are the same distance apart, but there is a niobium atom directly between the oxygen atoms in the 4b arrangement. The pairs shown are idealized. After atomic relaxations the local atoms are displaced from these positions to reduce the stress imposed by the defect atom.

Two interactions can be identified that contribute to the unrelaxed pair energies of Figure 4.5. The first is electrostatic in nature and arises from the fact that the dissolved oxygen atoms have a local negative charge (see Section 4.3.3). Electrostatic interactions between two negatively charged species are repulsive and increase with decreasing distance. We note, however, that the electrostatic interactions between a pair of dissolved oxygen atoms in Nb should only be significant at very short distances as the itinerant electrons of the metallic Nb host will screen the negatively charged oxygen atoms at larger distances.

Electrostatic interactions between dissolved oxygen does not fully explain the variation in the pair energies of Figure 4.5, however. This is already evident when considering

the symmetrically distinct fourth-nearest-neighbor configurations, which, while having identical O-O pair distances, have very different energies. The symmetrically distinct fourth nearest neighbor configurations are shown in Figure 4.6(d) and (e). In both configurations the oxygen atoms acquire a Bader charge of -1.30. In the O-O configuration of Figure 4.6(d), the oxygen atoms are separated by two Nb atoms having Bader charges of +0.13 that are 45ff axis from the O-O pair. In the O-O configuration of Figure 4.6(e), in contrast, a single niobium atom directly separates the two oxygen atoms and acquires a significantly larger Bader charge of +0.82. Electrostatic interactions alone would favor the configuration of Figure 4.6(e) due to the presence of a positively charged Nb that blocks a direct line of sight between the pair of negatively charged oxygen. Nevertheless, the unrelaxed DFT-PBE calculations of Figure 4.5 predict that the configuration of Figure 4.6(d) has a lower energy.

A second interaction between a pair of dissolved oxygen atoms has a chemical nature and can be attributed to an unfavorable hybridization between filled atomic orbitals. This interaction has been referred to as a closed-shell repulsive interaction.[115, 116] As shown in Section 4.3.3, the valence p orbitals of oxygen atoms dissolved in BCC Nb remain very localized and hybridize negligibly with the surrounding Nb matrix. Furthermore, since the energies of the oxygen p orbitals are far below the Fermi level they are fully occupied. When a pair of dissolved oxygen atoms come close to each other, their fully occupied p orbitals will overlap and hybridize to form bonding and antibonding states. Since the oxygen p orbitals are fully occupied, however, the interaction is akin to that of two closed-shell atoms forced to form a bond: at short distances, the hybridization is unfavorable due to the filling of anti-bonding states and incurs an energetic cost.

The closed-shell interaction is clearly illustrated by examining the electronic structure of the relaxed third nearest-neighbor O-O pair configuration shown in Figure 4.7. The DOS for the relaxed structure is used for this illustration because the localized states were

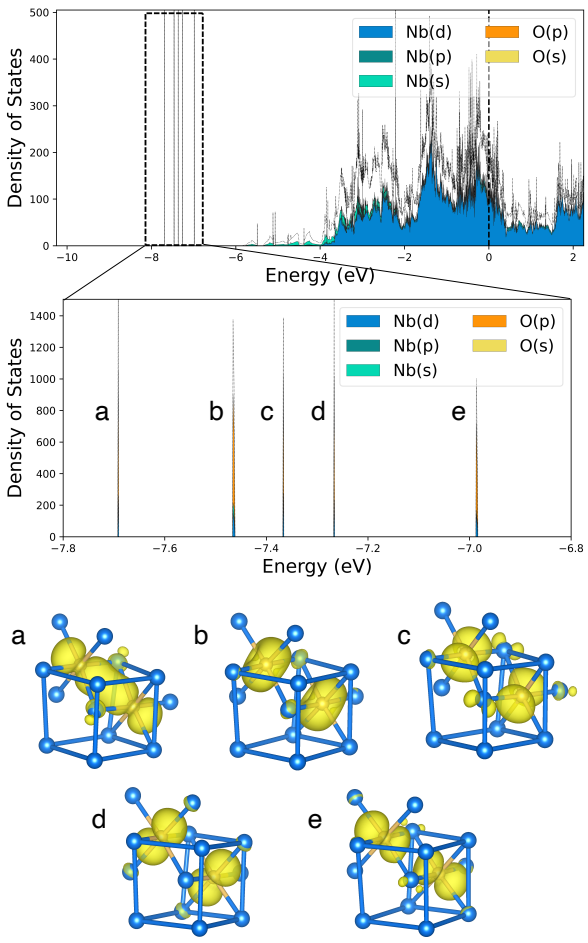

Figure 4.7: The density of states and the partial charge density of localized bands for the 3rd nearest neighbor pair are shown.

extremely narrow and difficult to sample for the idealized structure. Otherwise, the DOS are very similar in both cases. The sharp peaks in Figure 4.7, far below the Nb d-states, correspond to molecular-orbital-like states that emerge from the hybridization of the p orbitals of a pair of oxygen atoms in a third nearest neighbor configuration within a BCC Nb matrix. The peaks (a) and (e) correspond to bonding and anti-bonding orbitals, as is evident from the electronic charge densities associated with those peaks in Figure 4.7. The bonding state has a lowered energy and enhanced electronic charge density along the O-O bond, while the anti-bonding state has a higher energy with a depletion of charge

between the O-pair. The three mid-energy localized states in Figure 4.7(b), (c), and (d) are all composed of p orbitals that are perpendicular to the bond. These orbitals do not undergo any significant hybridization with each other, but do hybridize slightly with surrounding niobium atoms.

Since these states are far below the Fermi level, both the bonding and antibonding molecular orbitals are occupied and no benefit is derived from the hybridization.

The closed-shell repulsion is especially pronounced for a first-nearest-neighbor O-O configuration. In this configuration (Figure 4.6(a)), oxygen atoms occupy overlapping octahedral sites and are very close to one another. The electronic states of the oxygen atoms have a substantial spacial overlap and undergo a significant degree of hybridization that results in a low energy bonding orbital and a high energy antibonding orbital.

The degree of hybridization between oxygen p orbitals can be correlated with the separation in energy, ΔE_{hybrid}, between the bonding and antibonding states. For the third nearest neighbor pair, for example, ΔE_{hybrid} is equal to the difference in energy between the bonding peak a and the antibonding peak e in Figure 4.7. Figure 4.8(a), shows that the unrelaxed O-O pair energy, as calculated for each O-O pair configuration up to the 12^{th} nearest neighbor, is strongly correlated with ΔE_{hybrid} calculated from the electronic structure of each idealized pair configuration. The larger the degree of hybridization between oxygen p orbitals, and therefore the larger the value of ΔE_{hybrid}, the larger the repulsion between the O-O pair.

Interactions mediated by strain

A dissolved oxygen atom in BCC Nb imposes a tetragonal distortion on the surrounding matrix. The displacement fields surrounding interstitial oxygen solutes will produce a strain mediated interaction between pairs of oxygen that act in concert with purely electronic and chemical interactions. The importance and nature of strain mediated in-

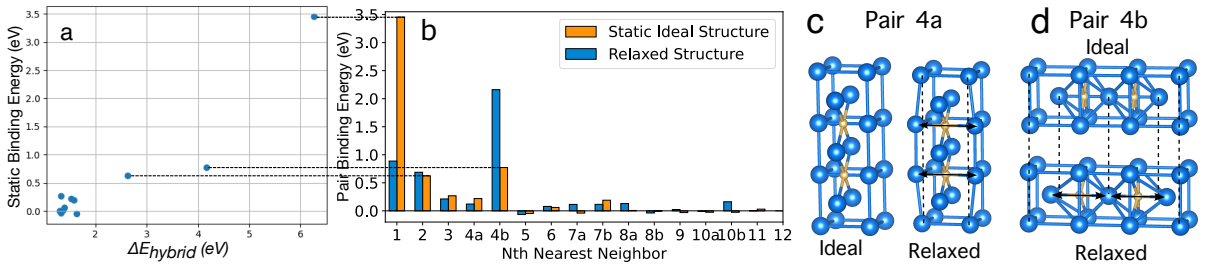

Figure 4.8: (a) The static pair binding energy is plotted as a function of ΔE_{hybrid}. The idealized and relaxed binding energies of each pair are shown in (b) with the relaxation of the 4th nearest neighbor pairs illustrated in (c) and (d)

teractions can be assessed by comparing fully relaxed pair energies to unrelaxed pair energies. This is done in Figure 4.8(b) where all O-O pair energies are again referenced to the 12^{th} nearest neighbor pair. All structures experienced a reduction in energy upon relaxation, however, those that reduced their energy more than the 12^{th} nearest neighbor pair upon relaxation have a lower binding energy after relaxation than before relaxation. The effects of relaxations are especially pronounced for the first nearest neighbor pair. In fact, the first-nearest neighbor pair configuration relaxes to a new configuration in which the oxygen atoms become tetrahedrally coordinated. The pair configurations that benefit the least from relaxations relative to the 12^{th} nearest pair have a higher binding energy after relaxation than before, as occurs for the fourth nearest neighbor of Figure 4.6(e).

The nature of the strain mediated interactions between a pair of interstitial oxygen atoms becomes evident upon close inspection of the relaxations that accompany the two symmetrically distinct 4^{th} nearest neighbor pairs. As is clear in Figure 4.8(b), the O-O pair labeled 4a has a very low energy after relaxation, while the O-O pair labeled 4b has the highest energy after relaxation. Due to the asymmetry of the BCC octahedral interstitial sites, the relaxations of the short O-Nb bonds are larger than those of the longer O-Nb bonds, resulting in a tetragonal distortion that produces an elastic dipole. The difference in pair energies between the 4a and 4b pairs highlights the importance of

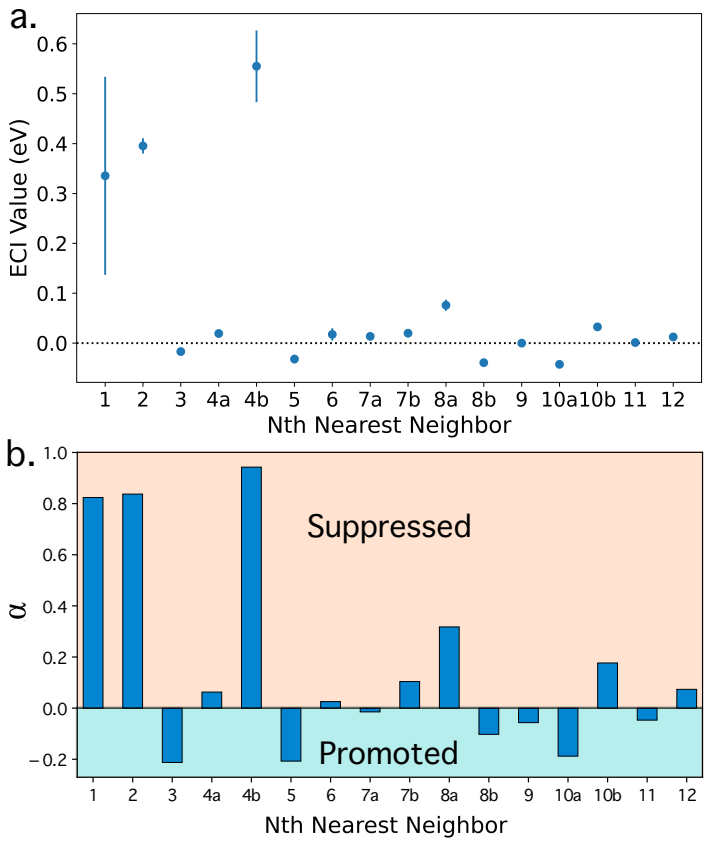

Figure 4.9: (a) The ECI parameters are plotted for the mean cluster expansion from the posterior distribution of cluster expansions with the corresponsing diagonal value of the covariance matrix plotted as the error bar. (b) The Warren-Cowley short range order parameters calculated at 1915 using grand Canonical Monte Carlo with the mean cluster expansion.

the relative orientations of the short O-Nb bonds of the interacting octahedra. For the 4a pair cluster, shown in Figure 4.8(c), the axis of their tetragonal distortions are parallel. In the relaxed structure shown in Figure 4.8(c), the elastic dipoles act in a coordinated way to distort the surrounding Nb lattice and locally achieve a more open environment for both oxygen atoms. The high energy pair cluster 4b, shown in Figure 4.8(d), has a Nb atom directly between the two oxygen atoms. The tetragonal elastic dipoles of the interacting octahedra are aligned as illustrated with the arrows in Figure 4.8(d). The two interstitial oxygen atoms apply opposing forces on the intermediate Nb atom, thereby

preventing either octahedron from fully relaxing.

Finite temperature short-range order

Since the O-O pair binding energies vary in a non-monotonic manner, it is of interest to explore the extent to which this may lead to short range order. Warren-Cowley short range order (SRO) parameters[117] were calculated using grand canonical Monte Carlo. For a given pair cluster i, The SRO parameter α_i for a particular pair cluster, i, is defined as

$$\alpha_i = 1 - \frac{p_i}{m_O^2} \tag{4.1}$$

where p_i is the probability that both sites of pair cluster i are simultaneously occupied by oxygen. The m_O^2 appearing in the denominator is the square of the fraction of interstitial sites that are occupied by an oxygen atom and is equal to the probability of an O-O pair for a random distribution of oxygen, in the absence of any short-range order.

When α_i is positive (negative), the pair cluster is less (more) likely to be observed relative to a random mixture of oxygen over the interstitial sites. The ECI values for the pair correlations used in the Monte Carlo simulation are plotted in Figure 4.9(a) which prove to be a good predictor of the short range order parameters. Figure 4.9(b) shows the values of α_i at 1915^{o}C from a Monte Carlo pass at the maximum solubility. Pairs 1, 2, and 4b have very large and positive order parameters, exceeding a value of 0.80, signifying very low probabilities that these O-O pairs are sampled at elevated temperature. Moderately negative order parameters are predicted for the 3^{rd}, 5^{th} and 10ath O-O pairs, signifying a slight preference for these clusters than would be expected for a random mixture of oxygen over the octahedral interstitial sites of BCC Nb.

4.3.4 Point Defects in Niobium Monoxide

The NbO crystal structure is a vacancy ordered rocksalt (Figure 4.2b) in which one fourth of both the Nb and O sublattices are vacant. This generates a network of Nb (O) atoms that are each coordinated by four O (Nb) atoms in a square planar geometry. There are four possible point defects when excluding anti-site defects: either additional vacancies can be created on each sublattice, or the existing vacancies on the Nb (O) sublattice can be filled by Nb (O). These defects can result in configurational disorder and lead to some degree of off-stoichiometry of the oxide compound.

Point Defect Preference in Rocksalt

The predicted phase diagram in Figure 4.3 shows some oxygen solubility in the NbO monoxide phase at elevated temperatures. The ground state NbO structure contains a high concentration (25%) of vacancies on both the Nb and O sublattices, and therefore can accommodate additional oxygen by either filling vacancies on the oxygen sublattice or by creating additional Nb vacancies. Figure 4.10 shows the sublattice concentrations within rocksalt NbO as a function of the overall oxygen concentration at a 1917^{o}C as calculated with Monte Carlo simulations applied to the cluster expansion of the rocksalt phase. This temperature is near the solidus line. Both the Nb and O sublattices have an occupancy of 0.75 at the stoichiometric composition NbO, coinciding with an oxygen atom fraction of 0.5. In the region between the two dotted lines, where the vacancy ordered rock salt is thermodynamically stable, the concentration of the Nb sublattice decreases with increasing oxygen concentration, indicating a clear preference for additional Nb vacancies when the compound becomes oxygen rich. In contrast, the concentration on the oxygen sublattice remains unchanged.

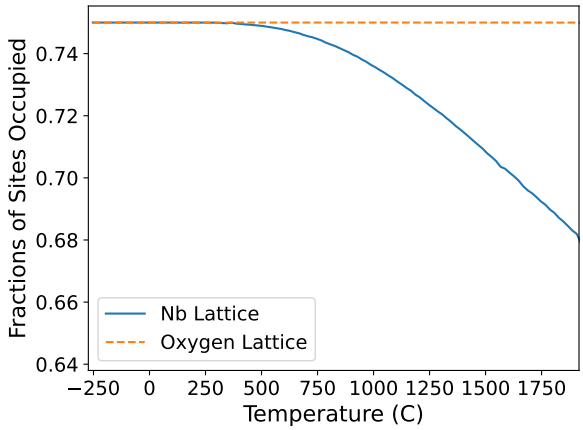

Figure 4.10: Plotted above are the sublattice occupancy for the Nb and oxygen sublattices in NbO observed in Monte Carlo calculations as the oxygen composition increases at a 1917 , a high temperature near the solidus. While the oxygen sublattice retains its 75% occupancy, the niobium sublattice occupancy drops indicating an accumulation of additional vacancies. Regions in grey are beyond the range of the rocksalt phase stability

Electronic Structure Analysis of the NbO Ground State

Before examining the bonding interactions that are altered in the presence of defects, we first describe the electronic structure of the pristine vacancy ordered NbO ground state. Similar analyses have been published previously [118, 35, 36, 34, 119], with Burdett and Hughbanks [118] emphasizing the importance of d-p π bonding between oxygen and niobium and d-d σ and π bonding between Nb-Nb pairs. Crystal Orbital Hamilton Population (COHP) analysis was performed using the software package LOBSTER [106, 107, 108, 109] to determine the energies and distribution of electronic states from Nb-Nb and Nb-O interactions in this structure.

First, the electronic structure of Nb-O bonds is examined. Figure 4.11 shows the five types of Nb-O bonding interactions allowed by the square planar symmetry in the vacancy ordered rocksalt NbO structure. The total -COHP of both Nb-O and Nb-Nb bonds is shown as a dashed line in each plot in Figure 4.11. The filled light blue states in the -COHP plots of Figure 4.11 indicate electronic states arising from the hybridization

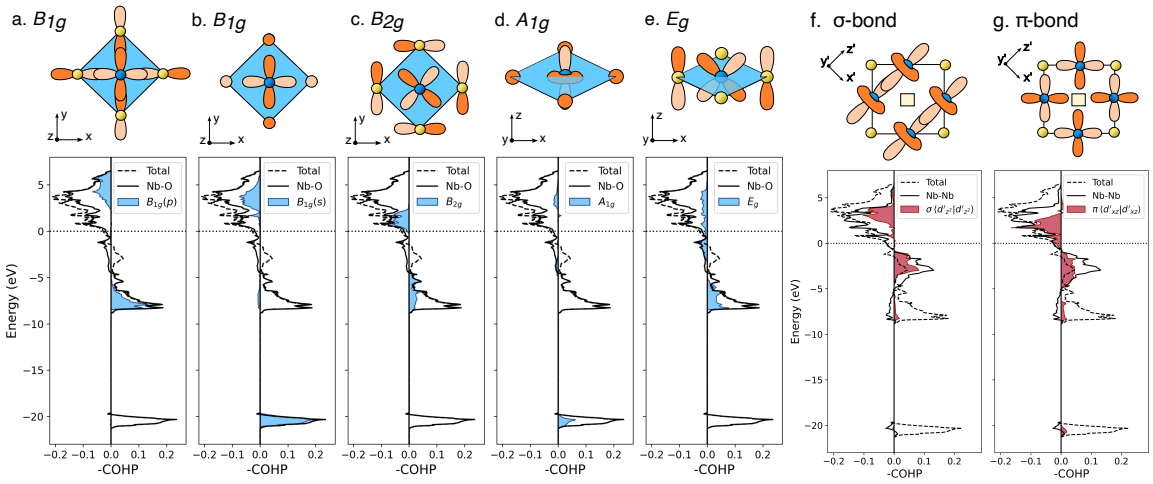

Figure 4.11: In each of the above plots, the total -COHP of the niobium-oxygen interactions are shown with a black line, the filled light blue region indicate the contribution from orbitals of a given symmetry in the square planar NbO crystal structure, and the total -COHP for the structure is shown with a dashed line. Above each plot is an illustration of the orbitals involved in the interaction. In a, b, and c the relevant orbitals are all located in the plane of oxygen whereas in d and e the orbitals involved extend out of the plane of oxygen. The gold circles at the corners of the square indicate oxygen atoms while the blue circle in the center represents the niobium atom. (g-f) The Nb-Nb interactions are also plotted as filled red states. Above each plot, a {020} slice of the NbO unit cell is shown with the rotated orbitals involved in each the Nb-Nbσ-bond (f) and π-bond (g).

of the depicted orbitals, where a positive density of states is a bonding interaction and a negative density of states is an antibonding interaction. The first two bonding interactions have a B_{1g} type symmetry and are comprised of strong σ bonds between the Nb $d_{x^2-y^2}$ and either oxygen p_x and p_y or oxygen s orbitals, all contained within the plane of atoms as shown in Figure 4.11a and b, respectively. The interactions have bonding states far below the Fermi level while the corresponding antibonding states are pushed far above the Fermi level and thus are unoccupied.

Figure 4.11c, shows a π bonding interaction with B_{2g} symmetry between niobium d_{xy} orbital and oxygen p_x and p_y orbitals contained within the plane of Nb and O atoms. Although the oxygen p-orbitals point into the neighboring vacancy, they are able to π bond with the d_{xy} of the central niobium. This overlap is weaker than the σ bond of

Figure 4.11a, as manifested by a less significant energetic splitting of the bonding and antibonding states in blue in 4.11c. The antibonding states for this interaction lie just above the Fermi level.

Continuing to Figure 4.11d, the orbitals with A_{1g} symmetry, the niobium $d_{3z^2-r^2}$ and oxygen s orbitals are mostly non-bonding in character.

The final niobium-oxygen bond consists of oxygen p_z orbitals overlapping with niobium d_{xz} or d_{yz} one of which is illustrated in Figure 4.11e. There are two instances of this type of interaction which has E_g symmetry. This orbital overlap is once again a π bond though it has even weaker splitting that the B_{2g} state. The antibonding orbital is only slightly higher in energy than the bonding orbital and spans a wider energy range. Since these states straddle the Fermi level they must be partially occupied incurring some energetic cost.

Next, the Nb-Nb interactions are examined using a similar approach. The niobium $d_{xz(yz)}$ orbital which points directly at neighboring niobium atoms, and niobium $d_{3z^2-r^2}$ orbital which points towards the oxygen vacancy, both play an important role in metal-metal bonding. Since the vector between niobium atoms is at a 45° angle from the Cartesian coordinate system we have defined so far, it is more intuitive to study the -COHP of the Nb-Nb interactions with a rotated basis set [120] of atomic orbitals (Support Information Figure S3) . With the rotated basis, the σ bonding and antibonding states can be entirely described by the $\langle d'_{3z^2-r^2}|d'_{3z^2-r^2}\rangle$ interaction (Figure 4.11f). The σ bonding states are near but below the Fermi level while the antibonding states are above the Fermi level and are unoccupied. According to Burdett and Hughbanks[118], this σ interaction is largely composed of d_{xz} orbitals in the original coordinate system, though there are some contributions from other interactions.

With this rotated basis, significant Nb d-d π bonding and antibonding states can be entirely described by the $\langle d'_{xz}|d'_{xz}\rangle$ interaction (Figure 4.11g). For the π bond, the bonding

state and lower edge of the antibonding states are below the Fermi level. There are also some contributions from other interactions such as the $\langle d_{yz}|d_{yz}\rangle$, which are parallel orbitals. Both Nb-Nb bonding states make up significant electron density below the Fermi level, overcoming the antibonding Nb-O states and resulting in a bonding character for the total -COHP until 1.45 eV below the Fermi level, as indicated by the dashed line in Figure 4.11. Prior work has shown that this shift of Nb d-orbital electron density from antibonding(nonbonding) $\langle$Nb $d_{xz(yz)}|$O$p_z\rangle$ ($\langle$Nb $d_{3z^2-r^2}|$O$s\rangle$) states into favorable Nb-Nb σ (π) bonding states stabilizes the NbO vacancy ordered structure compared to the ideal rocksalt [118].

Thus, there are three features of the electronic structure which lead to the stabilization of the vacancy ordered NbO structure:

- **Unfavorable:** Nb d_{xz}-O p_z π bonding is somewhat unfavorable due to a subset of anti-bonding states that are below the Fermi level. The vacancy ordered structure reduces these interactions.

- **Favorable:** Nb-Nb σ and π have a stabilizing effect and span the space left by oxygen vacancies, promoting their formation.

- **Favorable:** The σ Nb-O bonding has a stabilizing effect which prevents larger numbers of oxygen or Nb vacancies from forming.

Electronic Structure Analysis of the NbO Defects

This understanding of the NbO ground state informs a subsequent examination of the electronic structure of different defects in NbO. According to Figure S2 in the Appendix A Figure A.2, vacancy generation is less costly than the addition of atoms into the vacancy ordered NbO crystal, with the highest energy point defect consisting of an oxygen atom filling a vacancy.

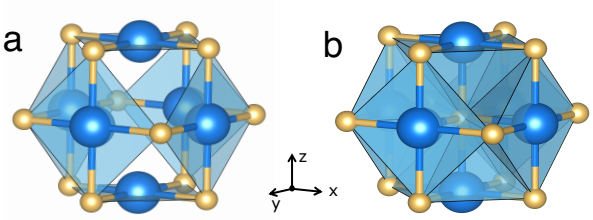

Figure 4.12: Part a shows the idealized NbO crystal structure where the blue spheres represent niobium atoms and the small yellow one s are oxygen atoms. On the right (part b) is an idealized NbO crystal structure with an additional oxygen atom filling a vacancy.

First, this highest energy defect, the addition of an oxygen atom, is studied. Compared to the the pristine NbO structure, the extra oxygen atom fills a vacant site that is octahedrally coordinated by Nb (Figure 4.12), changing the coordination environments of the surrounding six niobium atoms from a square planar symmetry to that of a square pyramid.

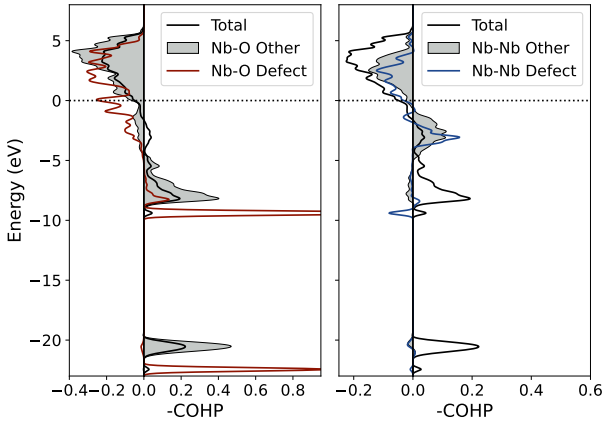

Figure 4.13: Plotted are the -COHP for the NbO structure with an additional oxygen atom normalized per bond. On the left, the Nb-O bonds near the defect are compared to the rest of the Nb-O bonds in idealized 2x2x2 supercell. On the right, the Nb-Nb bonds near the oxygen defect is compared to the rest of the Nb-Nb bond. The energy is referenced to the Fermi level.

The calculated -COHP for the the Nb-O and Nb-Nb bonding interactions in a $2 \times 2 \times 2$ idealized supercell with an additional oxygen atom are shown in Figure 4.13. In Figure 4.13a, the red curve which represents the bonds between the oxygen defect atom

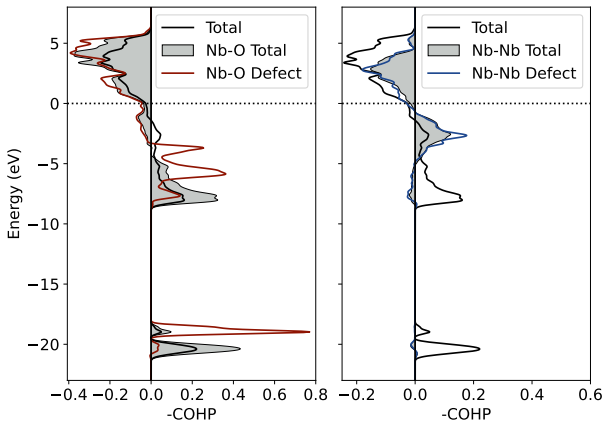

Figure 4.14: Plotted are the -COHP, normalized per bond, for the NbO structure with an additional Nb vacancy. On the left, the Nb-O bonds near the defect are compared to the average Nb-O bonds in idealized 2x2x2 supercell. On the right, the Nb-Nb bonds near the defect are compared to the average Nb-Nb bond. The energy is referenced to the Fermi level.

and surrounding Nb atoms is significantly different from the rest of the Nb-O bonds in the structure, which are shown in grey. Lower energy isolated states which would stabilize the defect, correspond to the σ bonds between the additional oxygen atom and the surrounding oxygen similar to those in Figure 4.11a and b. However there is a significant addition of antibonding states near and just below there Fermi level. From Figure 4.11c and e, we see that the antibonding Nb-O states near the Fermi level are typically composed of π bonding between the $d_{xy,xz,yz}$ orbitals and oxygen p orbitals. This is verified by a project DOS plot in the Appendix A (Figure A.4), where a lower energy from the two peaks includes contributions from the Nb $d_{xz,yz}$ orbitals which corresponds to enhancement of the antibonding Nb-O π bonds examined in Figure 4.11(e). The peak at the Fermi level in the Figure 4.13(a) also includes contributions from the Nb d_{xy} orbital according to Figure A.4. This verifies that there is additional filling of the antibonding Nb-O π bonds seen the Figure 4.11(c). The oxygen defect atom has enhanced the Nb-O π interactions, pulling the antibonding states below the Fermi level, which has a destabilizing effect.

In Figure 4.13b the Nb-Nb bonds adjacent to the oxygen atom defect are compared to the the rest of the Nb-Nb bonds in the structure. These bonds are disrupted, with a lower overall density. Due to the intervening oxygen atom, electron density from the $d_{3z^2-x^2}$ and $d_{xz(yz)}$ orbitals is shifted from the favorable Nb-Nb bonds into the Nb-O π bonds discussed in the previous paragraph. Thus the additional oxygen atom increases Nb-O hybridization resulting in the occupation of antibonding orbitals while also mildly disrupting the neighboring Nb-Nb bonding. The occupation of these antibonding states are extremely costly and destabilized this defect.

This analysis can be contrasted to the effect of a niobium vacancy, the lowest energy point defect (Appendix A Figure S2). The -COHP of the Nb vacancy defect in a a similar idealized $2 \times 2 \times 2$ NbO supercell is shown in Figure 4.14. In Figure 4.14a, the red curve representing Nb-O bonds involving oxygen p-orbitals which points into the new vacancy is compared to the average Nb-O bonds in the overall structure in grey. The oxygen p-orbitals still participate in bonding with other surrounding Nb orbitals but have dangling bonds facing the vacancy. The energy of bonding states, which correspond to the σ bonds in Figure 4.13a and b, are thus raised and broadened in energy near the defect, however no new antibonding interactions are added. In Figure 4.14b, the Nb-Nb bonds of the surrounding Nb are also relatively unchanged compared to the average Nb-Nb bonds in the structure. Since -COHP analysis cannot probe non-bonding states directly, these Nb-Nb defect states instead correspond to any Nb-Nb bonds which involve one atom that would have bonded with the missing Nb atom. In contrast to the Nb-O bonds which are raised in energy when the neighboring Nb atoms is absent, the Nb-Nb bonds are relatively unperturbed. However, there would be fewer present in the structure lowering their stabilizing contribution to the overall electronic structure.

The raised energy of Nb-O bonds contributes to the defect energy but is clearly less costly than the additional antibonding interaction seen in the oxygen atom defect.

When either a niobium or oxygen atom are added into the NbO structure, an octahedral site is filled creating six new nearest neighbor Nb-O pairs Meanwhile, when an additional vacancy is generated on either sublattice, bonds are broken with four surrounding nearest neighbor atoms of the other species. Thus, the destabilizing effects of an additional atom on surrounding Nb-O bonds have a 6-fold impact on the defect energy, while the destabilizing impact on surrounding bonds of Nb vacancy have only a 4-fold impact on the energy of the structure. This results in both vacancy generating defects tending to have a lower energy than the corresponding vacancy filling defects (Appendix A Figure S2)

4.4 Discussion

Through first principles calculations we have predicted eight ground states in the Nb-O binary system which include four off-stoichiometric Wadsley-Roth phases, which were previously not considered ground states. We used a statistical mechanics approach to predict a finite temperature phase diagram for the NbO system. Our predictions suggest oxygen solubility in both the BCC interstitial solution and the ordered rocksalt monoxide phase at elevated temperatures. The Bayesian cluster expansion method used to describe the configurational energy of interstitial oxygen in BCC Nb system enabled an assessment of the uncertainty of the predicted oxygen solubility limit in BCC Nb due to numerical errors on the DFT training data and errors due to cluster expansion truncation. The experimentally predicted solubility limit is about a standard deviation below the computationally predicted solubility limit. Notably, vibrational excitations are excluded from our analysis and could impact the solubility limit [121, 122, 123].

The most frequently cited Nb-O phase diagram proposed by Okamoto in 1990 [18, 17, 124] depicts the solubility of interstitial oxygen in BCC niobium along side three line

compounds, NbO, NbO_2, and Nb_2O_5. There is a notable absence of additional oxide phases between NbO_2 and Nb_2O_5. A study by Naito et al. [16] attempted to address this compositional range by detailing the phase diagram between NbO_2 and Nb_2O_5. The solubility curve proposed by Okamoto et al [18] shown in Figure 4.3, is motivated by several conflicting solubility curves measured in the 1960s [42, 125, 38, 45] and an empirically fit models [46]. However, these studies contained very few measurements at high temperatures. The solubility curve has not been revisited in recent experimental studies. CALPHAD studies [126, 127, 44] build upon the same early measurements, the Zircobase database [128], and rely on a private communication from Dupin and Ansara [129]. No first principles prediction of the full binary system has been performed to date.

We have demonstrated that some short range ordering of interstitial atoms occurs at high oxygen concentrations despite high temperatures. The high energetic costs of certain O-O pairs manifests as a significant suppression of these pairs in thermal equilibrium at elevated temperatures. While some of the pair binding energies can certainly be attributed to strain mediated effects and electrostatic repulsion, in many of the shorter range pairs closed-shelled repulsion plays a significant role. These unfavorable electronic interactions are the result of filling both bonding and antibonding orbitals. The short range ordering of O-O pairs may play a significant role in the diffusion and mechanical properties in niobium and other BCC interstitial solutions.

Lastly, an in-depth analysis of the electronic structure of point defects in the NbO monoxide structure was performed. The additional oxygen atom defect causes Nb-O $\langle d_{xy,xz,yx} | p_{x,y,z} \rangle$ π antibonding orbitals to be pulled below the Fermi level and occupied while disrupting favorable Nb-Nb σ and π bonding interactions, resulting in a significant energetic penalty. For the vacancy generating defects, dangling bonds are created which raise the energy of neighboring NbO bonding interactions. However, since antibonding states are not added and there is minimal impact on the Nb-Nb σ and π bonding in-

teractions, these defects are less costly. Furthermore, defects which create additional vacancies raise the energy of fewer NbO interactions than the additional atoms making them less costly to generate than defects that fill vacancies.

Short range ordering of interstitial oxygen solutes may lead to a depression in solubility in the models solid solution. In the predicted phase diagram (Figure 4.3), the predicted oxygen solubility increases quickly at moderate temperatures, but at higher temperatures it because challenging to dissolve larger amounts of oxygen. This is likely related to short range order effects becoming more significant above about 5% and reducing the entropic benefit of dissolving additional oxygen. Since certain oxygen configurations are promoted by the short range ordering, they may play a role in phase transformations in BCC alloys. For instance when niobium alloyed with HCP elements, a BCC-HCP phase transformation is sometimes observed in parts of the matrix resulting in a second phase [130]. This phase transformation may be promoted by the elastic dipole of oxygen interstitial solutes and particular arrangements of these solutes may lower the energy barrier along the Burgers path. Future work could calculate the energy barrier along this path as a function of oxygen concentration and configurations.

4.5 Conclusion

The thermodynamic behavior of the Nb-O binary system has been evaluated from eight predicted 0-K ground states to finite temperature where off-stoichiometry is predicted in the BCC and monoxide phases. We have highlighted the short range electronic interactions and long range elastic interactions which result in stabilized or destabilized O-O pair configurations. These diverse O-O pair interactions lead to short range order of interstitial oxygen in BCC Nb which persists to high temperatures and without an imposed strain. This lays a foundation for interpreting the behavior of interstitial de-

fects in other BCC materials including newly developed BCC refractory multi-principle element alloys. Analysis the electronic structure of defects in the vacancy ordered NbO rocksalt also sheds light on the interactions which stabilize the Nb vacancy defect over all others. These findings may extend beyond defects in the niobium monoxide to other rocksalt monoxide materials. Understanding the behaviors of point defects in both the BCC metals and vacancy ordered rocksalt is essential for studying diffusion, oxidation, and phase transformation pathways.

Chapter 5

The Niobium Oxide Wadsley Roth Block Phases

The electrification of vehicles and high-power electronics requires the development of battery electrodes that can sustain fast charging rates and high power densities after many charging cycles. An especially promising class of materials to serve as high power anodes in Li-ion batteries are the Wadsley-Roth block phases.[131, 132, 133, 134, 135, 136, 137, 93, 138, 139, 140, 94, 95] Also referred to as crystallographic shear structures, the Wadsley-Roth crystal structures are adopted by early transition metal oxides and constitute a large family of phases that can intercalate Li at high rates. Their structures can accommodate Li over multiple redox couples and their crystallographic flexibility makes it possible to tune their structure through alloying. While there are several Nb-oxides that form Wadsley-Roth block phases,[141, 142, 143, 144, 145, 146, 147, 148] many more have been synthesized by combining different early transition metals such as Nb, Ti, W and Mo.[20, 22, 21, 23, 24, 149, 150, 151, 152, 153, 154, 155, 156, 157, 158] For example, $TiNb_2O_7$, which has already been commercialized as an anode material, exhibits reversible capacities up to 341mAh/g and high reversible charge rates [139, 136,

159]. Other titanium-niobates such as $TiNb_{24}O_{62}$ [160] and $Ti_2Nb_{10}O_{29}$ [161] also exhibit high rate capabilities. Recent work by Griffith et al.[93] has demonstrated high rate capabilities in Wadsley-Roth phases containing different mixtures of Nb and W.

Wadsley-Roth phases are also important for refractory metal alloys [4, 130] as they can form as part of their oxide scales. There is currently much interest in the development of multi-principal element (MPE) structural alloys made of early transition metals such as Ti, Zr, Hf, V, Nb, Ta, Cr, Mo and W for high temperature structural applications.[56, 55] Structural alloys for extreme environments require protective and passivating oxide scales such as Al_2O_3.[162, 163, 164, 165, 166, 167] The formation of desirable oxide scales requires a careful tuning of the alloy composition that is guided by a comprehensive characterization of oxide phase stability as a function of oxygen partial pressure and base metal chemical potentials.[124] The flexibility of Wadsley-Roth phases to accommodate multiple early transition metals makes them important oxidation products when refractory MPE alloys are exposed to extreme oxidizing environments.

In this chapter, we investigate the structural diversity of Wadsley-Roth phases and identify chemical and crystallographic factors that determine phase stability among the many possible structural variants. We develop approaches to systematically enumerate Wadsley-Roth phases and extend the naming scheme proposed by Cava[29] to enable a more precise specification of each Wadsley-Roth crystal structure. We next explore the crystallographic features that make some Wadsley-Roth phases more stable than others and find that stable Wadsley-Roth phases minimize the number of edge-sharing octahedra. The flexibility of the metal-oxygen octahedra to undergo structural distortions play a secondary role in determining the relative stability among different Wadsley-Roth crystal structures.

5.1 Methods

The reader is referred to Chapter 3 for more details and background on the first principles methods used in this chapter. Density Functional Theory (DFT) calculations were performed with the Vienna ab initio simulation package (VASP)[76, 77, 168, 169] . The projector augmented wave (PAW)[78, 79] method was used to treat interactions between valence and core electrons. All calculations were performed within the generalized gradient approximation (GGA) as parameterized by Perdew, Burke, and Ernzerhof (PBE).[75] A 575 eV plane wave energy cutoff and a Γ-centered k-point grid with a reciprocal space discretization of 45 Å was used. All calculations were performed spin polarized and were initialized in a ferromagnetic state. All structures were relaxed with respect to the lattice and atomic coordinates using a force convergence of 0.02 eV/Å and an energy convergence of 10^{-5}eV.

5.2 Results

5.2.1 Wadsley-Roth Block Structures

Wadsley-Roth phases are made of octahedrally coordinated metal cations (Figure 5.1(a)) that assemble into infinitely long $n \times m$ blocks as illustrated in Figure 5.1(b). The corners of the octahedra represent oxygen ions. Each octahedron shares a corner oxygen with an adjacent octahedron within the same block. The integer n (m) refers to the number of corner sharing octahedra along the $\hat{x}$ ($\hat{y}$) axis of the Cartesian coordinate system of Figure 5.1. There is no bound on the number of corner sharing octahedra along the $\hat{z}$ axis of each $n \times m$ block.

Different $n \times m$ blocks of a Wadsley-Roth phase are joined together as illustrated in Figure 5.1(c), which shows a side view in the $\hat{x} - \hat{z}$ plane. The octahedra along the

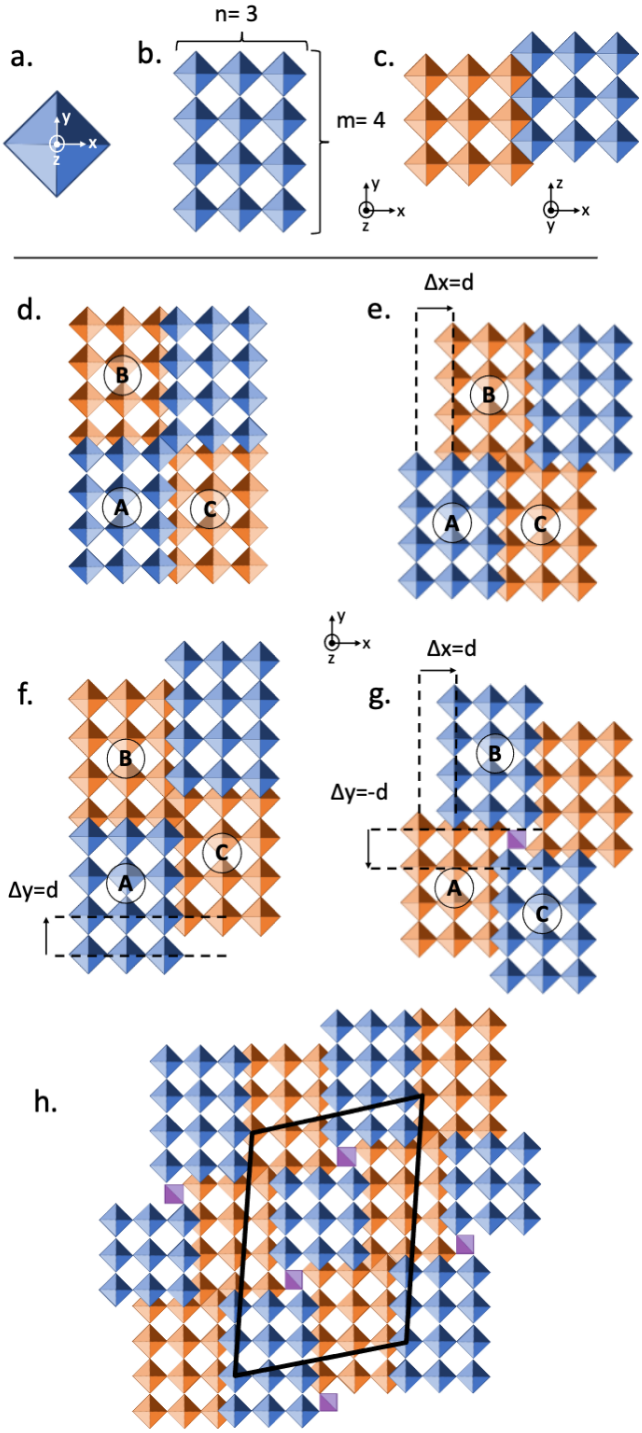

Figure 5.1: Wadsley-Roth crystallographic shear structures are made of MO_6 octahedra (M = metal, O = oxygen) (a) that form infinitely long $n \times m$ corner-sharing blocks (b). The blocks are joined along "shear boundaries" (c). The blocks can tile space in a multitude of ways to generate a rich variety of Wadsley-Roth crystal structures (d)-(h).

periphery of a block share edges with octahedra of neighboring blocks, which leads to an off-set along the $\hat{z}$-axis between adjacent blocks by half the height of an octahedron. The plane of edge sharing octahedra between neighboring $n \times m$ blocks is referred to as a crystallographic shear boundary (not to be confused with a mechanical shear).

There are multiple ways to join different $n \times m$ blocks of corner sharing octahedra when viewed down the $\hat{z}$ axis. Figure 5.1(d) shows a simple checker-board pattern of 3×4 corner sharing blocks within the $\hat{x} - \hat{y}$ plane. More complex arrangements are also possible in which the relative positions of neighboring blocks are shifted by an integer number of the width of an octahedron d. In Figure 5.1(e), block B is shifted by a distance d along the $\hat{x}$ axis relative to block A. In Figure 5.1(f), block C is shifted upwards along the $\hat{y}$ axis by a distance d relative to block A. Another arrangement can be realized by shifting both the B and C blocks relative to the A block as illustrated in Figure 5.1(g), leading to a tunnel along the $\hat{z}$ axis of tetrahedrally coordinated sites, shown in purple. To achieve this pattern, block B shifts by a distance d along the $\hat{x}$ axis and block C shifts down by a distance d along the $\hat{y}$ axis.

An infinite number of Wadsley-Roth crystal structures can be enumerated by varying the dimensions n and m of the block in the $\hat{x} - \hat{y}$ plane and by varying the relative shift of adjacent blocks as illustrated for the 3×4 blocks of Figure 5.1. Only a subset of all possible Wadsley-Roth phases that can be generated in this manner have been observed experimentally. Furthermore, some experimentally observed Wadsley-Roth phases have crystal structures that cannot be generated by tiling a single $n \times m$ block. These more complex Wadsley-Roth phases are generated by tiling a collection of differently sized corner-sharing blocks. An example is illustrated in Figure 5.1h, an idealized crystal structure for $Nb_{47}O_{116}$ as described by Koccer et al[92]. This structure combines 3×4 and 3×3 blocks that tile space to produce a mix of tetrahedral and edge-sharing corners.

Cava introduced a naming scheme to distinguish different classes of Wadsley-Roth

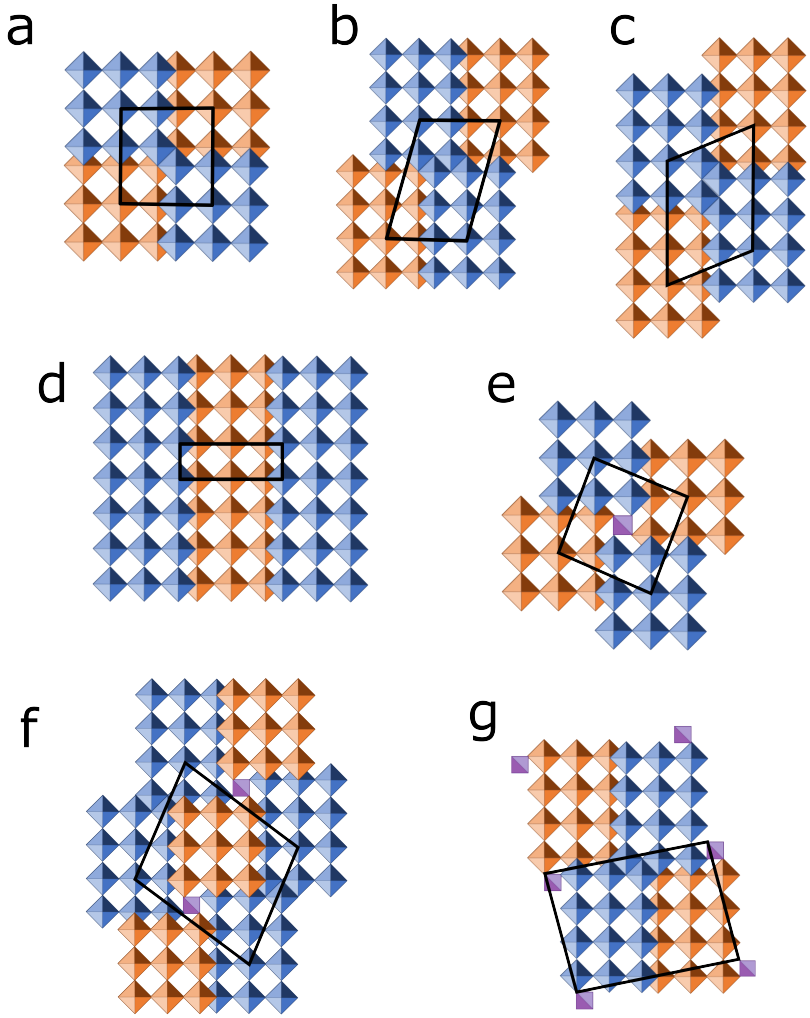

Figure 5.2: Seven different examples of Wadsley-Roth shear structures. With the augmented naming scheme of Cava, these can be referred to as (a) $E_0[3 \times 3]$, (b) $E_{1x}[3 \times 4]$, (c) $E_{2y}[3 \times 4]$, (d) $E[3 \times \infty]$, (e) $T[3 \times 3]$, (f) $M[3 \times 3, 3 \times 4]$, and (g) $M[3 \times 4, 3 \times 4]$. Both (b) and (c) have the same block dimensions but have a different relative offset between neighboring blocks. (f) and (g) both fall into the broader category of the more complicated mixed Wadsley-Roth structures.

phases.[29] Wadsley-Roth phases that exclusively have edge-sharing octahedra at the corners of each block are labeled E while those that have tetrahedrally coordinated sites at each corner are labeled T. The Wadsley-Roth phases made of a single block that only have a relative shift along $\hat{x}$ or along $\hat{y}$, but not both, are E structures (e.g. Figures 5.1(d), (e) and (f)). Those with a relative shift of adjacent blocks in both the $\hat{x}$ and $\hat{y}$ directions that result in a tetrahedrally coordinated site at each block corner are T structures (Figure 5.1g). Those with a mixture of edge sharing octahedra and tetrahedral sites at block corners are type M. These more complex structures tend to be composed of motifs that are made of multiple block sizes.

Here we augment Cava's naming scheme to enable a more precise specification of the Wadsley-Roth phases within a particular category of structures. For the category of E Wadsley-Roth phases, made of a single $n \times m$ block, we append a modifier to E to specify the block size and the relative shift between neighboring blocks. To avoid ambiguity, we orient the block such that the shorter edge length is parallel to the $\hat{x}$ axis. By this convention, the Wadsley-Roth phases of Figures 5.2(a), (b), (c) and (d) can be uniquely labeled. The Wadsley-Roth phase of Figure 5.2(a), for example, becomes $\mathrm{E}_0[3 \times 3]$, with the subscript 0 indicating that there is no relative shift between neighboring blocks. The structures of Figures 5.2(b) and (c), which have undergone relative shifts along the $\hat{x}$ and $\hat{y}$ directions, respectively, are labeled $\mathrm{E}_{1x}[3 \times 4]$ and $\mathrm{E}_{1y}[3 \times 4]$. The integer subscript indicates the number of units of the width of an octahedron that a neighboring block has been shifted along the $\hat{x}$ or $\hat{y}$ direction. Block shifts of up to $n-1$ along $\hat{x}$ and $m-1$ along $\hat{y}$ can generate symmetrically unique structures. For square blocks (i.e. $n = m$), there is no need to specify a shift direction since a shift along $\hat{x}$ or along $\hat{y}$ will generate symmetrically equivalent structures. Meanwhile, the structure made of $3 \times \infty$ blocks in Figure 5.2(d) becomes $\mathrm{E}[3 \times \infty]$, where the subscript has been omitted since all shear boundaries are parallel. A method to systematically enumerate E Wadsley-Roth phases

is described in Appendix B.

Following Cava, we continue to label the Wadsley-Roth phases that host tetrahedrally coordinated sites as T, but suggest an additional modifier to specify the block size. Hence, the structure of Figure 5.2(e) becomes T[3×3]. There is no need to specify the relative shifts between neighboring blocks as there is only one set of shifts that will generate a tetrahedral site at the junction of four blocks: a positive shift by a distance d along $\hat{x}$ and a negative shift by d along the $\hat{y}$. Any other combination of $\hat{x}$ and $\hat{y}$ shifts of neighboring blocks will generate unphysically large open tunnels at the junctions of four blocks that are not present in any experimentally observed Wadsley-Roth phases.

Finally, the more complex Wadsley-Roth structures with a mixture of edge sharing octahedra and tetrahedral sites at block corners are designated as type M in accord with Cava's nomenclature. These more complex structures tend to be composed of repeating motifs that consist of multiple blocks with different dimensions n and m.[160, 170, 144, 171, 172, 173] Two simple M structures are illustrated in 5.2 g and f. These are composed of pairs of blocks that either have a different shape (f) or the same shape (g) and that are then tiled as a unit to generate the crystal structure. As these structures can be quite elaborate, containing multiple blocks in their repeat units that themselves are then tiled in diverse of ways, we did not determine an unambiguous method with which to specify the resulting structure. Instead, we simply modify the label M with a list of the dimensions of the blocks that define the repeat unit that tiles space. Thus the structure in Figure 5.2 f is designated M[$3 \times 3, 3 \times 4$] while that of g becomes M[$3 \times 4, 3 \times 4$]. Similarly the more complicated structure in Figure 5.1 h becomes M[$3 \times 4, 3 \times 4, 3 \times 3, 3 \times 4$]. While the T and E nomenclature can designate a specific crystal structure, there may be more than one structure which can fit a given M-type description.

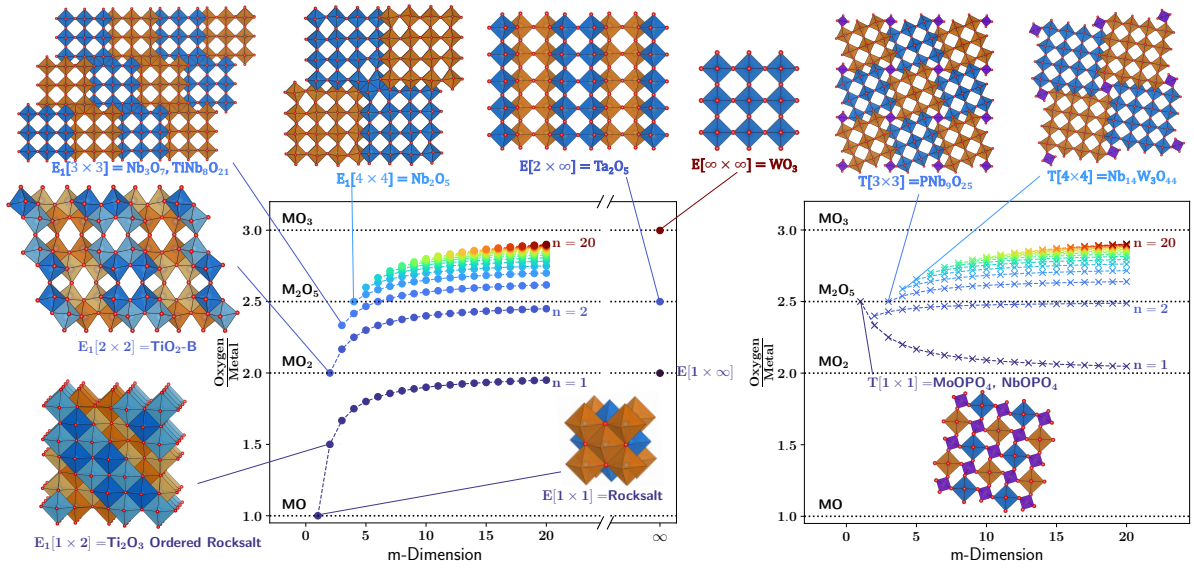

Figure 5.3: (a) The ratio of oxygen to metal of $E_{i\alpha}[n \times m]$ Wadsley-Roth structures as a function of block dimensions n and m. Each curve represents a fixed value of n while the horizontal axis tracks m. (b) The ratio of oxygen to metal of T$[n \times m]$ Wadsley-Roth structures as a function of block dimensions. A variety of technologically important crystal structures emerge as part of a systematic generation of E and T Wadsley-Roth block structures. The blue and orange octahedra indicate neighboring blocks which are offset by $\frac{d}{2}\hat{z}$.

5.2.2 Wadsley-Roth composition and relation to structure

The structural versatility of Wadsley-Roth phases enables oxide stoichiometries that span a wide range of oxygen to metal ratios. The oxygen to metal ratio of an oxide M_pO_q, defined as $\phi = q/p$, can be tuned by varying the block size and relative shifts between neighboring blocks. Figure 5.3(a) shows the dependence of the oxygen to metal ratio, ϕ, of the E type Wadsley-Roth phases as a function of block size. The compositions of the E type Wadsley-Roth phases are only affected by the block size and not the relative shift between neighboring blocks. Each curve corresponds to a particular value of n, while the horizontal axis corresponds to m in the E$_{ix}[n \times m]$ and E$_{jy}[n \times m]$ family of Wadsley-Roth phases. The composition of the E Wadsley-Roth phases can be calculated according to

[23]

$$\phi = \frac{3nm - n - m}{nm} \tag{5.1}$$

Values of ϕ consistent with E Wadsley-Roth phases range between 1 and 3.

The upper horizontal dashed line at $\phi = 3$ in Figure 5.3 corresponds to the stoichometry of WO_3 and is asymptotically reached when the block dimensions become infinitely large (i.e. $E_0[\infty \times \infty]$). The resultant structure is simply the corner-sharing ReO_3 perovskite-like crystal adopted by WO_3 without any crystallographic shear boundaries. The introduction of crystallographic shear boundaries between finite-sized $n \times m$ blocks reduces the oxygen to metal ratio from its maximum value at $\phi = 3$ due to the replacement of corner-sharing octahedra with octahedra that share edges along crystallographic shear boundaries. The lowest dashed line at $\phi = 1$ in Figure 5.3 can only be achieved with 1×1 blocks, which when combined with neighboring 1×1 blocks through edge-sharing crystallographic shear planes generates the dense rocksalt MO crystal structure.

Figure 5.3 clearly shows that the Wadsley-Roth structures are bracketed by the densely-packed rocksalt crystal, equivalent to $E_0[1 \times 1]$, at one extreme and the open perovskite-like crystal structure of ReO_3, $E[\infty \times \infty]$, at the other extreme. The rocksalt structure consists of only edge-sharing octahedra, while the perovskite-like structure of ReO_3 is made of only corner-sharing octahedra. All other Wadsley-Roth type phases combine local environments of both rocksalt and the perovskite-like ReO_3 structures.

The dashed line at $\phi = 2.5$ in Figure 5.3(a) corresponds to the oxygen to metal ratio of Nb_2O_5 and Ta_2O_5. This ratio is asymptotically approached for a Wadsley-Roth phase with $n = 2$ and $m \to \infty$. The resultant $E[2 \times \infty]$ Wadsley-Roth phase is the stable polymorph of Ta_2O_5. The same horizontal line at $\phi = 2.5$ also crosses the $n = 4$ line at $m = 4$, corresponding to $E_i[4 \times 4]$, and the $n = 3$ line at $m = 6$, which corresponds to the $E_{ix}[3 \times 6]$ and $E_{jy}[3 \times 6]$ structures. The horizontal dashed line at $\phi = 2$, the

stoichometry of TiO_2, is asymptotically approached from by below by the $n = 1$ line as $m \to \infty$. The resulting Wadsley-Roth phase, E$[1 \times \infty]$, is hypothetical, consisting of two-dimensional sheets of edge-sharing octahedra that are corner sharing with adjacent sheets. This structure does not coincide with any polymorph adopted by TiO_2. The same oxygen to metal ratio of $\phi = 2$, however, can also be realized with the E$_i[2 \times 2]$ Wadsley-Roth structures. In fact, E$_1[2 \times 2]$ can be shown to be the structure of TiO_2-B, a polymorph of TiO_2 that is generally not recognized as belonging to the Wadsley-Roth family of crystals. Similar to other Wadsley-Roth phases, the TiO_2-B polymorph is a promising anode material for Li-ion batteries.[174, 175, 176, 177] Another interesting enumerated structure is that of E$_1[1 \times 2]$ at $\phi = 1.5$, which can also be viewed as a rocksalt structure with cation vacancies and which was recently predicted to have a low energy in the Ti-O binary.[9]

As with the E type Wadsley-Roth phases, it is possible to systematically enumerate T$[n \times m]$ Wadsley-Roth structures, which contain tetrahedral sites at the junctions between four $n \times m$ blocks of corner sharing octahedra. In these structures the oxygen to metal ratio can be calculated with [23]

$$\phi = \frac{3nm - n - m + 4}{nm + 1} \tag{5.2}$$

where the tetrahedral site accounts for the addition of 4 oxygen atoms and 1 metal atom to the chemical formula. The tetrahedral sites may be filled by a transition metal[140, 178, 134, 27, 179, 180, 181], or by small cations such as phosphorus. At most half of the tetrahedral sites are filled and the ordering in which these sites are filled offers another degree of freedom for these crystal structures [94].

Figure 5.3(b) shows the relation between the oxygen to metal ratio, $\phi = q/p$ in M_pO_q, as a function of n and m. Each curve corresponds to a fixed value of n while the horizontal

axis corresponds to m. As with the E type structures, the asymptotic limit of infinitely large blocks, i.e. T[$\infty \times \infty$], is the ReO_3 perovskite-like structure adopted by WO_3. At the other extreme, T[1×1] is a structure consisting of a high density of octahedral and tetrahedral sites as illustrated in the inset in Figure 5.3(b). This structure is adopted by many phosphate compounds, such as $MoOPO_4$[182] and $NbOPO_4$[183, 184], where the tetrahedral sites are occupied by phosphorus and the octahedral sites by the transition metal. This structure is also seen in high pressure $TaOPO_4$[185] and similar structures are observed for Cr and V phosphates, though in these cases Cr and V distort away from the center of their octahedra and thereby adopt a pyramidal coordination by oxygen. The tetrahedral sites is also filled by phosphorus in the T[3x3] structure of PNb_9O_{25}, a promising electrode material for Li-ion batteries [95, 186]. In contrast to the other T structures, the oxygen to metal ratio, ϕ, for T[$1 \times m$] decreases with increasing m. This is because an increase in the length of the $1 \times m$ block increases the number of edge sharing octahedra in the structure without generating any additional corner sharing octahedra as occurs in other block geometries.

The oxygen to metal ratios of $\phi = 3$, 2.5 and 2 have a special significance as these correspond to the stoichiometries of WO_3, Nb_2O_5 and TiO_2 in which the metals are in their maximum oxidation states. Oxygen to metal ratios that deviate from those of WO_3, Nb_2O_5 and TiO_2 can be realized by combining cations with different oxidation states. Cations such as Nb can accommodate multiple formal oxidation states and form Wadsley-Roth phases that contain a mix of Nb^{5+} and Nb^{4+}. Cations with different maximum oxidations states can also be combined to form a wide variety of Wadsley-Roth structures. For example, a range of Wadsley-Roth phases have been synthesized [29, 93, 187, 188, 23, 54] with values of ϕ between those of WO_3 at $\phi = 3$ and Nb_2O_5 at $\phi = 2.5$ by combining different ratios of W^{6+} and Nb^{5+} cations. These can adopt Wadsley-Roth structures that lie between the dashed lines at $\phi = 3$ and $\phi = 2.5$ in

Figure 5.3(a) and (b). Wadsley-Roth phases have also been synthesized by combining Ti^{4+} with Nb^{5+}. These can adopt structures between the dashed lines at $\phi = 2$ and $\phi = 2.5$ in Figure 5.3(a) and (b). As is clear from Figure 5.3, the Wadsley-Roth phases containing W^{6+} and Nb^{5+}, which have high oxidation states, have larger block sizes than those containing Ti^{4+}.

5.2.3 Stability of $E_{i\alpha}[n \times m]$ WR structures for Nb_pO_q

While multiple M_pO_q Wadsley-Roth phases can be enumerated for common oxygen to metal ratios $\phi = q/p$, only a subset of them are observed experimentally. To explore the structural features that determine the relative stability among enumerated Wadsley-Roth structures, we calculated the energy of Nb_pO_q in $E_{ix}[n \times m]$ and $E_{jy}[n \times m]$ Wadsley-Roth structures for values of $i \leq n-1$ and $j \leq m-1$. Five different values of $\phi = q/p$ were explored, corresponding to the oxides Nb_2O_5, $Nb_{12}O_{29}$, $Nb_{15}O_{37}$, Nb_3O_7 and NbO_2. As encapsulated in Figure 5.3, the stoichiometry of the oxide restricts the values of n and m to particular values.

Figure 5.4 shows the calculated energies for each stoichiometry as a function of the shift i or j along the $\hat{x}$ or $\hat{y}$ directions, respectively. Figure 5.4(a) shows the energies for idealized Wadsley-Roth phases in which all the octahedra retain their cubic symmetry. Only the volumes of each structure were allowed to relax. These energies do not account for the effects of atomic relaxations, which for Wadsley-Roth phases are dominated by distortions of the MO_6 octahedra and changes in the distances between edge-sharing cations. Figure 5.4(b) shows the energies of the fully relaxed structures, while Figure 5.4(c) shows the difference between (b) and (a) and represents the energy gained as a result of atomic relaxations. As is clear in Figure 5.4, the unshifted $E_0[n \times m]$ WR phases are unfavorable both with and without atomic relaxations. The $E_{1\alpha}[n \times m]$ structures,

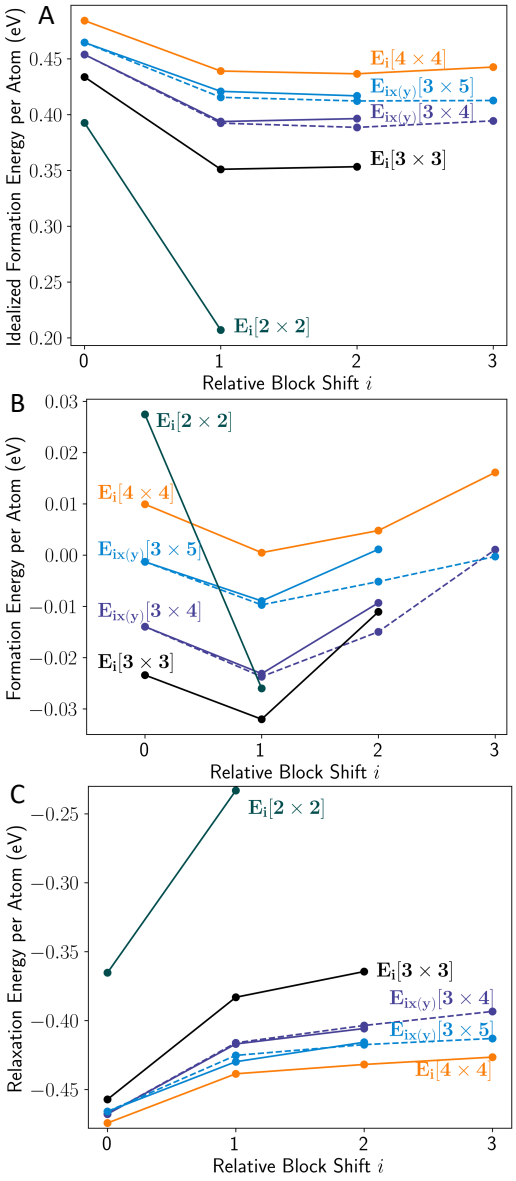

Figure 5.4: The formation energy per atom of Nb_pO_q in several $E_{i\alpha}[n \times m]$ Wadsley-Roth structures as a function of the shift i in the $\alpha = \hat{x}$ or $\alpha = \hat{y}$ directions. Each line color represents a different $n \times m$ block size (and therefore composition $\phi = q/p$). The formation energies are calculated relative to Nb_2O_5 in the $E_1[4 \times 4]$ structure and bcc Nb. The solid lines refer to $E_{ix}[n \times m]$ structures while the dashed lines refer to $E_{iy}[n \times m]$ structures. (a) Unrelaxed energies, (b) fully relaxed energies and (c) relaxation energy, calculated as the difference between the relaxed energy of (b) and the unrelaxed energy of (a).

with $\alpha = x$ or y, have the lowest energies for all five stoichiometries when allowing for full relaxations. Even in the absence of relaxations, these structures are either the most favored or a close second. While the $E_{2\alpha}[n \times m]$ and $E_{3\alpha}[n \times m]$ structures have energies that are similar to those of the $E_{1\alpha}[n \times m]$ structures in the absence of atomic relaxations, they are much less favored after relaxations, indicating that they have less flexibility to lower their energy during relaxation. In fact, Figure 5.4(c) shows that the amount of energy gained during relaxation decreases (i.e. becomes less negative) with increasing shift, i, with the $E_0[n \times m]$ structures able to lower their energy by the largest margin as a result of atomic relaxations.

The trend exhibited by the unrelaxed energies in Figure 5.4(a) can be explained in terms of the number of edge-sharing octahedra. The high oxidation state of Nb results in large repulsive electrostatic interactions between edge-sharing cations. The number of edges shared by Nb per unit cell in $E_0[4 \times 4]$, for example, is 36, while the number of shared edges in the other three Wadsley-Roth structures ($E_1[4 \times 4]$, $E_2[4 \times 4]$ and $E_3[4 \times 4]$) is 34. More generally, the number of edges shared by Nb in the $E_0[n \times m]$ structure is larger than that in the $E_{i\alpha}[n \times m]$ structures when $i > 0$ and α is either x or y. In the absence of relaxations, these electrostatic interactions dominate and penalize the $E_0[n \times m]$ structure relative to $E_{1\alpha}[n \times m]$, $E_{2\alpha}[n \times m]$ and $E_{3\alpha}[n \times m]$, the latter three having very similar energies, which is consistent with the fact that they have the same number of edge sharing Nb cations.

Figure 5.4(c) shows that $E_0[n \times m]$ is able to lower its energy by the largest amount during relaxation, and that the energy lowering during relaxation for the other $E_{i\alpha}[n \times m]$ Wadsley-Roth structures decreases with increasing shift i. There are two dominant driving forces that direct relaxations in Wadsley-Roth phases. The first is due to a second-order Jahn-Teller instability of d^0 cations, such as Nb^{5+}, which leads to a displacement of those cations away from the centers of their octahedrally coordinated sites. The

second is the large electrostatic repulsion between cations of octahedra that share edges which increases cation-cation distances through an additional off-centering of the cations involved. The off-centering in response to the cation-cation repulsions of edge-sharing octahedra also leads to further collateral distortions of the surrounding oxygen ions.

The $E_0[n \times m]$ structures undergo a larger reduction in energy during relaxation than the other $E_{i\alpha}[n \times m]$ Wadsley-Roth structures (with $i > 0$) because they have more edge-sharing octahedra per transition metal. The $E_0[n \times m]$ structures benefit more per transition metal from the off-centering of the cations of edge-sharing octahedra to reduce electrostatic repulsion during relaxation. The number of edge-sharing octahedra per transition metal, however, does not fully explain the variation in relaxation energy with structure since the $E_{i\alpha}[n \times m]$ structures with $i > 0$, which all have the same number of edge-sharing octahedra, continue to exhibit small differences in relaxation energy. More subtle differences between the $E_{i\alpha}[n \times m]$ structures with $i > 0$, such as the orientation of the shared edges relative to the block length, lead to small variations in their relaxation energies. This is discussed in more detail in Appendix B.

By calculating the fully relaxed energies of systematically enumerated $E_{i\alpha}[n \times m]$ Wadsley-Roth phases for Nb_pO_q at various values of $\phi = q/p$ and those of experimentally observed Wadsley-Roth structures, it is possible to assess zero Kelvin phase stability in the oxygen rich portion of the Nb-O binary phase diagram. Figure 5.5 shows calculated formation energies and the resultant convex hull of the Nb-O binary in the vicinity of the Nb_2O_5 stoichiometry. The reference states for the formation energies are pure Nb in the bcc crystal structure and the lowest energy Nb_2O_5 structure, which has the $E_1[4 \times 4]$ Wadsley-Roth crystal structure. A variety of experimentally observed and enumerated Wadsley-Roth phases are predicted to reside on the convex hull. We note that DFT-PBE does not predict the distorted rutile form of NbO_2 as a ground state. The Nb_3O_7 ground state in Figure 5.5 is therefore in equilibrium with the vacancy ordered rocksalt form

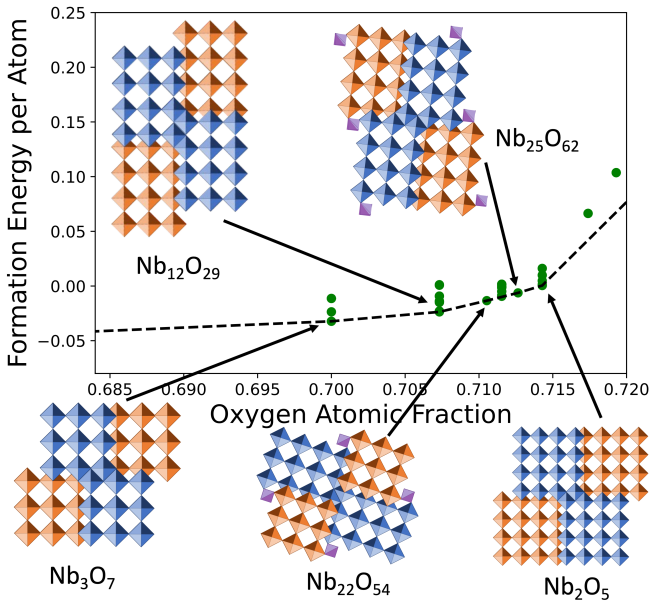

Figure 5.5: Formation energies of systematically enumerated Wadsley-Roth structures and other known structures of the Nb-O binary. The reference states for the formation energies are Nb_2O_5 in the $E_1[4\times4]$ structure and bcc Nb. Five of the predicted ground states along the Nb-O binary are Wadsley-Roth phases: Nb_3O_7, $Nb_{12}O_{29}$, $Nb_{25}O_{62}$, $Nb_{22}O_{54}$, and Nb_2O_5.

of NbO. The predicted $Nb_{12}O_{29}$ ground state has the $E_{1y}[3 \times 4]$ structure while only the monoclinic form of $Nb_{12}O_{29}$ with the $E_{1x}[3 \times 4]$ structure has been experimentally synthesized[92]. Both structures have similar formation energies, with a difference of less than 1meV per atom.

5.3 Discussion

The Wadsley-Roth family of crystal structures are adopted by a wide variety of early transition metal oxides containing Ti, V, Nb, Ta, Cr, Mo and W. Many Wadsley-Roth phases are promising anode materials for Li-ion batteries due to their ability to intercalate Li ions at high rates and at low voltages.[187, 92, 181, 136, 139, 94, 95, 54, 189, 190, 191, 134, 143, 192, 193, 194, 195, 196, 2, 197, 198, 135] They are also important for structural

applications as they are formed by many of the early transition metals of multi-principal element refractory alloys. Their open crystal structures, however, make them unsuited as protective oxide scales for corrosive or high temperature structural applications and strategies are desired to suppress their formation in favor of more dense and protective oxide scales.

In this work, we have analyzed and classified Wadsley-Roth phases and developed approaches to systematically enumerate an important subset of their crystal structures. We have extended Cava's naming scheme [29] to be more precise and descriptive by adding specifications for the block size and relative offset of neighboring blocks. By systematically enumerating the structures of two subclasses of Wadsley-Roth phases we have been able to identify relationships between important oxide crystal structures that were not previously evident. These are summarized in the structure-composition maps of Figures 5.3(a) and (b).

Building on the work of Roth and Wadsley [23], the structure-composition maps in Figures 5.3(a) and (b) show that the rocksalt structure and the perovskite-like ReO_3 structure are the asymptotic extremes of the Wadsley-Roth family of phases. The perovskite-like ReO_3 structure, also adopted by WO_3, can be viewed as a Wadsley-Roth phase with infinitely sized blocks of corner sharing octahedra (i.e. $E_0[\infty \times \infty]$), while the rocksalt MO structure can be viewed as a Wadsley-Roth phase with 1×1 blocks of corner-sharing octahedra (i.e. $E_0[1 \times 1]$). Interestingly, other well-known crystal structures can be viewed as belonging to the Wadsley-Roth family of phases. For example, the bronze B-TiO_2 crystal structures can be viewed as an $E_1[2 \times 2]$ Wadsley-Roth phase. The stable polymorph of Ta_2O_5 is also a Wadsley-Roth phase with an $E[2 \times \infty]$ structure. The extreme end of the T type block structure with 1×1 block generates a common phosphate structure adopted by $NbPO_5$ and $MoPO_5$. While many of these important crystal structures were not previously recognized as belonging to the family of Wadsley-

Roth crystal structures, they naturally emerge as part of the generative algorithms of Wadsley-Roth phases developed in this study. Generative algorithms and accompanying naming schemes have been developed for two subclasses of Wadsley-Roth phases, though similar approaches to generate the more complex class of Wadsley-Roth phases consisting of multiple differently sized blocks remain to be developed.

Another factor affecting phase stability is the flexibility of the Wadsley-Roth backbone structure in accommodating relaxations. The majority of transition metal cations in Wadsley-Roth phases are in their maximum oxidation state.

The second-order Jahn-Teller distortion leads to an off-centering of the transition metal cation Niobium exhibits a sizable off-centering when occupying the corner sharing octahedra at the center of the block. The off-centering of the transition metal is amplified in edge-sharing octahedra due to the large repulsion between neighboring cations that share a common edge. To first order, the gain in energy due to relaxations correlates with the number of edge-sharing pairs. But when comparing different Wadsley-Roth phases having the same number of edge-sharing pairs, other more subtle structural features affect the ability of cations to favorably relax.

Implications for batteries and at higher temperatures: Anode chemists can used the compositional plots in Figure 5.3 to make predictions of possible phases which can form for novel chemistries and readily generate proposed structure files for theoretical study allowing for more efficient screening of potential battery materials. The collaborations with the author, Dr. Muna Saber [14] showed that electrostatic effects and octahedral relaxations also determine the preferred decorations of cations on Ti-Nb-O Wadsley Roth phases with cations which have lower oxidation states preferring block corners sites. This insight allows battery anode chemists to better predict the placement of cations in these complex structures which can impact electronic properties both in the maximum oxidation states and during lithiation. For instance, over the course of lithiation, prior

work has shown that cePNb9O25 undergoes a volume change related over the course of lithiation [94] related to the formation of metal-metal bonds at the block corners. The [n×m] block corners may tend to reduce first which both reduces electrostatic repulsion and generates metal-metal bonds leading to the observed volume change.

5.4 Conclusion

We have presented a systematic way to generate a subset of Wadsley-Roth block structures and have linked them to a wide variety of experimentally observed and technologically important oxide crystal structures. This perspective unifies a diverse range of structures that include rocksalt, bronze TiO_2 and the perovskite framework of WO_3 among many others. The explicit connections established in this work between Wadsley-Roth crystal structures and the oxygen to metal ratio of an oxide will facilitate structure predictions of alloyed oxides with mixed oxidation states. Our first-principles calculations on enumerated Wadsley-Roth structures has revealed the importance of the number of edge-sharing octahedra and the orientation of the shared edges as the drivers of stability among different Wadsley-Roth structures. In cation alloyed Wadsley-Roth phases, our first-principles calculations have shown that the cations with the highest oxidation states will segregate to octahedra that share the lowest number of edges with neighboring octahedra, while the cations with the lowest oxidation states will accumulate in edge sharing sites along the crystallographic shear boundaries. The systematic approach to generating Wadsley-Roth crystal structures described in this work will enable first-principles search efforts for promising multi-principal element oxides without being restricted to experimentally known crystal structures and provides guidance as to how other families of complex oxide structures can be enumerated algorithmically.

Chapter 6

Solute-Solute Interactions in Dilute Nb-X-O Alloys From First Principles

6.1 Introduction

The need for new high temperature structural materials to improve the efficiency of combustion engines for utility and aerospace applications has motivated a revival of refractory alloy development. Refractory alloys were initially studied during the space race in the 1950s to early 70s. However, the best performing alloys at high temperatures were often brittle and unworkable at lower temperatures, limiting their manufacturability [199, 47, 4, 12]. Many of these metals have a strong tendency to dissolve oxygen, which can embrittle the material [200, 12] and complicate the stabilization of protective oxide scales [201, 202]. Recent advances in additive manufacturing techniques have greatly revised the workability requirements for refractory alloys [4], while the advent of refractory multi-principal element alloys (RMPEAs) has unlocked a new means for tuning mechanical properties and oxidation resistance [53, 59].

RMPEAs have demonstrated improved oxidation resistance compared to traditional

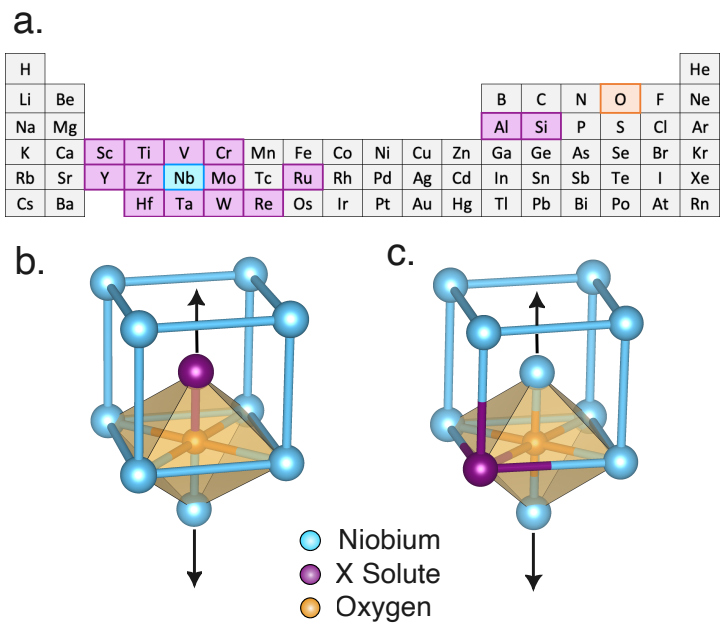

Figure 6.1: (a) The 14 substitutional atoms studied are highlighted on the periodic table in pink while the matrix Nb and oxygen are in light blue and orange respectively. Part b and c show the first and second nearest neighbor environments for the X-O pairs. When and oxygen atom occupies the asymmetric octahedral interstitial site, it imposes an elastic dipole on the surrounding lattice as shown.

refractory alloys [59, 60]. Recent work has shown that oxygen diffusion controls the oxidation rates of RMPEAs[66]. Many of the early transition metals of RMPEAs can dissolve exceptionally high concentrations of interstitial species such as oxygen, nitrogen and carbon. [38, 61, 62, 127, 203, 9, 8]. Alloying can modify interstitial solubility limits [115] and oxidation rates [63], but a clear understanding as to why certain alloying additions bind or repel interstitial oxygen remains to be established. Recent theoretical work focused on calculated binding energies between substitutional solute atoms and interstitial oxygen [204, 115, 205] and used this to predict diffusion coefficients in niobium [206, 207]. Trends in electronegativity and solute size have been used to rationalize calculated binding energies, however, established correlations remain empirical and many notable exceptions remain to be explained [206].

The refractory metal niobium is technologically important as a common constituent

material in RMPEAs as well as the primary component of the most widely used refractory alloys C103 [3]. Niobium has a high melting point of 2468 and a density of 8.5 g/cm^3 [208], which is low relative to other refractory metals, making it an attractive material for high temperature aerospace applications. Niobium has a BCC crystal structure and has a maximum oxygen solubility approaching 10 atomic percent [18, 17]. Both experimental [209] and computational [206] studies have demonstrated that substitutional alloying elements can slow the diffusion of oxygen in niobium, while other studies have demonstrated that the oxygen solubility can be increased or decreased by alloying [42, 126, 38, 61, 62].

In this contribution, we examine interactions between substitutional and interstitial solutes for fourteen X-O pairs (X= Al, Si, Sc, Ti, V, Cr, Y, Zr, Mo, Ru, Hf, Ta, W, or Re) dissolved in niobium. These fourteen substitutional elements are highlighted in light blue in the periodic table of Figure 6.1a and include twelve transitional metals as well as Al and Si. We use first-principles calculations based on Density Functional Theory (DFT) to calculate binding energies and analyze the electronic structure of X-O solute pairs in BCC Nb. The results of the calculations demonstrate relationships between electronegativity and the accumulated charge and size of substitutional solute atoms in the Nb matrix. These each play an important role in determining the binding energies of substitutional solutes to interstitial oxygen at both the first and second nearest neighbor distance. We also identify a short-ranged repulsive interaction that arises from the closed-shell hybridization of localized atomic orbitals that plays an important role for a subset of X-O solute pairs.

6.2 Methods

The reader is referred to Chapter 3 for more details and background on the first principles methods used in this chapter. Substitutional solute-oxygen binding energies

in BCC Nb were calculated with Density Functional Theory (DFT) using a cubic super cell of the bcc unit cell that contained 54 substitutional sites. The binding energies are estimated as the difference between the energy of nearest neighbor solute-oxygen configurations ($\approx 1.6 - 2$ Å) and a configuration in which the solute and oxygen are separated by a large distance (≈ 7.35 Å). DFT calculations were performed using the VASP package [76, 77] with the Perdew, Burke, Ernzehof (PBE) exchange correlation functional [75]. The interactions between the core and valence electrons were treated with projector augmented wave method (PAW) [78, 79] pseudopotentials (PAW pseudopotentials with the following names were used for each element: Al, Si, Sc_sv, Ti_sv, V_sv, Cr_pv, Y_sv, Zr_sv, Nb_sv, Mo_sv, Ru_pv, Hf_pv, Ta_pv, W_sv, Re, O). A 575 eV plane wave cut-off energy and a Γ-centered k-point grid with a density of 45 Å was used. All calculations were spin polarized and final static calculations used the tetrahedron method with Blöchl corrections. Similar DFT calculations were performed to obtain densities of states (DOS) and partial charge densities. Bader charges [210, 211] were calculated using the methodology of Henkelman et al[102, 103, 104, 105]. The volume and shape of the supercell were kept fixed, while the atomic positions were allowed to relax until the forces converged to 0.02 eV/Å.

6.3 Results

6.3.1 Geometry of an octahedrally coordinated interstitial in BCC

Dissolved oxygen atoms in niobium occupy the octahedral interstitial site in the BCC lattice. This site is asymmetric and has one axis that is shorter than two others. Figure 6.1 illustrates the two symmetrically distinct sites that a solute atom in BCC can

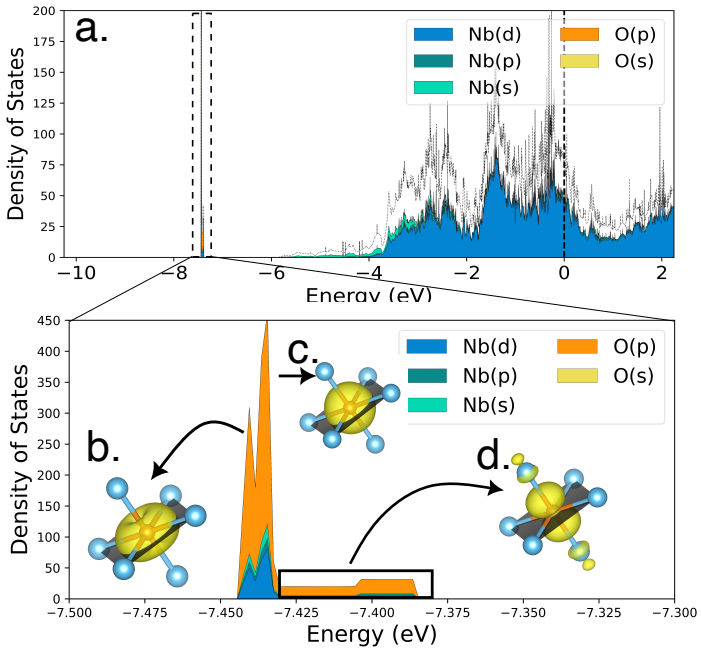

Figure 6.2: (a) The projected DOS for $Nb_{54}O$ is plotted with the total density of states shown as a dotted line. Highlighted below are the partial charge densities corresponding to the oxygen p orbitals. Those aligned with the symmetric axes indicated by the grey plane(b) are lower in energy while the states associated with the asymmetric axis are higher in energy(d). The region between (c) contains contributions from all three p-orbitals.

occupy when directly coordinating an interstitial oxygen atom. A solute atom occupying one of the sites along the short axis of the octahedron is in a first-nearest neighbor position relative to the interstitial oxygen (Figure 6.1b), while a solute atom on one of the remaining sites (on the equator of the flattened octahedron) is in a second nearest neighbor position relative to the oxygen interstitial (Figure 6.1c). An interstitial oxygen atom will induce a strain on the surrounding matrix as illustrated by the arrows in Figure 6.1 b and c.

6.3.2 Electronic Structure of Dilute Oxygen in Niobium

Figure 6.2(a), shows the calculated electronic density of states (DOS) of a 54 atom supercell of BCC Nb and one oxygen atom in an octahedral site. The Fermi level is indicated by the vertical dashed line and cuts through states that are primarily derived from niobium valence states having d character. Far below the Nb d states are highly localized states at approximately 7.4 eV below the Fermi level. These states, which have p character, have charge densities that localize around the interstitial oxygen. The high energy region of these states derives from a localized p state with its lobes aligned along the short axis of the octahedral site (Figure 6.2b), while the states with slightly lower energy derive from orthogonal p-like orbitals with increased charge density along the waist of the octahedron as denoted by a blue plane (Figure 6.2d). In a neutral oxygen atom, the valence p orbitals are partially occupied. The states between contain contributions from all three p orbitals Figure 6.2c. However, since the p-orbitals of the dissolved oxygen in niobium are far below the Fermi level, they become fully occupied, resulting in a local accumulation of charge around the oxygen atom. The Bader charges on the oxygen in all calculations are approximately -1.3 (Appendix C S2).

6.3.3 Electronic Structure of Dilute Nb-X Alloys

Most of the studied Nb-X-O alloys have very similar density of states (Appendix C C3-5) to Nb with dilute oxygen (Figure 6.2). Figure 6.3 shows the projected and total DOS for a BCC supercell with 53 Nb atoms and 1 Ru atom. Since Ru is dilute, the density of states projected onto the Ru atom is plotted separately in Figure 6.3(b) for the same energy range. The valence states associated with the Ru solute (band for the Ru atom) and the Nb atoms are very similar, spanning the same energy range and exhibiting a similar mix of d, p and s character. The valence states of many of the studied 3d, 4d,

and 5d elements are very similar to those of Ru in $Nb_{53}Ru$ and overlap with the niobium states. These metal states are well-separated in energy from the low energy oxygen p states localized on oxygen. However, there were some notable outliers, particularly the group 3 elements Si and Al (Figure C3).

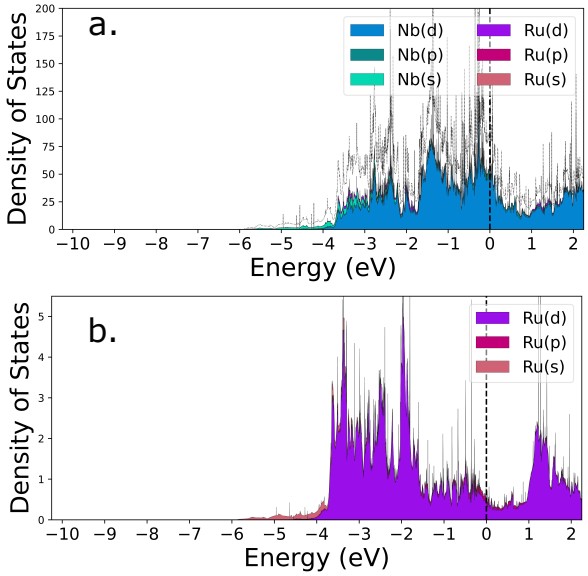

Figure 6.3: The projected DOS for a $Nb_{53}Ru$ cell is shown along with the total DOS as a dotted line(a). The contribution from the Ru atoms is highlighted in (b). Since Ru is dilute its electrons constitute only a small portion of the electron density. The Ru electronic states nearest the valence band consist mostly of d states and largely overlap with the niobium electron band. These overlapping partially filled electronic state near the Fermi level are typical of the majority of the transition metal alloying elements studied.

6.3.4 Electronegativity and Charged Solutes

Previous studies of solute binding energies in Ti have revealed the importance of short-range electrostatic interactions between neighboring solutes. Electrostatic interactions emerge as a result of electron transfer between the host and the solutes [115, 205]. Bader charges [210, 211] serve as a measure of the degree with which charge is transferred between different elements within a solid. Figure 6.4a plots the calculated Bader charges

of the different substitutional solute elements in the Nb host when the solute is next to an interstitial oxygen atom. A non-zero Bader charge on a substitutional solute indicates that there is some degree of charge transfer between the solute and the Nb host. The Bader charges tend to decrease when moving from left to right in the periodic table. This trend is more pronounced when the substitutional solute is in the 2nd nearest neighbor site relative to an oxygen interstitial. A positive Bader charge indicates a transfer of electrons from the solute to the Nb host, while a negative Bader charge indicates an opposite transfer of electrons. With the exception of Al and Re, all Bader charges are enhanced for the second nearest neighbor site compared to first nearest neighbor site. Bader charges on the solutes when the they are at large distances from the interstitial oxygen can be found in the Appendix C C1.

Figure 6.4b plots the calculated solute Bader charges as a function of the difference in the electronegativities, $\Delta\chi$, between the solute and Nb, revealing a clear correlation between the two quantities. When the substitutional solute atom has a higher electronegativity than Nb ($\Delta\chi > 0$), it tends to attract electrons from the matrix and accumulate an additional negative charge (Figure 6.4b). Conversely, when Nb has a higher electronegativity than the solute atom ($\Delta\chi < 0$), it tends to pull electrons away from the solute atom, resulting in a positively charged solute (Figure 6.4b). Since the solid as a whole is comprised primarily of Nb which has a sizable density of states at the Fermi level and is metallic, any local accumulation of positive or negative charge on a solute is screened by mobile electrons. Therefore, electrostatic interactions with other locally charged species such as oxygen will only be significant at very short distances.

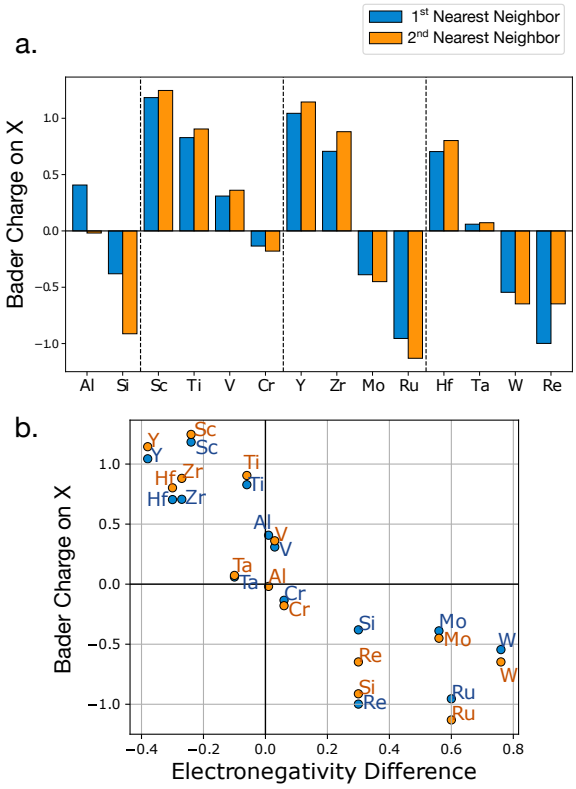

Figure 6.4: (a) The Bader charge calculated on each of the 14 substitutional atoms in the first nearest neighbor and second nearest neighbor sites are shown. The dashed vertical lines separate the 3rd, 4th, 5th, and 6th period elements. (b) The charge a solute atom accumulated in the niobium matrix is related to the difference between the electronegativity ($\Delta\chi$) of the solute atom and the niobium matrix (part b)

6.3.5 Volume Changes of Solute Atoms

Interstitial solutes such as oxygen strain the host crystal as illustrated in Figure 6.1(b) and (c). The resultant strain field interacts with substitutional solutes whose volume differs from that of Nb. The Bader analysis, in addition to measuring the degree of charge transfer, is also able to provide a measure of the volume of an atom [210, 212, 102, 103]. Since substitutional solute atoms can accumulate or surrender charge when dissolved in Nb, their volume in the Nb matrix will deviate from their atomic volume in free space. As is clear in Figure 6.5a, ΔV, defined as the difference in Bader volume and the atomic

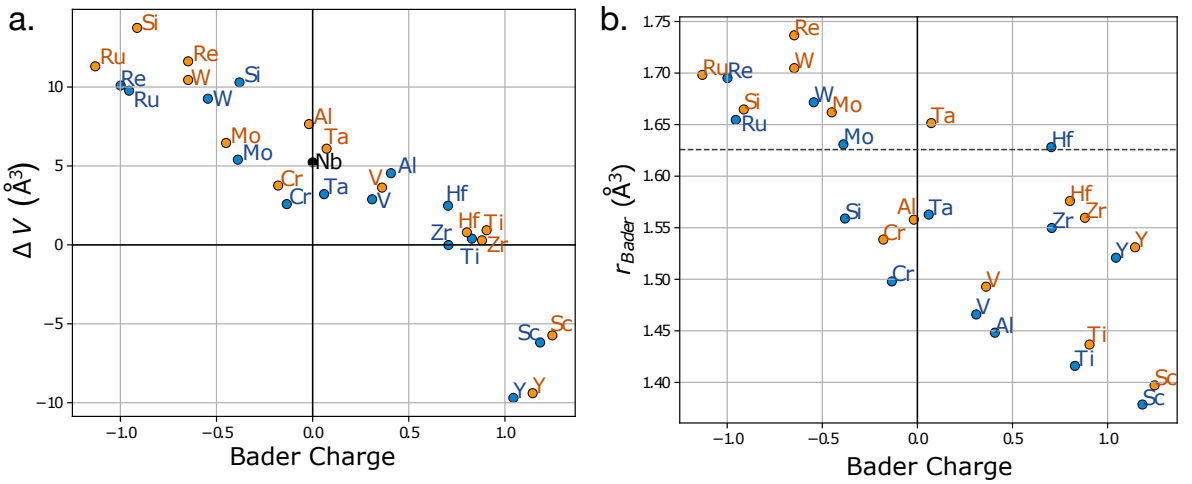

Figure 6.5: Part a. shows the impact of the Bader charge accumulated by a solute atom on the volume of that atom is shown. Blue and orange points correspond to the first and second nearest neighbor sites respectively while the volume change of the Nb matrix is shown as a black point. In Part b, the Bader volume for each solute is plotted as a function of Bader charge with the radius of the niobium matrix atoms indicated by the horizontal dashed line.

volume as tabulated by Slater [213], is strongly correlated with the Bader charge of the solute when dissolved in Nb. This indicates that solute atoms with a large positive or negative Bader charge as a result of electron transfer with the host undergo a sizable change in their atomic volume when dissolved in Nb. For example, Y and Sc, which have atomic volumes that are larger than that of Nb as free atoms, shrink dramatically when dissolved in the Nb matrix. Similarly, several solute atoms with smaller atomic radii, such as W, Re, and Ru, become larger than the Nb host atoms as a result of the accumulation of additional electrons. Figure 6.5b shows the absolute Bader volumes of each solute as a function of Bader charge and compares it to that of niobium (horizontal dashed line). The solutes above (below) the dashed line are larger (smaller) than the Nb host atoms and are expected to interact unfavorably (favorably) with the tetragonal strain fields induced by the interstitial oxygen atoms. Note that the Bader volume of an atom is systematically larger than that of a free atom as it counts some of the interstitial

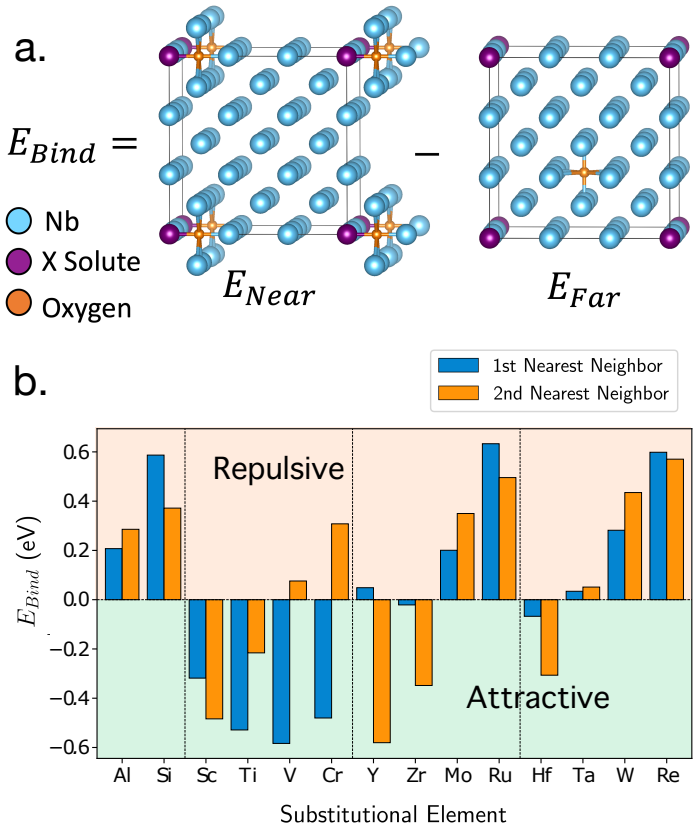

Figure 6.6: (a) The binding energy for each first and second nearest neighbor X-O pair were calculated by subtracting the energy of the a similar unit cell where the oxygen and substitutional element were 7.35 Å apart. (b) The binding energy between oxygen and each of 14 substitutional elements in the first nearest neighbor and second nearest neighbor sites are shown. The dashed vertical lines separate the 3rd, 4th, 5th, and 6th period elements.

space between atoms in a crystal. A measure of this systematic shift is apparent in the positive ΔV for Nb in Figure 6.1(a), which has a zero Bader charge.

6.3.6 Solute-Oxygen Binding Energies and Trends

The binding energies between interstitial oxygen and substitutional solutes, X = Al, Si, Sc, Ti, V, Cr, Y, Zr, Mo, Ru, Hf, Ta, W and Re in BCC Nb were calculated as the difference in energy between a first or second nearest neighbor X-O configuration and a

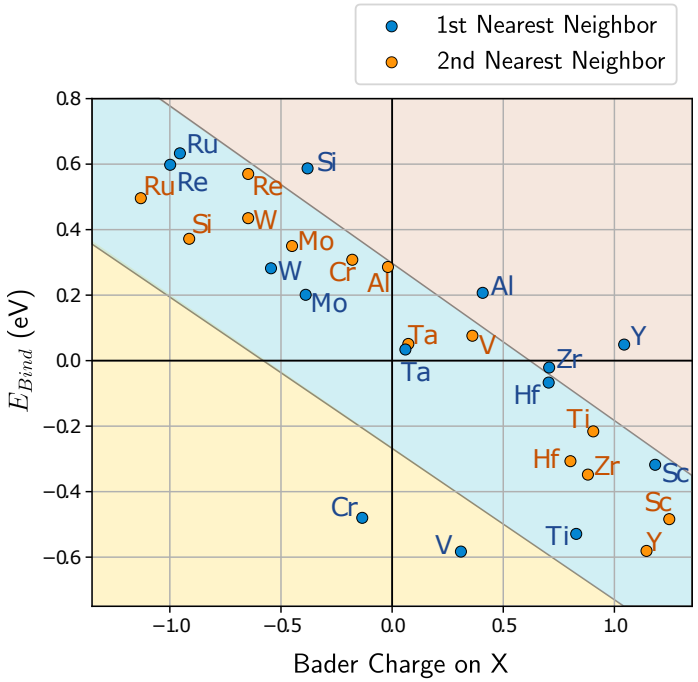

Figure 6.7: The X-O binding energy for the first (blue) and second nearest neighbor (orange) sites are plotted as a function of the Bader charge on solute X.

configuration in which X and O are separated by a large distance. The calculations were performed using a super cell of BCC that contains 54 substitutional sites as illustrated in Figure 6.6(a). The binding energy between an interstitial oxygen atom and each of the 14 substitutional elements placed in the first and second nearest neighbor shell of oxygen are shown in Figure 6.6b. The binding energies range between -0.6 eV and 0.6 eV, with positive (negative) values indicating repulsive (attractive) interactions between X and O in BCC Nb.

Variations in the binding energies can in large part be explained as arising from local electrostatic and strain interactions. This is evident in Figure 6.7, which plots binding energies as a function of solute Bader charges. Most solutes fall within the blue band in Figure 6.7, with negative (positive) solute Bader charges correlated with positive (negative) and repulsive (attractive) binding energies. Since oxygen is negatively charged,

having a Bader charge of -1.3, it will experience a repulsive electrostatic interaction when placed next to a solute with a negative Bader charge. Likewise, the negatively charged oxygen will be attracted to solutes that are positively charged. This qualitative trend is revealed by the blue band of Figure 6.7. Since the Nb host is metallic, with abundant free electrons at the Fermi surface, the electrostatic interactions are strongly screened and should only dominate at very short distances.

Strain interactions are also likely to play an important role in determining binding energies. Interstitial oxygen exerts a tetragonal strain on the BCC lattice that can be relieved by replacing nearest neighbor Nb atoms with smaller solute atoms. Hence smaller solute atoms will be attracted to oxygen, while larger solutes will repel oxygen. As is predicted in Figure 6.5b, the smaller solutes tend to also have positive Bader charges, while the larger solutes accumulate charge from Nb and are negatively charged. Due to this correlation between solute size and Bader charge, strain interactions reinforce the trend that can be explained by short-range electrostatic interactions. Hence, it is not directly evident as to how much of the correlation between the binding energy and the Bader charge in Figure 6.7 can be attributed to electrostatic versus strain interactions.

Several solute elements fall outside the blue band in Figure 6.7. For example, Cr and V have lower (more negative) binding energies than would be expected from their Bader charges if they were to follow the trends of most of the other solute atoms. Figure 6.5b shows that Cr and V have smaller Bader volumes than many other solutes, especially when compared to those with similar Bader charges. Their smaller volume will favor their proximity to the interstitial oxygen, which locally dilates the BCC crystal. Hence, a possible explanation for the lower binding energies of Cr and V is that strain interactions are more favorable for these elements than for others with similar Bader charges (and therefore similar short-range electrostatic interactions).

There are additional outliers in the upper orange triangle of Figure 6.7, with Si, Al, Y

and to some extent Zr having higher (more positive) binding energies in the first nearest neighbor shell of oxygen than would be expected from their Bader charges. In fact, all four of these elements have smaller radii than Nb (Figure 6.5b) and should also have a favorable strain energy contribution. Nevertheless, they have large binding energies, indicating that an additional mechanism is causing a significant energetic cost for a subset of first nearest neighbor X-O pairs. Previous studies on O-X interactions in a Ti host revealed the importance of a closed-shell repulsion that arises from the interaction between filled atomic orbitals when the solutes are brought in close proximity [115, 205]. This possibility for Si, Al and Y is explored next .

6.3.7 Closed Shell Repulsion Between Solutes

In a study of interactions between substitutional solutes and interstitial oxygen in Ti, Gunda et al [115, 205] revealed the existence of a closed-shell repulsive interaction due to the hybridization between filled atomic-like orbitals centered on the solute atoms. The effect was found to be especially pronounced for Si-O and Al-O solute pairs in a Ti host. A similar hybridization phenomenon involving closed-shell atomic-like orbitals occurs between interstitial oxygen and substitutional Si, Al and Y solutes within a Nb host. The closed-shell hybridization between solutes is apparent in the electronic density of states and is most clearly illustrated for the Si-O pair in BCC Nb.

Figure 6.8a shows the density of states of a supercell of BCC Nb (54 substitutional sites) containing a substitutional Si solute and an interstitial oxygen that are separated by a large distance. Once again, the oxygen p states are localized with energies far below the Nb states. The degeneracy of the oxygen p orbitals is lifted due to the asymmetry of the octahedral site in BCC, with the higher energy p orbital aligned with the shorter axis of the octahedron(Figure 6.8c) and the two other degenerate p orbitals aligned with the

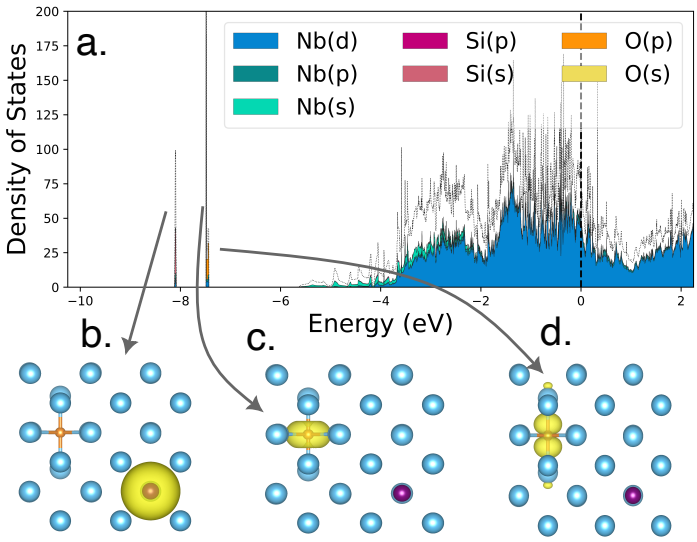

Figure 6.8: (a) The projected DOS is plotted for $Nb_{53}SiO$ where oxygen and silicon are about 7.35 Å apart. Isolated states about 8eV below the Fermi level correspond to the partial charge densities below. These states correspond to the fully occupied atomic orbitals from the silicon s orbitals(b) and oxygen p-orbitals (c,d). The Fermi level is indicated by a vertical dashed line at E=0 eV and the total DOS is plotted with a dotted line.

two longer axes of the octahedron (Figure 6.8d). The Si s orbital is also very localized and has a lower energy than the oxygen p states. All of these states are well below the Fermi level and are therefore fully occupied (Figure 6.8b). When Si is brought within the first-nearest-neighbor shell of oxygen, the localized s and p orbitals hybridize. This is evident in Figure 6.9a, which shows the electronic DOS for a configuration in which Si is a first-nearest-neighbor of oxygen. The oxygen p orbital that is aligned with the short axis of the octahedron hybridizes with the Si s state to form a lower energy bonding orbital (Figure 6.9b) and a higher energy anti-bonding orbital (Figure 6.9d). Since all participating orbitals are fully occupied, there is a significant energy cost to forcing this closed-shell interaction at such short distances. The other two p orbitals are only weakly affected by the neighboring oxygen as they are oriented orthogonal to the Si-O bond (Figure 6.2c).

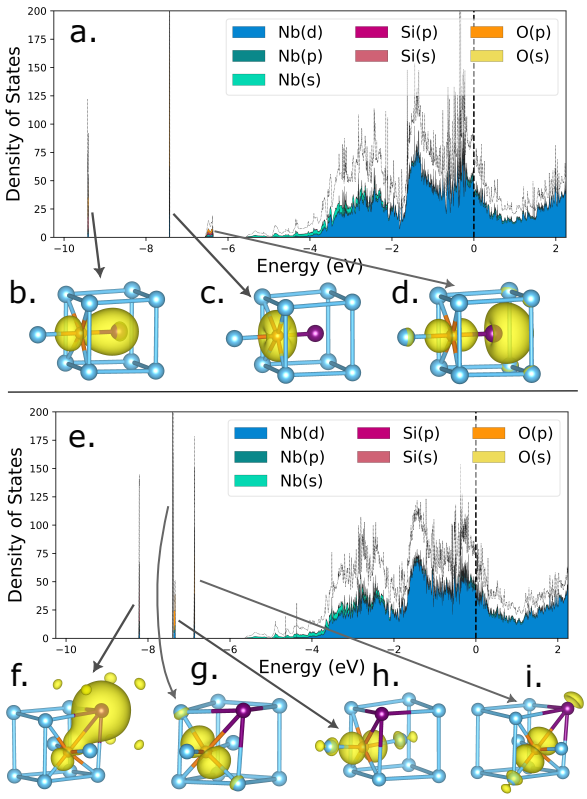

Figure 6.9: The projected DOS is plotted for $Nb_{53}SiO$ where oxygen and silicon are in the first(a) and second(d) nearest neighbor position. Isolated states between -10 and -6 eV below the Fermi level correspond to the partial charge densities shown below. These states correspond to the fully occupied bonding(b, and f), 2 nonbonding oxygen p orbitals (c, g and h), and antibonding orbitals (d and i). The Fermi level is indicated by a vertical dashed line at E=0 eV and the total DOS is plotted with a dotted line.

When oxygen occupies the second nearest neighbor site to a Si solute atom, a similar hybridization is predicted (Figure 6.8e). Once again a lower energy bonding state (Figure6.9f) and higher energy anti-bonding state (Figure6.9i) emerges. The bonding state has enhanced charge along the bond, while the anti-bonding state has a depletion of charge between Si and O. Since Si is no longer on the short axis of the octahedron, the degeneracy of the non-bonding states is broken, with a non-bonding oxygen p orbital aligned with the long axis that does not contain a Si solute (Figures 6.9g) and a second non-bonding oxygen p orbital pointing to the short axis (Figures 6.9h). Due to

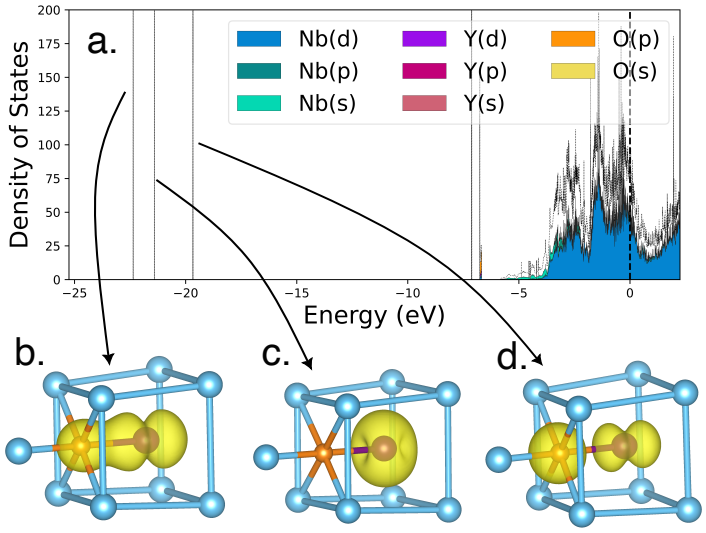

Figure 6.10: (a) The projected DOS is plotted for $Nb_{53}YiO$ where oxygen and yttrium are in the first nearest neighbor position. Isolated states about 22eV below the Fermi level correspond to the partial charge densities below. These states correspond to the fully occupied bonding (b), nonbonding (c), and antibonding orbitals (d) resulting from the hybridization of the yttrium p and oxygen s atomic orbitals. The Fermi level is indicated by a vertical dashed line at E=0 eV and the total DOS si plotted with a dotted line.

the larger distance between Si and O in the second-nearest neighbor configuration, the hybridization is weaker than in the first-nearest neighbor configuration, as manifested by a significantly smaller splitting between the bonding and anti-bonding states.

A similar closed-shell repulsive interaction is predicted for an Al-O solute pair in Nb, due to the hybridization between an Al s orbital and an oxygen p orbitals. The Al s orbital of an isolated Al solute far way from an oxygen atom sits slightly above the energy of the oxygen p orbitals, but still far below the Fermi level and is therefore fully occupied. When the Al and O atoms are brought together their orbitals hybridize into bonding and antibonding orbitals, much like the Si-O pair. The anti-bonding orbital is pushed higher in energy and approaches the bottom of the metallic states derived from the Nb host.

Closed-shell hybridization between substitutional solutes and interstitial oxygen can

also involve the deeper lying oxygen s orbitals. This occurs for the Y-O solute pair in Nb. Figure 6.10 shows closed-shell hybridization in the the first nearest neighbor configuration of a Y-O solute pair in BCC Nb. Here the oxygen s state and Y p states hybridize in spite of the fact that their energy levels are more the 20eV below the Fermi level. Clear bonding and anti-bonding states between O s and Y p orbitals form with charge distributions shown in Figure 6.10 b and d respectively. There is a significant energy penalty for pushing the electrons up in energy in the fully occupied antibonding orbital. A similar interaction is predicted between a first nearest neighbor Zr-O configuration involving a p state of Zr and an oxygen s orbital (Appendix C C7). The closed-shell hybridization involving the O s states are only evident in the first nearest neighbor configuration and are absent at larger distances. This is likely because the oxygen s atomic orbital is more contracted than the oxygen p atomic orbital, thereby limiting its overlap with orbitals on neighboring atoms to only very short distances.

Inspection of the electronic DOS plots for all substitutional solute-oxygen pairs in Nb indicates that the closed-shell hybridization described above is most pronounced in the solutes that have high binding energies, even when they have favorable Bader charges and Bader volumes. Both Al and Y, for example, have positive Bader charges and smaller Bader volumes compared to Nb, and are therefore expected to have negative (attractive) binding energies with oxygen. The closed-shell hybridization at short distances, however, leads to a repulsive interaction due to the filling of high energy anti-bonding orbitals. Zr also exhibits some degree of closed-shell hybridization with oxygen and is a possible explanation for the prediction that its binding energies is higher than expected based on the general trend of most other elements Figure 6.7.

6.4 Discussion

Refractory metals such as Nb can dissolve high concentrations of interstitial oxygen, with significant consequences for their mechanical properties and oxidation behavior [200]. Alloying of refractory metals is a common way of modifying oxygen solubility and oxidation behavior. In this study, we have sought to elucidate the electronic and chemical factors that determine the interactions between dilute substitutional solutes and interstitial oxygen in BCC Nb.

Our calculations have shown that an electronegativity difference between a solute and the surrounding Nb matrix, $\Delta\chi$, drives a transfer of charge and an accompanying change in volume of the solute. A useful measure of the extent of charge transfer between a solute and the surrounding matrix is the Bader charge [210, 211]. Similarly, the Bader volume of a dissolved atom [210, 211, 102, 103] is a more accurate reflection of the volume of a solute embedded in a matrix than its atomic volume in free space. Generally, elements that are less electronegative than Nb tend to transfer electrons to the host, accumulating a positive charge and reducing their volume. The opposite trends are predicted for solutes that are more electronegative than Nb.

The charge transfer and volume changes of solute atoms that are correlated with $\Delta\chi$ play an important role in determining solute-oxygen binding energies. This explains the strong correlation between X-O binding energies and the electronegativity difference $\Delta\chi$ in Nb that was revealed in an earlier study by Chen et al [206]. The local accumulation or depletion of electron density on substitutional solutes leads to short-ranged electrostatic interactions with interstitial oxygen. Since interstitial oxygen in Nb is negatively charged, due to the complete filling of its valence p orbitals, solutes with a positive Bader charge tend to attract oxygen, while those with a negative Bader charge repel oxygen. The electrostatic interactions should only dominate at very short distances, however, since

the Nb crystal is metallic with a high density of itinerant electrons at the Fermi level to screen charges at large distances. Strain mediated interactions between substitutional solutes and interstitial oxygen are also important. Interstitial oxygen induces a tetragonal strain on the surrounding crystal that can be partially relieved by substitutional solutes that are smaller than the Nb solvent. The size of a solute is found to correlate with its Bader charge, and by extension with $\Delta\chi$; Solutes that have a positive (negative) Bader charge due to electron loss (accumulation) are generally predicted to have a smaller (larger) Bader volume than that of Nb. Hence, the short-range electrostatic and strain mediated interactions work in the same direction and reinforce each other.

Short-range electrostatic and strain-mediated interactions do not explain the predicted trends in binding energies for all solutes. For solutes such as Si, Al and Y, our analysis has shown the importance of a close-shell hybridization that produces a repulsive X-O interaction at short distances. The hybridization involves localized atomic orbitals with energies below the Fermi level of the matrix and produces bonding and anti-bonding orbitals that are both filled. Similar closed-shell interactions were found between substitutional solutes and oxygen in a Ti host [115, 205].

Both attractive and repulsive interactions between substitional solutes and oxygen have been shown to slow oxygen diffusion in Nb. Attractive solutes that trap interstitial oxygen tend to slow diffusion more efficiently [209, 206], but may increase the solubility of oxygen in the alloy as in the case of Nb-Ti alloys [42]. Elements that have strongly repulsive binding energies can create an exclusionary zone around the solute atom, thereby restricting the number of sites that oxygen can visit and thus depressing oxygen movement and solubility [115].

A fundamental understanding of the underlying factors that determine X-O interactions in Nb can provide insights about similar interactions in other BCC metals and alloys. Short-range electrostatic interactions due to local charge transfer between solutes

and matrix likely play a role in other early transition metals as well. The current study has revealed the importance of charge transfer in affecting the solute volume when dissolved in the matrix. Solute size also plays a role in relieving or exacerbating the tetragonal strain fields induced by interstitial oxygen. The repulsive closed-shell hybridization, which is predicted here to be significant for some solutes in Nb and by Gunda et al for Ti [115, 205], is also likely to persist in most early transition metals and alloys since it is a function of the relative energy of core states of the solutes and of oxygen. However, the extent to which it manifests itself may be sensitive to the host crystal structure and lattice parameters as these geometric constraints affect the degree of overlap between the atomic orbitals that undergo rehybridization.

Many of the solute elements studied tend to form second phases when alloyed with Nb alloys. For instance, several of the studied elements (Sc, Ti, Y, Zr, Hf) form hexagonal closed-packed (HCP) crystals as a metal tend to form HCP phases in alloys [53, 55, 65]. Many of these elements are attractive to oxygen as solute in the BCC material. Previous work has noted that as regions near these HCP preferring element begin to undergoing a BCC to HCP transformation along the Burgers path, oxygen prefers their local environment[65, 130]. This has previously been attributed to the materials have significantly higher oxygen solubility in the HCP phase and oxygen preferring these HCP-like environments. However, in this study we see that even in a locally BCC environment, these elements attract oxygen more than the Nb matrix. This suggests that even before beginning the BCC-HCP transformation these elements attract oxygen. The transformation along the Burgers path and attraction to oxygen both in the BCC structure and HCP structure are likely symbiotic. An increase in oxygen concentration near HCP forming element will deform the lattice locally pushing the structure along the Burgers path. At the same time, a BCC lattice which has partially deformed along the Burgers path can trap interstitial oxygen which may further promote the structural transformation.

Meanwhile, other elements such as Ru and Al [57, 214] tend to form B2 precipitates in RMPEAS and are often specifically chosen to generate coherent precipitates. These elements may interact with interstitial oxygen as they diffuse to regions to form secondary phases. Elements such as Ru and Al tend to repel oxygen and may reject oxygen from their surrounding environment while diffusing into precipitates. Alloys designers must be careful to control the oxygen concentration through the heat treatment of these materials as dissolved oxygen which is expelled by the diffusing Ru may locally increase the oxygen concentration in the matrix which could lead to unexpected embrittlement or additional precipitation of oxide phases in the matrix. Such oxide precipitates could have strengthening effects if well controlled, though if deposited on defects or grain boundaries, could generate interior flaws which become nucleation points for crack generation and growth. Other B2 forming elements, such as Hf, attract oxygen and may pull oxygen along with them as they diffuse into the precipitates. If the oxygen concentration is appropriately controlled this could lead to an increased hardness of the B2 phase, while pulling interstitial atoms out of the softer matrix improving its ductility. Solute-oxygen interactions can thus have interesting impacts on the final morphology and properties of alloys and can provide an additional avenue for alloy designers to engineer new materials.

6.5 Conclusion

The binding energies between oxygen and 14 solute elements in two configuration in BCC Nb have been calculated from first principles. We have discussed how the relative electronegativity between the solute atom and the surrounding Nb matrix can influence the size and accumulated charge of the solute atom. These factors along with a repulsive interaction that emerges from a close-shell hybridization between localized atomic levels determine the solute-oxygen binding energies. Slowing oxygen diffusion and controlling

oxygen solubility is essential for alloy designers who are tasked with balancing the complex interplay of alloy weight, thermal performance, mechanical properties, and oxidation behavior to find an optimal material for a given application. These more in-depth relationships will allow alloy designers to accurately predict which solutes will getter oxygen or depress solubility to realize optimal oxidation behavior.

Chapter 7

Generalized Stacking Fault Energies in BCC Niobium with Interstitial Oxygen from First Principle

7.1 Introduction

Refractory metals such as niobium and its alloys dissolve large amounts of oxygen in an interstitial solution [8, 9, 13] which has been shown experimentally to cause embrittlement of these metals [200, 12]. Oxygen interstitials impose a significant tetragonal strain field on the BCC lattice due to the geometry of the octahedral site which they occupy. This strain field and that of other defects within the matrix, such as grain boundaries or dislocations will interact leading to accumulation of oxygen in regions where it can relieve the tensile strain in the crystal. One well known phenomena, caused by these strain mediated interactions, occurs when interstitial atoms accumulate below dislocations forming a Cottrell atmosphere which can impact dislocation movement[215]. At closer ranges to the dislocation, linear phase formations called linear complexions have been observed in

some materials [216, 217, 218, 219, 220] which can increase the hardening of materials. However similar shorter range linear complexes with interstitial oxygen in bcc materials have not been studied.

Work by Fey et al [221], used a phase field dislocation dynamics method based on the generalized stacking fault energies and elastic dipole interactions to study dislocation motion when oxygen was near dislocation in BCC niobium. Oxygen was seen to increase the energy required to move dislocations in the BCC material which lead to oxygen concentration dependant mechanisms of dislocation motion. The elastic dipole was also calculated and found to interact with the dislocation strain tensor when the dislocations were fixed in place. Oxygen would defuse to tensile regions surround the dislocation resulting in regions with interstitial concentrations which were twice that of the bulk nominal concentration [221]. It is thus reasonable to propose that oxygen could accumulate not only near but within a dislocation core, drastically changing the mechanisms of glide. Since plastic deformation in BCC materials is dominated by dislocations motion, it is important to understand how oxygen can alter their motion.

The generalized stacking fault energy (GSFE) is related to the Peierls stress for dislocation movement and is a quantity which can be directly calculated through first principle approaches [222]. First principles calculations of GSFE curves and traction curves have previously been applied to study decohesion and slip in the presence of interstitial atoms in both metallic and intercalation materials[223, 224] In this work, we will examine how GSFE curves are impacted when oxygen is allowed to accumulate within the glide plane itself. In BCC metals, slip typically occurs along the $\langle 111 \rangle$ which is the closest pack direction in the crystal. The $\{110\}$ plane contains two $\langle 111 \rangle$ vectors accounting for 12 $\langle 111 \rangle \{110\}$ slip systems in the crystal. The $\langle 110 \rangle$ direction also contained in the $\{110\}$ is not closed packed and but is useful for studying the extema of the GSFE curve in the glide plane. This study focuses on slip in the $\{011\}$ plane with and without oxygen

contained in the the glide plane. We find that oxygen can overall lower the energy range across the entire γ_{GSFE} surface. Furthermore, our results indicate local energy minimum correspond to the generation of preferential interstitial sites during slip.

7.2 Methods

The reader is referred to Chapter 3 for more details and background on the first principles methods used in this chapter. Vienna ab initio simulation package (VASP)[76, 77, 168, 169] was used to perform Density Functional Theory (DFT) calculations with the interactions between core and valence electrons treated using the projector augmented wave (PAW)[78, 79] method. The generalized gradient approximation (GGA) functional as parameterized by Perdew, Burke, and Ernzerhof (PBE)[75] was used with a 575 eV plane wave cutoff energy and Γ-centered k-point grid which was automatically generated with a density of 45 Å along each reciprocal lattice vector. Calculations were performed spin polarized and were initialized in a ferromagnetic state. All structures were relaxed at a constant shape and volume with only the oxygen atoms free to adjust their position to a convergence of 10^{-5}eV. The MultiShifter software package [225, 226] was used to generate supercells with incremental shears along the glide plane, as well as structures with a range of cleavage distances at each shear vector. Each calculation contained six layers of {110} Nb atoms between each glide plane. For each shear vector, an ultimate binding energy relation curve[227, 228, 229, 230] was fit to the surface energy as a function of cleavage distance to determine the minimum energy.

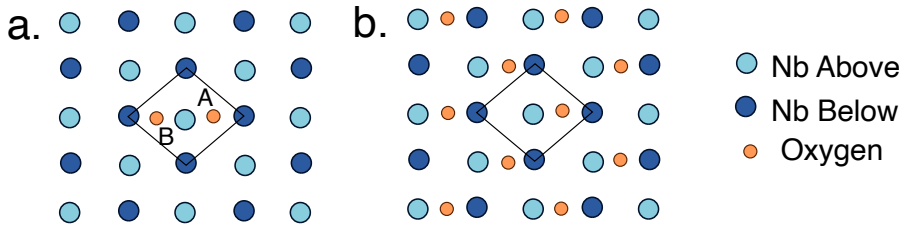

Figure 7.1: The {110} plane is shown with the Nb atoms on either side of the glide plane illustrate. (a) The unit cell is outlined with the two possible interstitial sties indicated by the A and B. (b) The {110} glide plane is illustrated where each A site is filled with an oxygen interstitial atom.

7.3 Results

A view of the {110} plane (Figure 7.1) shows the geometry of the slip plane in primitive unit cell used in this investigation with and without oxygen. For the Pure Nb, a grid of 12 x 12 incremental slip vectors were sampled across the the unit cell. When oxygen was present, GSFE curves were sampled at 22 increments across each Burgers vector. When oxygen dissolves in niobium, it prefers to occupy octahedral sites. In the BCC lattice, the octahedral interstitial site is asymmetric so when it is occupied by an oxygen atom, it imposes a tetragonal elastic dipole upon the surrounding matrix. There are actually two distinct octahedral sites in the {110} primitive cell (Figure 7.1a) which we will call site A and B. If both sites A and B s are occupied this would amount to occupying ever 2^{nd} nearest oxygen-oxygen pair in a plane. However this oxygen-oxygen pair is high energy and expected to be significantly suppressed even at high temperatures, as seen in Chapter 4 Figure 4.9. If only site A is occupied (Figure 7.1b), this would be equivalent occupying every 6^{th} nearest neighbor pair in a plane. This pair interaction is much lower in energy and much more likely to occur (Figure 4.9). Therefore only site A is filled at a time in the following calculations. Figure 7.3 illustrates how the tetragonal elastic dipole from an oxygen interstitial atom acts on the surrounding {110} planes at

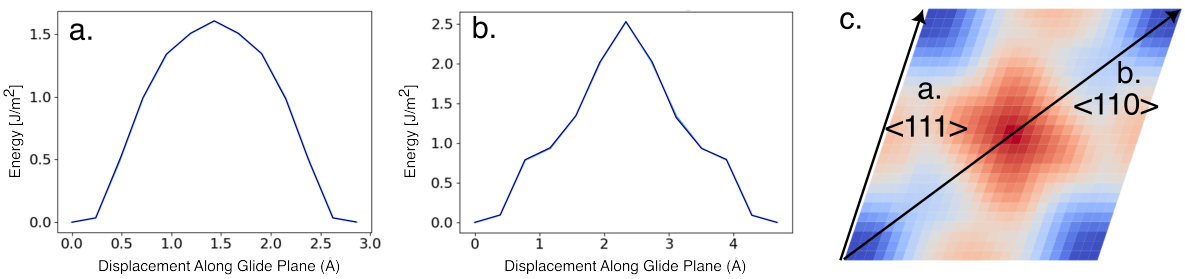

Figure 7.2: The GSFE curves for slip along the ⟨111⟩ (a) and ⟨110⟩(b) directions are shown with the γ_{GSFE} surface for the {110} plane shown in (c) for pure Nb.

an angle, applying both a stretch and shear. If oxygen atoms occupy only A sites, their dipoles will be aligned applying a net shear within the ⟨110⟩ slip plane.

7.3.1 GSFE curves and γ_{GSFE} surface in pure niobium

In Figure 7.2a, the γ_{GSFE} surface for slip in the {011} for pure Nb is shown. Each point in the surface defines the slip vector used in the calculation. The only local minimum in this surface is at the corners of the surface where the plane above the glide plane is unslipped. The GSFE curves (Figure 7.2 a and b) for each of the high symmetry directions are both symmetric with a higher energy peak found in the ⟨110⟩ direction than in the ⟨111⟩ direction, consistent with results in the literature and our expectations. Slip along the 111⟩ is preferred because the Burgers vector is smaller and the energy barrier between lattice points is lower than other high symmetry directions.

7.3.2 GSFE curves for dense layer of oxygen

The calculated the ⟨111⟩{110} and ⟨100⟩{110} GSFE (Figure 7.4) for a system with a dense plane of oxygen (Figure 7.1b) looks significantly different from those without oxygen. This calculation was performed in a unit cell with six {110} type layers which corresponds to a concentration of 14.3 atomic % oxygen. While this is higher than the

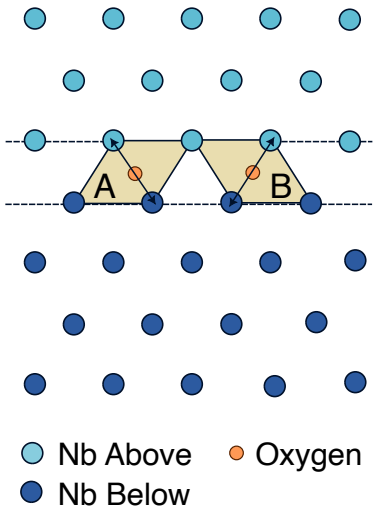

Figure 7.3: Each interstitial oxygen imposes a tetragonal distortion along one axis of the octahedra. Site A and B in the {110} plane are oriented so that the component of their tetragonal dipole which is parallel to the glide plane are opposing.

bulk oxygen solubility in niobium, it would be achievable with the 2-fold increase in local oxygen concentration at dislocations reported in Fey et al [221] at a nominal bulk concentration of only 7 atomic %. Along the ⟨111⟩ direction a new minimum has emerged about 0.9 Å from the origin with a second smaller local minimum about 2.25 Å from the origin (Figure 7.4a). Meanwhile along the ⟨110⟩ the curve looks drastically different with three local minima at about 1.0, 2.25, and 4.0 Å respectively (Figure 7.4b).

The energy range of each of these GSFE curves is significantly smaller than the GSFE curves without oxygen. While the peak energy for the unstable stacking faults along both the ⟨111⟩ and ⟨110⟩ are 1.55 J/m^2 and 2.5 J/m^2 respectively, the curves with oxygen span less than 0.7 J/m^2. This suggests that a dense layer of oxygen in the glide plane can significantly reduce the barrier to shear in both directions.

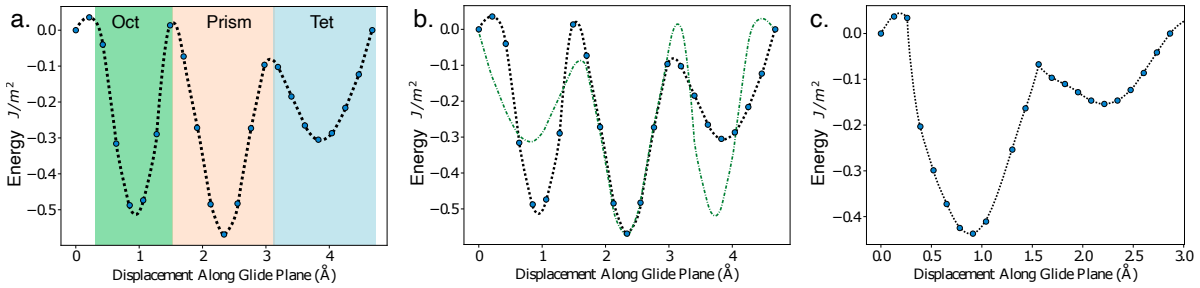

Figure 7.4: The GSFE curve for slip along the ⟨111⟩ (a, b) and ⟨110⟩(c) directions are shown for the {110} plane shown for the structure with a dense plane of oxygen in the glide plane. The regions in which the oxygen atom occupies different local coordinations (octahedral, prismatic, and tetrahedral) are noted in (a). The green dash-dotted line in (b) indicates the ⟨111⟩ GSFE curve for oxygen in Site B.

7.3.3 Interstitial geometry of local minima

Each of the local minima in the GSFE curves with oxygen correspond to a configurations in which the interstitial oxygen atom has found a locally favorable environment. Without oxygen present, the plane only has a minimum when the niobium atoms are aligned to the BCC matrix. Along the ⟨100⟩ direction, the GSFE is lowered to the first local minimum when the shearing of the neighboring planes stretches the oxygen octahedral environment along shorter axis of the site. The energy is lowered as the octahedron achieves a more optimal, symmetric geometry. Continuing to shear along the ⟨110⟩, the next minimum occurs at 1/2⟨110⟩, which was previously the highest energy point in the γ_{GSFE} surface in the absence of oxygen. In this geometry the oxygen interstitial environment evolves into a prismatic site. Finally if the structure is sheared further along the ⟨110⟩ vector, the shallowest of the local minimum corresponds to tetrahedral interstitial oxygen environment.

Similar structures are also observed at the local minima of GSFE curve along the ⟨111⟩ direction. At the first minimum the oxygen has square pyramidal coordination. This is clearly related to the octahedral site, but with lower symmetry which results in the oxygen atom relaxing to one side. A second local minimum occurs at 2.4 Å along

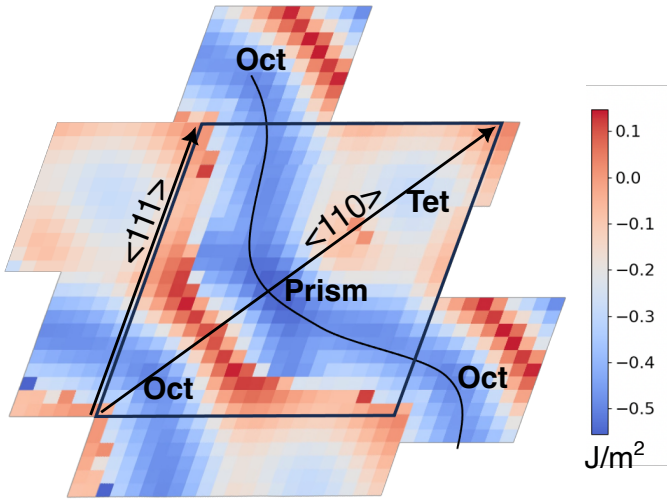

Figure 7.5: The γ_{GSFE} surface for the {110} plane with 1 oxygen atom per unit cell is shown which contain a new lowest energy path and three local minima.

the ⟨111⟩ where the oxygen is once again in a tetrahedral site similar to the one found along the ⟨110⟩ shear direction.

Oxygen interstitial atoms are mobile in the BCC matrix, so at elevated temperatures, or slow strain rates, the oxygen atoms may be able to diffuse to more favorable positions during shear. If the oxygen were to occupy site B instead of site A in the glide plane, the GSFE curve would be simply be a reflection of the GSFE curve for Site A. Therefore, if oxygen could diffuse, the lowest energy curve would allow the oxygen to diffuse from site A to site B after the a shear of 1.5 Å along the ⟨110⟩ or 3.0 Å along the ⟨111⟩ direction, ensuring that it is always in the lowest energy site.

7.3.4 The {110} γ_{GSFE} surface with dense layer of oxygen

Regions of the 2-dimensional γ_{GSFE} surface were calculated by initializing the interstitial atom at the nearest local minimum. A full γ_{GSFE} surface for the case with a dense layer of oxygen is shown Figure 7.5. This surface is significantly different from the surface calculated without oxygen (Figure 7.2c). This surface shows the γ_{GSFE} with the

assumption that the oxygen atoms is not allowed to diffuse from the initial site A to site B on the other side of the unit cell. While the corner of the unit cell is no longer an energy minimum, there is a minimum at about 1 Å along the ⟨110⟩ direction where oxygen is in an optimized octahedral site. The energy is smoothly varying between the octahedral site minimum along the ⟨110⟩ direction and the pyramidal site along the ⟨111⟩. The configuration with a pyramidal is a saddle point between those with the oxygen in either an octahedral site or a prismatic site. There is a low energy and smoothly varying path across the unit cell, where the oxygen atoms moves from the octahedral site, through the pyramidal saddle point to a prismatic site then through to another pyramidal saddle point before recovering the octahedrally coordinated site after the top slab has slip into the next unit cell.

7.3.5 GSFE for moderate layers of oxygen

Thus far we have examined the extreme surface concentrations of oxygen, both high and low and found that the slip behavior varies significantly. To examine how this slip behavior changes as the oxygen concentration is varied, a unit which is twice as large was also examined. In this unit cell one of the ⟨111⟩ lattice vectors was twice as long extending to another unit cell. The oxygen concentration was thus cut in half as only one oxygen cite was occupied in the supercell, resulting in a glide plane with alternating rows of oxygen interstitial atoms (Figure 7.6). This corresponds to a local concentration of 7.69 atomic % oxygen. Since the local oxygen concentration is amplified by 2x at a dislocation, this could be observed in a bulk concentration of only 3.85 atomic %. In this unit cell, the two ⟨111⟩ vectors are no longer symmetrically equivalent. The GSFE curves for the ⟨110⟩ and two ⟨111⟩ directions are shown in Figure 7.7. Each curve has a minimum corresponding to the octahedral site (Figure 7.8a) or pyramidal site, similar to the GSFE

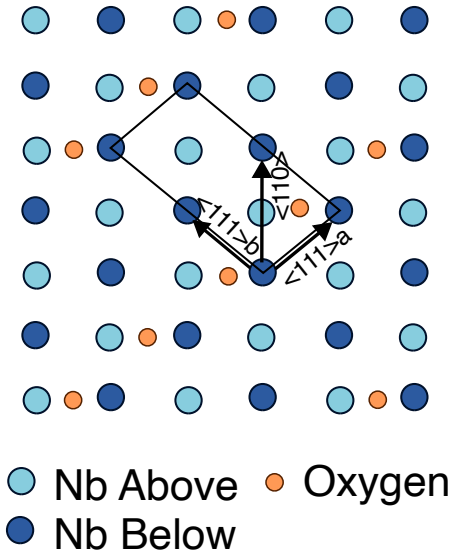

Figure 7.6: The {110} plane is shown with the Nb atoms on either side of the glide plane illustrated. Here a larger unit cell is shown where only half of the A type interstitial sites are filled with oxygen resulting in every other row of oxygen sites filled.

cruves in denser oxygen layer. However along the ⟨111⟩ direction with alternating rows of oxygen, the minimum is shallower in energy. Along the ⟨110⟩ direction, the prismatic site (Figure 7.8b) is no longer a globally favorable configuration, though it is a local minimum along the ⟨110⟩ vector. The tetrahedral site (Figure 7.8c), while still observable at shears greater than 4Å along the ⟨110⟩ or 2 Å ⟨111⟩, is not a local minimum along the either direction. The overall energy range of the curve is still smaller than in the GSFE curves without any oxygen present.

7.4 Discussion

When oxygen is present in the {110} fault plane it can dramatically alter the γ_{GSFE} surface both quantitatively and qualitatively. The energy range of GSFE curves in all calculations with oxygen are are least half of that in the absence of oxygen suggesting

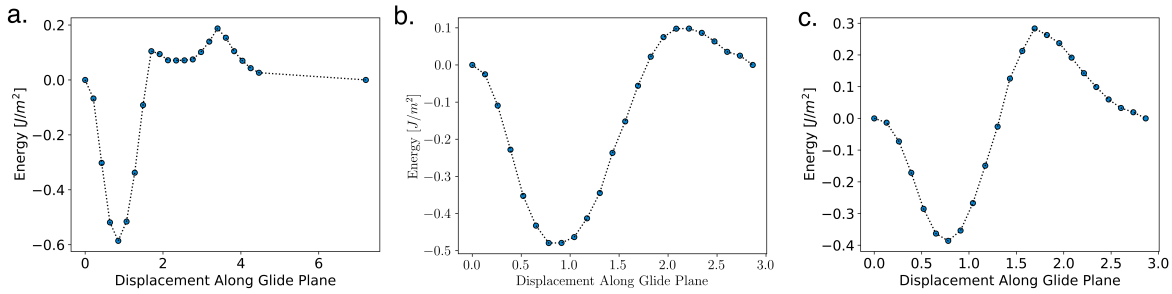

Figure 7.7: The GSFE curve are shown for the ⟨110⟩(a) and two distinct ⟨111⟩(b, and c) vectors in a supercell where half the A type oxygen sites are occupied which are labeled as ⟨111⟩a and ⟨111⟩b Figure 7.6.

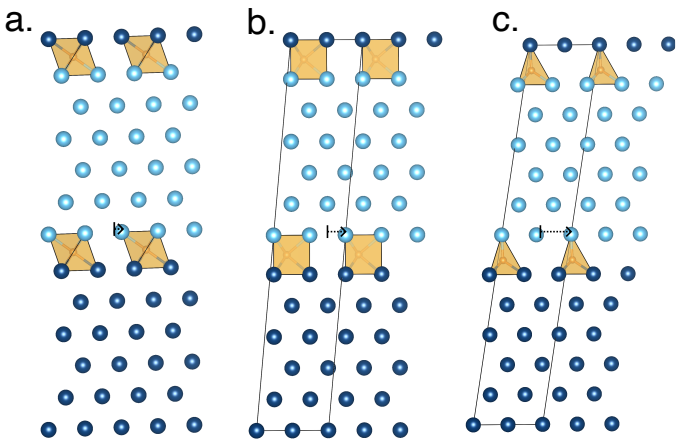

Figure 7.8: Over the course of slip along the ⟨110⟩ vector, the oxygen interstitial atom occupied three different site, and octahedral site (a), and prismatic site (b), and a tetrahedral site(c). The dark blue Nb atoms are below the slip plane while the light blue Nb atoms are above.

that oxygen can significantly lower the Peierls stress. The topology of the energy surface is significantly different in the presence of oxygen as shear vectors which result in favorable interstitial sites are preferred over those which recover an ideal BCC lattice. This preference for optimizing the interstitial environment is reduced as we decrease the oxygen concentration. Ultimately, interstitial oxygen changes the preferred slip direction, to a path through the lowest energy interstitial site. If slip is forced through the ⟨111⟩ direction in the presence of oxygen, the energy barrier would still be reduced. Further-

more, if oxygen was able to diffuse between site A and B, this could further reduce the energy barrier for this slip direction.

As a BCC material, dislocation motion is largely dominated by kink-pair nucleation. Since this process is typically thermally activated, mobile oxygen atoms may play a role in lowering the barrier for the nucleation of these pairs.

7.5 Conclusions and Future Directions

The presence of oxygen in a slip plane can dramatically change deformation mechanisms in BCC niobium. While this study was limited to one slip plane, and only two arrangements of oxygen, these findings could profoundly alter how we expect oxygen to interact with dislocations in BCC materials. While the local concentration of oxygen studied in this chapter may seem higher than is typically seen in bulk Nb or approaching the maximum solubility, the presence of a dislocation can lead to a local oxygen concentration which is twice that seen in the bulk material [221] Thus the oxygen concentrations in this study can be observed near defects at relevant experimental oxygen concentrations. The γ_{GSFE} surface is a result of the competing energetic benefits of recovering an ideal BCC metal lattice and providing an optimal interstitial site for the oxygen atom. Clearly at the dilute extreme, the former will win out, while we have shown that providing an optimal interstitial environment becomes a dominant factor at higher concentrations of oxygen. More research is need to determine this transition as a function of oxygen concentration.

Since interstitial oxygen is a mobile species in the bcc lattice, the γ_{GSFE} surface will be impact by the interstitial atoms ability to diffuse during the slip event. This mobility will vary as a function of temperature, strain rate, and slip vector. The oxygen atom may have very steep diffusion barriers from some sites when partially slipped, but not

other. For instance, the octahedral site may be more difficult to diffuse from than the prismatic site. Further investigation will be needed to tease out these nuances.

Future researchers should also work closely with experimentalists who are studying the role oxygen in BCC refractory alloys. STEM and TEM methods may be able to identify slip behavior including the formation of stacking faults or slip on systems such as those discussed in this chapter which would be lower in energy in the presence of oxygen but unexpected without it present. Rate and temperature dependant tensile and compression tests with varied amounts of oxygen as well as in situ tensile tests could further elucidate the effect oxygen and oxygen diffusion have on the deformation mechanisms in BCC metals. It would also be of interest to vary the matrix composition from a simple BCC interstitial solution such as pure niobium, to a binary alloy system such as Nb-Ti, to a multi principal element alloy. If the BCC lattice is less idealized in the matrix, lower concentrations of oxygen may be necessary for the oxygen interstitial environment to dominate the slip behavior. Alternately, a larger lattice parameter or stiffer matrix could lead to a smaller oxygen elastic dipole reducing its ability to impact slip in the material. Both experimental work and additional calculations are needed to fully understand this phenomena and its role the deformation of BCC alloys.

Chapter 8

Conclusion

In this thesis, a first principles investigation of the phase stability Nb-O binary system and the behavior of oxygen solutes in BCC niobium was presented. Throughout this work, I strove to not only describe but provide a physical explanation for the behavior of the system.

In the Wadsley-Roth study, a wider range of of crystallographic possibilities were explored than had previously investigated while a systematic nomenclature was defined to facilitate discussion. These crystal structures span a continuum between rocksalt and the perovskite like WO_3. Additionally many important materials such as the TiO_2–B can be described by this crystallographic family. This framework and nomenclature are intended to aide in the design of new Wadsley-Roth oxides and the continued study of this promising class of Li-ion battery materials.

First principles calculations demonstrated that the $E_1[n \times m]$ shift type structures were consistently preferred due to a balance of electrostatic considerations and atomic relaxations. The number and orientation of octahedra edge sharing instances in each structure were effective indicators of each of these energetic contributions. This analysis is the first explanation for the tendency for the $E_1[n \times m]$ seen in Wadsley-Roth phases

reported across the literature. In addition, our collaboration with Muna Saber [14] also demonstrated how similar logic can be applied to explain the cation ordering preferences in Ti-Nb-O Wadsley-Roth structures. The ordering of cations in these and other Wadsley-Roth structures can have significant impact on the Li-ion intercalation mechanisms and kinetics. It is therefore essential to accurately predict the cation ordering in mixed Wadsley-Roth oxides when studying their Li-intercalation behavior.

One theme revealed across this body of work is the complex interplay of strain mediated effects and electronic interactions in determining the relative phase stability, defect formation, and solute-solute interaction energies. In the vacancy ordered rocksalt NbO phase, partial filling of anti-bonding π orbitals strongly destabilized a defect which plugged a vacancy on the oxygen lattice. This structure, unexpectedly, strongly favors an additional niobium vacancy defect over other point defects. The short range interactions of oxygen-oxygen interstitial pairs in BCC niobium, similarly were destabilized when overlapping p-orbitals hybridized resulting in closed-shell bonding and antibonding interactions deep below the Fermi level. This repulsive interaction significantly outweighed electrostatic interactions of many short range O-O pair interactions. Overall, interstitial O-O pair interactions were derived from a combination of electrostatic, closed-shell bonding and strain mediated effects due to the tetragonal elastic dipole. The strong short range interactions led to significant preference for pair interactions which resulted in short-range ordering of interstitial atoms persistent to high temperatures. The high solubility both predicted here, and observed in literature [18, 44, 45, 42, 46] suggest, that this non-ideal behavior of oxygen interstitials may contribute to deviations from ideal behaviors. For instance, pair interaction will impact diffusion kinetics, while the preferential order could play a role in phase transformation pathways.

In Chapter 6, similar themes were studied in the context of the dilute Nb-X-O alloys. Here, electrostatics played a dominant role. Bader analysis revealed electronegativity dif-

ferences between substitutional solute and a niobium matrix caused charge accumulation and solute size changes for substitutional elements. Oxygen also accumulated a negative charge resulted in electrostatic interactions which to first order determined the stability of the X-O pairs in the Nb matrix. However some X-O pairs, particularly at the first nearest neighbor distance defied this simple trend. Some solute were very small, which further lowered the energy of the X-O pair, while other pairs experienced a destabilizing closed-shell bonding interaction. Some of these closed-shell bonding interaction, such as Zr-O, included states deep below the Fermi level, such as the Zr-p orbitals.

This thesis is closed out with a brief but exciting study of the impact of interstitial oxygen atoms on GSFE when they are located within the glide plane. Interstitial oxygen could profoundly alter the energy landscape suggesting a potential to drastically alter dislocation behavior. When significant oxygen is present the GSFE curve reflect a preference for shear vectors which optimize the interstitial coordination environment, often at the expense of the BCC lattice. The energy range of the entire γ_{GSFE} surface is also significantly decreased suggesting that the material could be drastically softened. This scenario is further complicated by the mobile nature of the interstitial oxygen atoms. Further study could reveal the temperature, rate, and compositional dependence of the dislocation glide behavior on interstitial oxygen.

8.1 Future Directions

The work presented in this thesis illuminated key mechanistic details underlying the behavior of oxygen as an interstitial solute in niobium, as well insights into the driving forces behind phase stability across the Nb-O binary system. These results lead to further questions about the phase stability and behavior of refractory alloys and oxides which we are now more well equipped to address.

The study of Wadsley-Roth oxide phases in Chapter 5 details a systematic way to study this broad class of oxides. While most of the literature focuses on the application of these oxides as anode materials, Wadlsey-Roth phases with multiple cations and cation disorder also play a role in depressing oxidation rates in RMPEAs [10, 65, 66]. Since these oxidation processes are typically driven by oxygen diffusion through the oxide scale and into the metal substrate, it is essential to understand the mechanism of oxygen diffusion through Wadsley-Roth crystal structures. The mechanism of oxygen diffusion, crystallographic shear plane migration, and Wadsley-Roth oxide formation remain open questions in the research community. Several theories of shear boundary formation and migration have been proposed [231, 232, 233]. Since an increase in the density of these shear planes reduces the local oxygen concentration, these planar features could diffuse in the opposite direction from oxygen diffusion. Many of the proposed migration and growth mechanisms required coordinated motions of many atoms to shift and entire shear boundary or part of a boundary. Vacancy mediated diffusion of oxygen through the oxygen sublattice may also provide a means to diffuse oxygen through the oxide. Oxygen diffusion through the square tunnels between corner sharing octahedra could also productive a means for oxygen diffusion.

A first principles approach could explore the relative energies associate with each of these diffusion mechanisms and any associate intermediate states. The energy barriers for these diffusion mechanisms would indicate which mechanism is most likely to occur and whether more than one might be observed at higher temperatures. These calculations could be repeated for oxides with different $E_1[n \times m]$ structures. Similarly, these calculations could also be repeated in structures with a mixture metal cations. This can provide insights in how the diffusion mechanism is influenced by oxide composition and cation ordering. The results may indicate that certain metal cations tend to slow diffusion or change the dominant diffusion mechanism.

In Chapter 6, we developed a nuanced understanding of the X-O pair interactions in the dilute niobium alloys providing a baseline from which to compare X-O interactions in more complex alloys. If we consider a refractory multi-principal element alloy, it is not as straightforward to compare the electronegativity for a given constituent element to the surrounding matrix. The alloy average, local neighborhood, or nearest neighbors atoms may be relevant points of comparison. While we have only considered the dilute alloy, the degree of charge accumulation may be tied more explicitly to composition. At first glance, we would not expect a significant change in the closed-shell bonding X-O interactions in other BCC alloys, as they are a result of the relative levels of the atomic core states. However, the change in lattice parameter upon alloying may somewhat change the relative energy level of core states and could also tune the degree of overlap due to the different bond distances. These uncertainties warrant further investigation in more complex alloys.

A number of straightforward studies could elucidate some of these questions by extending this computational approach to study the solute binding energies in alloys as a function of composition. It would be simple to first change out the matrix element from Nb to another BCC element such as W or Mo which have much higher electronegativity. By comparing the binding energies, Bader charges, and volume changes of solute elements in the the similar dilute alloy may confirm the electronegativity driven charge transfer. This study could also prove an effective way to test the persistence of the closed-shell bonding effects in another BCC materials with a different lattice parameter.

It is of particular interest to understand how solute-oxygen interactions change as a function of the matrix composition. For instance, alloy designers may wish to effectively predict how key elements such as Re or Ru, which are often used to increase ductility, or of Hf and Zr which are often used to getter oxygen and reduce weight, have different solute-oxygen interactions in different matrices. From a computational perspective, a

solute of interest could be tested by first generating a number of alloy supercells could be generated for a set of compositions. For instance, a sample of Nb-Mo-Ti special quasirandom supercells could be generated across a range of compositions. For each unique interstitial site the oxygen binding energy could be calculated. Then Bader analysis with a focus on each of the six coordinated atoms could address some open questions such as whether the solute behavior is driven by the first nearest neighbor charge, or if is strongly dependent on the six coordinated atoms. Furthermore, considering this behavior as a function of alloy composition and local environment will illuminate how these effects are changed by the matrix environment. While the electronegativity difference between the solute and the Nb matrix drove charge transfer and solute size changes in dilute Nb alloys, it is unclear how this translates into a more compositionally complex environment. Charge transfer could be dependent on a atoms electronegativity compared to the nearest neighbor atom electronegativities, the total matrix average electronegativity, or some intermediately sized environment.

Experimentalists may be most interested in how these solute interactions impact the composition and properties of multiphase refractory alloys. To study the possibility of some atoms pulling oxygen into precipitates or rejecting oxygen from precipitates into the matrix, experimentalists could generate an alloy with a range of controlled oxygen concentrations. Then the oxygen concentration could be measured in each phase of heat treatment which involved a second phase formation. Additional SEM and characterization of the grain morphology and phase compositions would be necessary to identify whether oxide formation occurred.

8.2 Closing Remarks

Throughout this thesis, I sought to develop a mechanistic understanding of Nb-O phase stability and solute interactions which will aid to alloy designers and battery engineers alike. The insights generated and methods applied led us to new interesting questions about the stability and behavior of other refractory alloys and oxides. This work brings us one step closer to a complete understanding of these fascinating material systems which can transform the technologies that shape our world.

Appendix A

Supplementary Information for the Thermodynamic Evaluation of the Nb-O Binary

A.1 Oxygen Interstitial Atom Lattice Distortions

An oxygen interstitial atom in an octahedral site in the BCC niobium imposes a tetragonal elastic dipole on the surrounding matrix. Although the overall effect is dilational, atoms along the waist of the asymmetric octahedron are drawn closer to the oxygen atom.

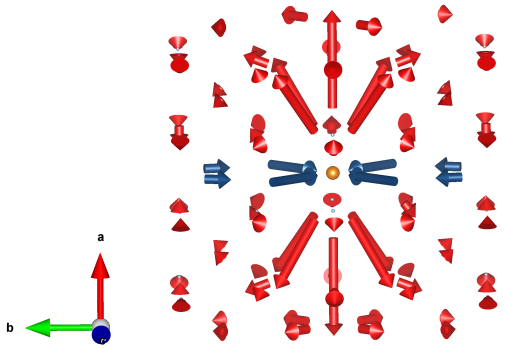

Figure A.1: The displacement vectors, amplified by a factor of 300, are illustrated for the atoms in a 128 Nb atom BCC cell with one interstitial oxygen atom. The displacement of the first nearest neighbor atoms is excluded for clarity,though they are an order of magnitude larger than the displacements rest of the cell. The displacement vectors which point toward the oxygen interstitial atom are shown in blue and are only found along the waist of the octahedral site. The rest of the displacements in red lead to an overall dialational elastic dipole.

A.2 Grand Canonical Defect Energies

The grand canonical potential energy for a given configuration σ is defined as

$$\Omega(\sigma) = E(\sigma) - \sum_i \mu_i n_i(\sigma) \tag{A.1}$$

where $E(\sigma)$ is the total energy of the configuration and μ_i and n_i are the chemical potential and number of atoms of each i component of the material. From this, the grand canonical defect potential energy, $\Delta\Omega_d$, is defined from the difference between the grand canonical energy of a structure with a particular defect and the pristine ground state structure.

$$\begin{aligned}\Delta\Omega_d &= E_d - \sum_i \mu_i x_{id} - (E_0 - \sum_i \mu_i n_{i0}) \\ &= \Delta E - \sum_i \mu_i \Delta n_i\end{aligned} \tag{A.2}$$

Here E_0 and E_d are the total energy of the ideal structure and defected structure respectively.

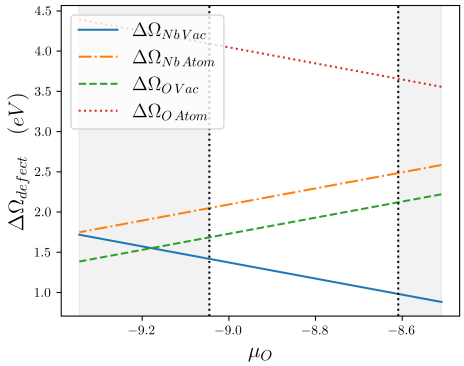

Figure A.2: The grand canonical defect energy for the four point defects in NbO was calculated. The white region in the center of the plot is the chemical potential window in which NbO is the stable ground state, and across this entire range the Nb vacancy defect is lowest in energy. When μ_O is lowered the BCC niobium phase becomes stable while at higher μ_O the Nb_3O_7 phase becomes stable. Dashed vertical lines represent two phase equilibria.

Figure A.2 shows $\Delta\Omega_d$ as calculated for the four point defects in the NbO rocksalt ground state as a function of μ_O. These values are based on the DFT calculated energies of the pristine vacancy ordered rocksalt supercell with 162 atoms and the same supercell containing a point defect after atomic relaxations. The relevant chemical potential window was determined from the convex hull.The value of μ_O can be written in terms of μ_{Nb} as follows:

$$\mu_O = 2E_0 - \mu_{Nb} \tag{A.3}$$

At $\mu_O = -9.045$ eV, denoted by a vertical dashed line in Figure A.2, BCC Nb and NbO

are in a two phase equilibrium. At lower μ_O BCC Nb is the stable phase. Similarly, when $\mu_O = -8.61$ eV the rocksalt is in equilibrium with the Nb_3O_7 ground state which becomes the stable ground state at increased μ_O.

Across the μ_O window in which the rocksalt phase is stable, the Nb vacancy defect has the lowest $\Delta\Omega$ out of all possible point defects while the extra oxygen atom defect is highest in energy. If the BCC phase formation were suppressed and μ_O were reduced to below -9.18 eV, then the oxygen vacancy would become the most stable defect. However, this is fairly far into the chemical potential range in which BCC niobium is stable, so it is unlikely to be realized in an experimental setting.

A.3 Rotated Orbital Basis

The orbital basis was rotated by 45 degrees about the y axis to align the z' axis with the vector between two Nb atoms as shown in Figure A.3. This allowed the *sigma* bonds and *pi* bonds between neighboring Nb atoms to be more directly examined with -COHP analysis.

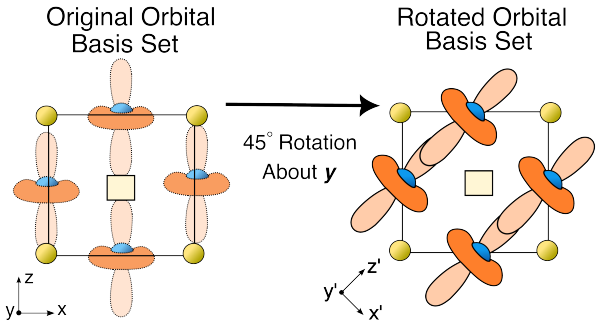

Figure A.3: The original basis set in the Cartesian coordinate system was rotated by 45 degrees about the y-axis was used to study the Nb-Nb interactions in the pristine NbO system. This aligns the $d_{3z^2-r^2}$ orbitals of neighboring Nb atoms as shown.

A.4 Electronic Structure of NbO with Defect

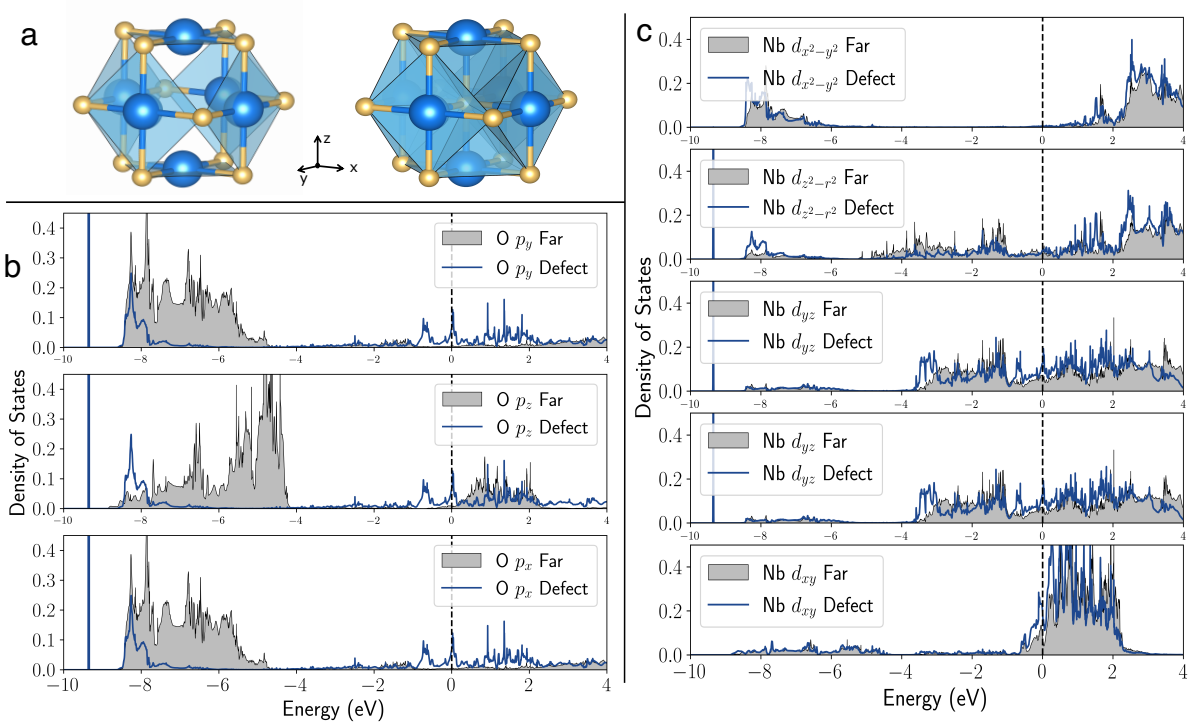

Figure A.4: Part a shows the idealized NbO crystal structure where the blue spheres represent niobium atoms and the small yellow one s are oxygen atoms. On the right is an idealized NbO crystal structure with an additional oxygen atom plugging a vacancy. Part b shows the projected density of states for the *p*-orbitals of two oxygen atoms while part c shows the projected density of states for the *d*-orbitals of two niobium atoms in a 163 atom supercell. The filled grey curve is the projected DOS from atoms in a square planar environment far from the oxygen defect atom while the blue line is the DOS projected onto the extra oxygen atom or niobium atom directly below the extra oxygen atom. The dashed vertical line at E=0 indicates the Fermi level.

The electronic structure of NbO structure with an extra oxygen atom filling a vacant site reflects the octahedral coordination environment the oxygen atom has been placed in (Figure A.4a) and the changing the coordination environments of the surrounding six niobium atoms from a square planar symmetry to that of a square pyramid. The projected density of states for oxygen *p*-orbitals and Nb *d*-orbitals was calculated in a $3 \times 3 \times 3$ supercell with an additional oxygen atom allowing atomic relaxations. In

Figure A.4b, the projected density of states of the oxygen p-orbitals are examined where the grey filled curve correspond to the states related to an atom with square planar geometry distant from the defect such that the p_z orbital points into the vacancy. The blue line indicates the oxygen p-states related to the additional oxygen atom. Each of these orbitals contributes to a narrow band about -9.0 eV below the Fermi level. There are also a few additional peaks near and just below the Fermi level.

Figure A.4c shows the projected density of states of the niobium d-orbtials where the grey filled curve are the states related to an atom with square planar geometry distant from the defect such that the $d_{z^2-r^2}$ orbital points into the vacancy. The blue line indicates the oxygen d-states related to the Nb atom directly below the extra oxygen atoms, such that the $d_{z^2-r^2}$ orbital points at the defect. The $d_{x^2-y^2}$ density of states, shown at the top of A.4c, is largely unaffected by the change in coordination environment. In contrast, the next three orbitals in A.4c, the d_{z^2-r2}, d_{yz}, and d_{xz}, all acquire some contribution to a narrow band near -9.0 eV relative to the Fermi level. This narrow band matches that seen in oxygen p-orbitals and indicates a new bonding interaction with the neighboring oxygen atom. For the $d_{z^2-r^2}$ orbital, this is mostly a strong σ-bond which pushes some of the density of states further above the Fermi level. However, for the the d_{xz} and d_{yz} in A.4c, this interaction is a weaker π-bonding interaction which does not result in as significant splitting. These two orbitals also have two smaller spikes at and just below the Fermi level which match those seen in the defect oxygen p-orbitals. This π-bond would be similar to the B_{2g} states in Figure 4.11b which has antibonding states just above the Fermi level in the pristine crystal structure. Similarly, in Figure A.4e, the d_{xy} orbital also experiences additional filling of states which are pulled lower in energy.

Appendix B

Supplementary Materials for Chapter 5

B.1 Algorithm for the enumeration of Wadsley-Roth block structures

To generate an arbitrary Wadsley-Roth block structure of type $E_{i\alpha}[n \times m]$ or $T[n \times m]$, a set of lattice vectors for a primitive cell is defined and then populated with a grid of corner sharing octahedra representing a single block motif. This starts in Cartesian space with the origin at the metal cation in the bottom left corner octahedron of block A oriented such that the cation-oxygen bonds of the idealized octahedron are aligned with the x, y, and z axes. By convention the $n \times m$ block motif sits in the x-y plane. In figure B.1 the origin sits on the central niobium atom of the bottom left corner of Block A. Primitive lattice vectors $\vec{a}$ and $\vec{b}$ are then selected that connect the cation of the corner octahedron at the origin to the cation in the similar corner octahedra of neighboring blocks B and C as shown in figure B.1. The $\vec{c}$ lattice vector accounts for height of a

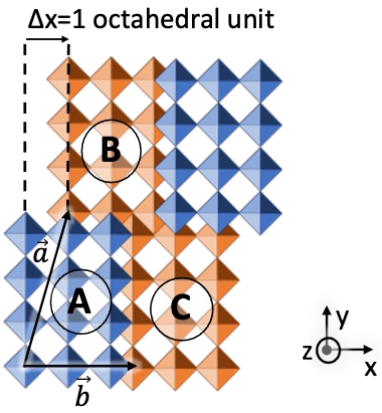

Figure B.1: The lattice vectors $\vec{a}$ and $\vec{b}$ are illustrated for an $E_{1x}[3 \times 4]$ Wadsley-Roth structure.

single layer of octahedra. These lattice vectors can be written as follows:

$$\vec{a} = \begin{bmatrix} \Delta x d \\ md - \frac{d}{2} \\ \frac{d}{2} \end{bmatrix} \quad \vec{b} = \begin{bmatrix} nd - \frac{d}{2} \\ \Delta y d \\ \frac{d}{2} \end{bmatrix} \quad \vec{c} = \begin{bmatrix} 0 \\ 0 \\ d \end{bmatrix} \tag{B.1}$$

Here d is the distance between two niobium atoms in adjacent corner sharing octahedra. Once this lattice is defined, an octahedron centered at each position in the Cartesian space is placed

$$\vec{p} = \begin{bmatrix} kd \\ ld \\ 0 \end{bmatrix} \tag{B.2}$$

where k and l are integers in the intervals (0, n] and (0,m], respectively. Lastly, all atomic positions defined by Cartesian coordinates, some of which may lie outside of the first unit cell, is converted into fractional coordinates within the primitive unit cell defined above. To enumerate $E_{ix}[n \times m]$ ($E_{jy}[n \times m]$) structures, i (j) ranges between 0 and $i = n - 1$ ($j = m - 1$).

B.2 Dependence of relaxation energies of Nb_pO_q WR-phases on the nature of shared edges

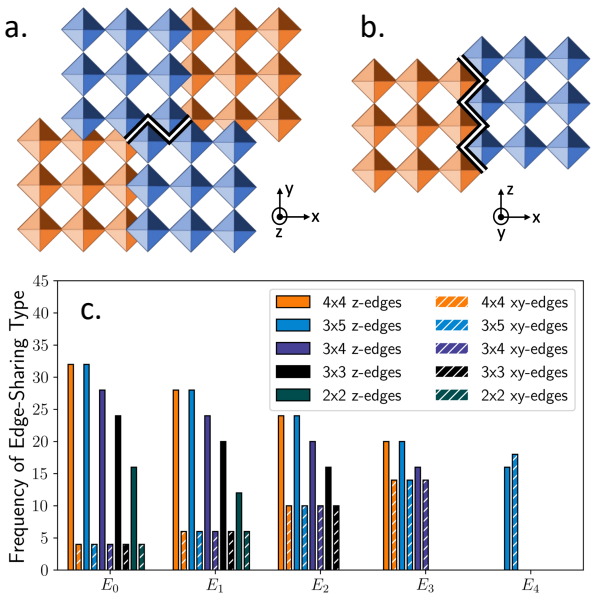

Figure B.2: Wadsley-Roth shear structures have octahedra that share edges that are (a) oriented parallel to the $\hat{x}$-$\hat{y}$ plane (x-y-edges) and (b) oriented out of the $\hat{x}$-$\hat{y}$ plane (z-edges). (c) The number of x-y-edges steadily increases with block shift i.

The variation in the relaxation energy for the $E_{i\alpha}[n \times m]$ Nb_pO_q structures with $i > 0$ is correlated with the frequency of different orientations of the shared edges. Wadsley-Roth structures have varying numbers of shared octahedral edges that reside within the $\hat{x} - \hat{y}$ plane (xy-edges), highlighted in black in Figure B.2(a), and shared octahedral edges that are oriented out of the $\hat{x} - \hat{y}$ (z-edges), as illustrated in Figure B.2(b). Figure B.2(c) shows that the number of shared octahedral edges that lie in the $\hat{x} - \hat{y}$ plane increases as the relative block shift i increases. Figure B.3 shows the correlation between the relaxation energy and the fraction of xy-edges for $E_{i\alpha}[n \times m]$ with $i > 0$. Each set of points connected by a line have the same number of shared edges. They do differ by the fraction of shared xy-edges to total number of shared edges. For a fixed number of edges

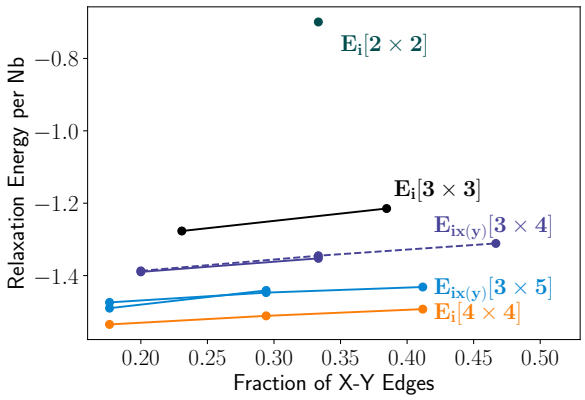

Figure B.3: The relaxation energy per Nb if plotted versus the fraction of x-y edges for E_{ix} and E_{jy} for each of the examine $[n \times m]$ block structures.

per Nb, the correlation between relaxation energy and fraction of xy-edges is reasonably linear for the $\mathrm{E}_{i\alpha}[n \times m]$ structures with $i > 0$. Figure B.3 suggests that as the shift between neighboring blocks i increases, the increasing number of in-plane edges limits the degree with which the structure can relax, thereby reducing the energy gain during relaxation.

Appendix C

Supplementary Materials for Chapter 6

Bader charge analysis was performed on similar unit cells with 53 Nb atoms and 1 substitutional atom X (X=Al, Si, Sc, Ti, V, Cr, Y, Zr, Mo, Ru, Hf, Ta, W, or Re) both with and without an interstitial oxygen atom present. The interstitial atom can be either in the 1st or second nearest neighbor site. The Bader charge was also calculated on the oxygen atom at the 1st nearest neighbor site and the distant reference site.

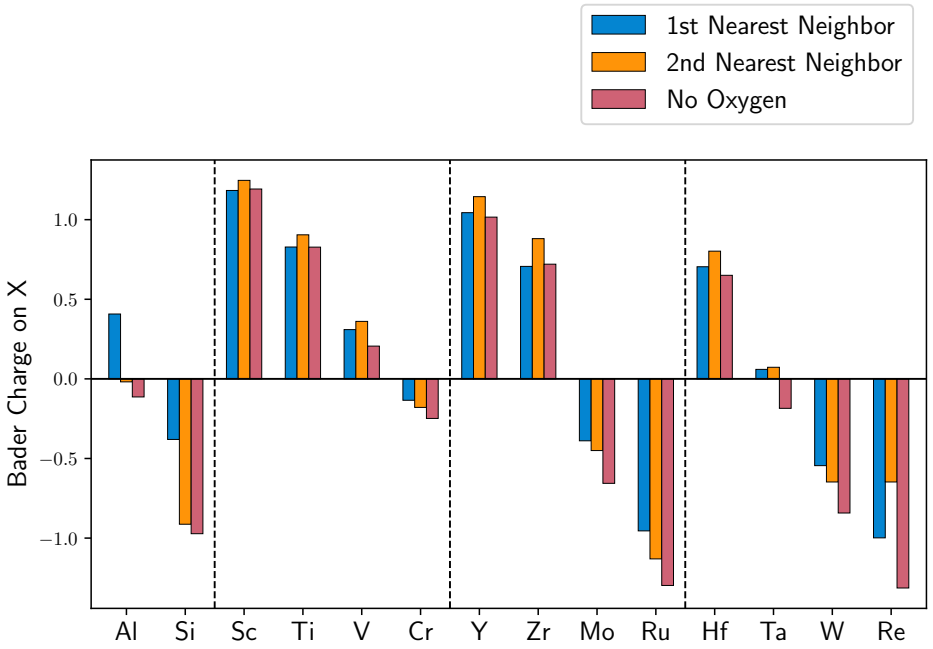

Figure C.1: The Bader charge on the substitutional atom are plotted for configurations where interstitial oxygen atoms are in the first near est neighbor site, the second nearest neighbor site, or not present. When oxygen is not present the Bader charges are more slightly more negative than the second nearest neighbor site, with the exception of Re where the difference in charge is more pronounced.

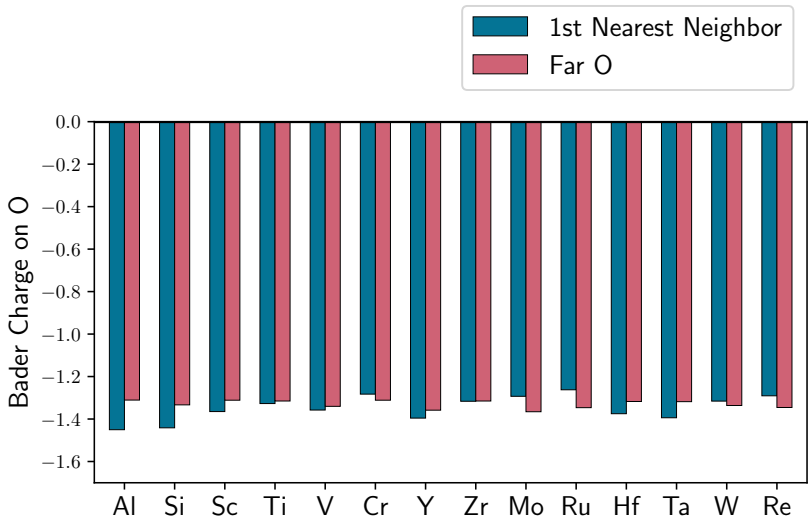

Figure C.2: The Bader charge on the interstitial oxygen is plotted for the 1st nearest neighbor site and the distance reference site. The charge for oxygen in all structures is very similar.

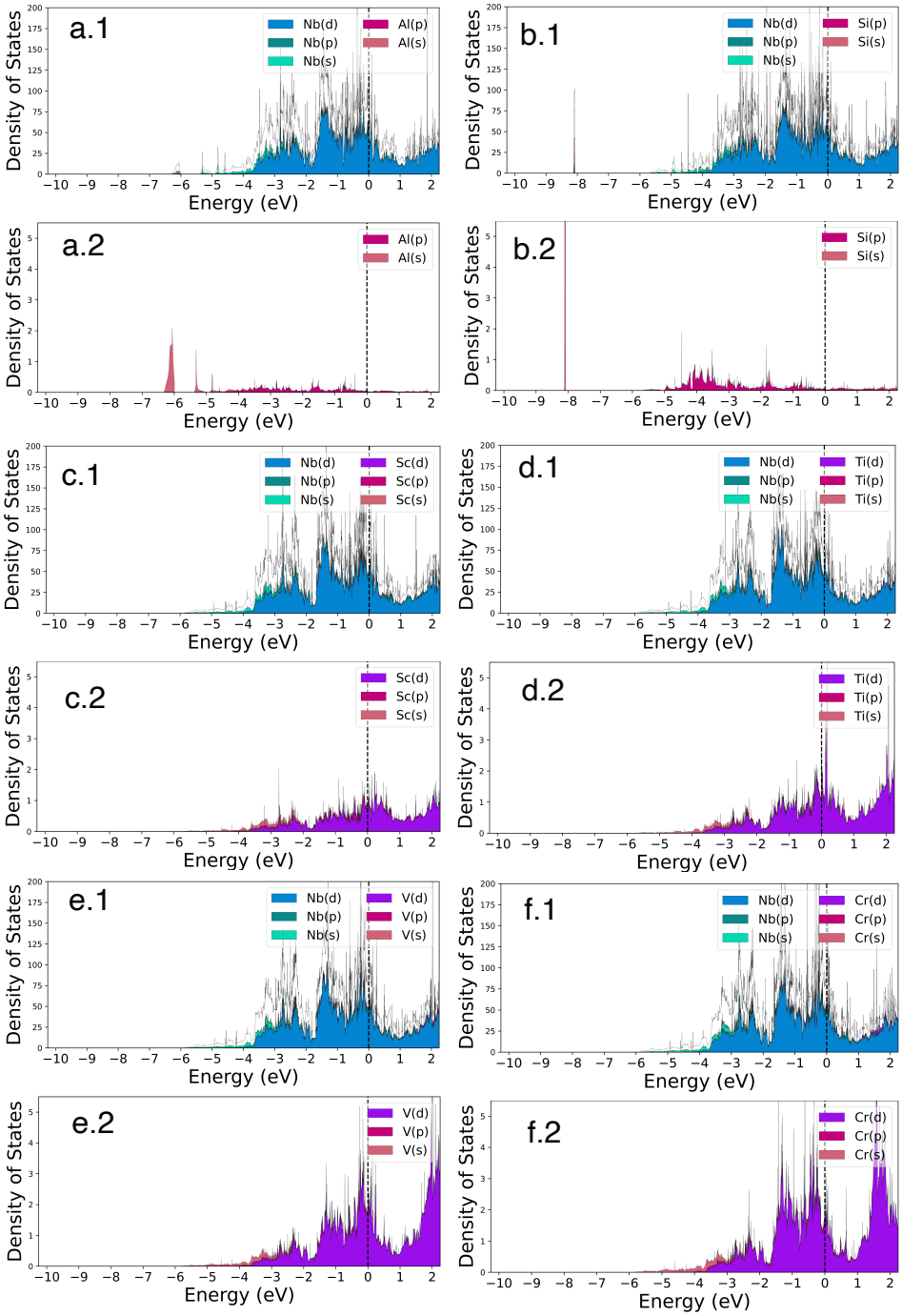

Figure C.3: The DOS for a 54 atom BCC supercell is shown with one substitutional alloying element atom and 53 Nb atoms. For each material, part 1 shows the projected DOS and total DOS as a dotted line while part 2 highlights the states projected onto the substitutional atom. Part a-f correspond to the electron structure niobium alloyed with Al, Si, Sc, Ti, Cr, and V respectively. While Si and Al both have states where are lower in energy than the band of Nb valence states and isolated, the rest of the metals have relatively similar densities of states to the Nb metal. Their d electron states mix with the niobium states and become part of the same electronic band.

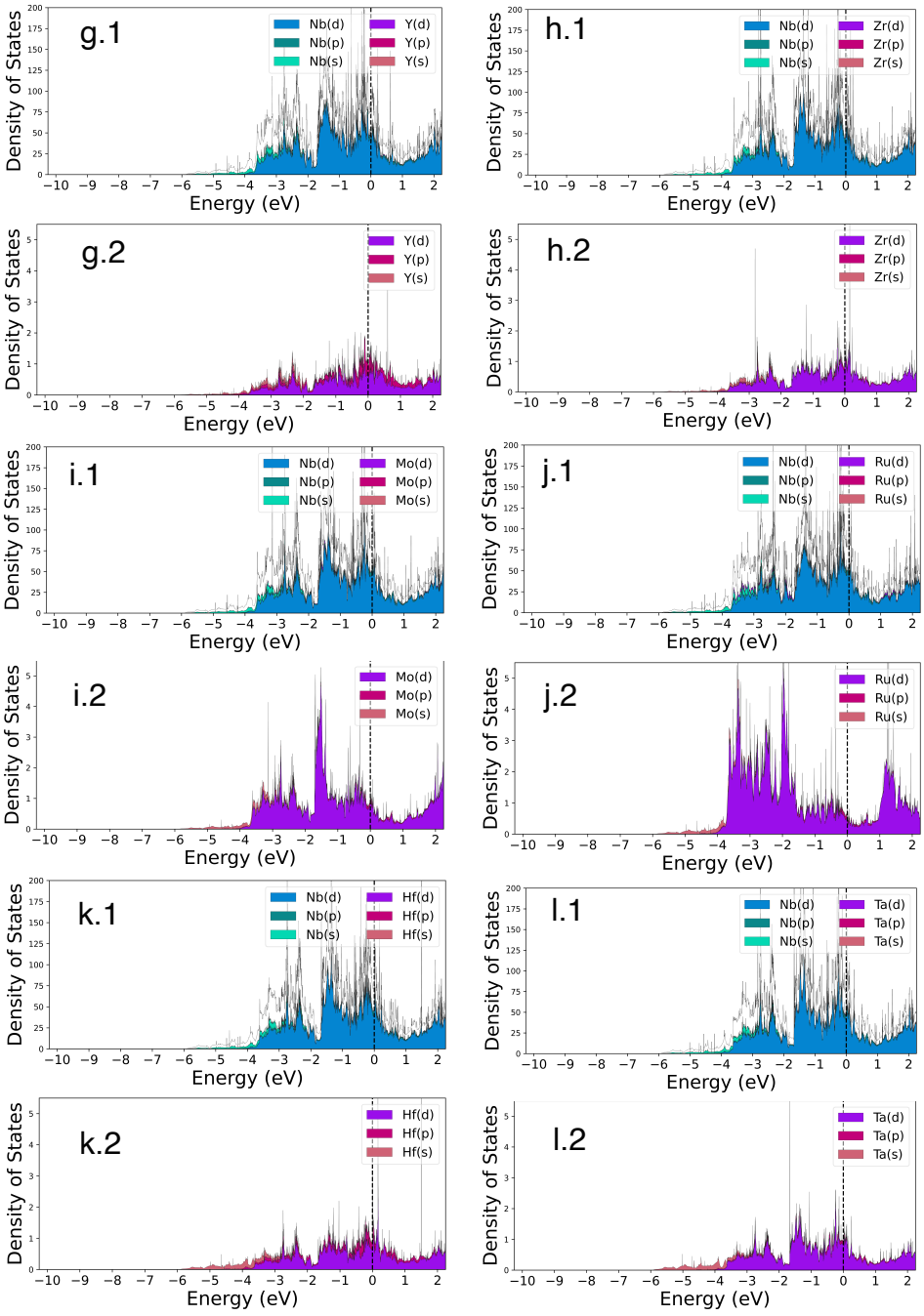

Figure C.4: The projected density of states for a 6 more dilute Nb-X alloys are shown. For each material, part 1 shows the projected DOS and total DOS as a dotted line while part 2 highlights the states projected onto the substitutional atom. Part g-l correspond to the electron structure niobium alloyed with Y, Zr, Mo, Ru, Hf, and Ta respectively. These transition metals have relatively similar densities of states to the Nb metal. Their d electron states mix and become part of the same electronic band.

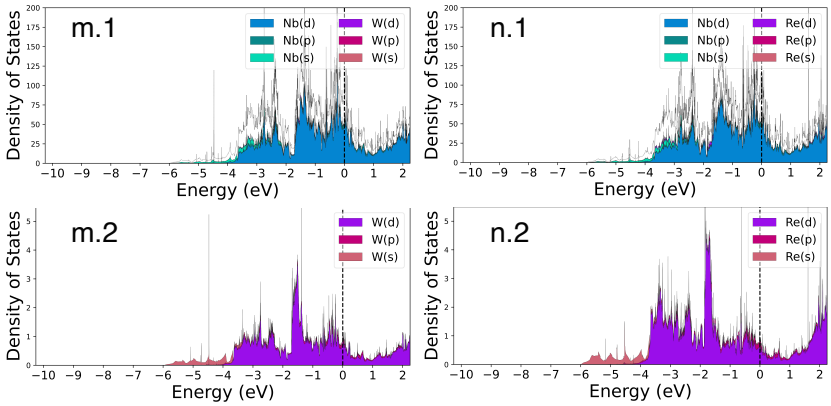

Figure C.5: The projected density of states for a 6 more dilute Nb-X alloys are shown. For each material, part 1 shows the projected DOS and total DOS as a dotted line while part 2 highlights the states projected onto the substitutional atom. Part m and n correspond to the electron structure niobium alloyed with W and Re respectively. These transition metals have relatively similar densities of states to the Nb metal. Their d electron states mix and become part of the same electronic band.

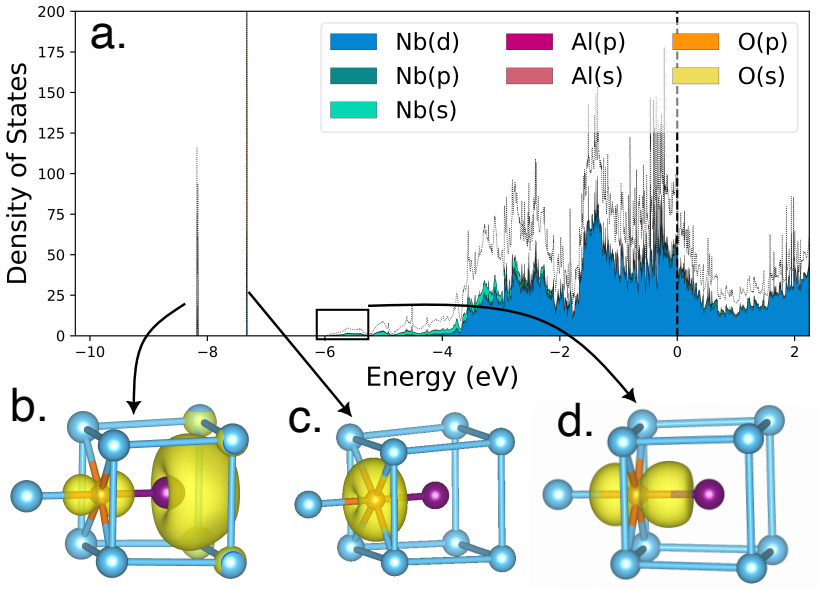

Figure C.6: The projected density of states (a) for $Nb_{53}AlO$ is shown for the first nearest neighbor configuration with the total DOS plotted with a dotted line. Below is the partial charge density for these isolated and fully occupied electronic states. There are a low energy bonding (b), a mid-energy nonbonding (c), and an high energy antibonding orbital (d) due to hybridization between the Al s orbitals and oxygen p-orbitals.

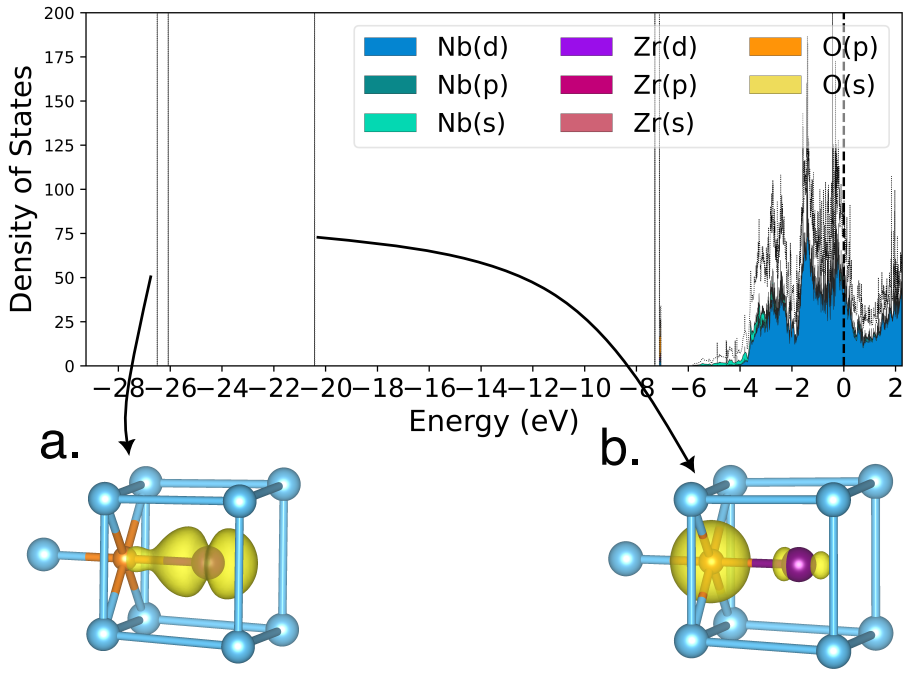

Figure C.7: The projected DOS for $Nb_{53}ZrO$ is shown for the first nearest neighbor configuration with the total DOS plotted with a dotted line. Below the partial charge density if shown for isolated and fully occupied electronic states. There is a low energy bonding (a) and higher energy antibonding orbital (b) due to hybridization between the Zr p orbitals and oxygen s-orbitals.

Bibliography

[1] J. B. Goodenough and Y. Kim, *Challenges for rechargeable Li batteries*, *Chemistry of materials* **22** (2010), no. 3 587–603.

[2] Y. Yang and J. Zhao, *Wadsley–roth crystallographic shear structure niobium-based oxides: Promising anode materials for high-safety lithium-ion batteries*, *Advanced Science* **8** (2021), no. 12 2004855.

[3] R. A. Perkins and G. H. Meier, *The oxidation behavior and protection of niobium*, *JOM* **42** (1990) 17–21.

[4] N. Philips, M. Carl, and N. Cunningham, *New opportunities in refractory alloys*, *Metallurgical and Materials Transactions A* **51** (2020) 3299–3310.

[5] J.-W. Yeh, S.-K. Chen, S.-J. Lin, J.-Y. Gan, T.-S. Chin, T.-T. Shun, C.-H. Tsau, and S.-Y. Chang, *Nanostructured high-entropy alloys with multiple principal elements: novel alloy design concepts and outcomes*, *Advanced Engineering Materials* **6** (2004), no. 5 299–303.

[6] B. Cantor, I. Chang, P. Knight, and A. Vincent, *Microstructural development in equiatomic multicomponent alloys*, *Materials Science and Engineering: A* **375** (2004) 213–218.

[7] I. Machlin, *Refractory Metal Alloys Metallurgy and Technology: Proceedings of a Symposium on Metallurgy and Technology of Refractory Metals Held in Washington, DC, April 25–26, 1968. Sponsored by the Refractory Metals Committee, Institute of Metals Division, The Metallurgical Society of AIME and the National Aeronautics and Space Administration, Washington, DC.* Springer Science & Business Media, 2012.

[8] B. Puchala and A. Van der Ven, *Thermodynamics of the Zr-O system from first-principles calculations*, *Physical review B* **88** (2013), no. 9 094108.

[9] N. H. Gunda, B. Puchala, and A. Van der Ven, *Resolving phase stability in the Ti-O binary with first-principles statistical mechanics methods*, *Physical Review Materials* **2** (2018), no. 3 033604.

[10] T. Butler, K. Chaput, J. Dietrich, and O. Senkov, *High temperature oxidation behaviors of equimolar NbTiZrV and NbTiZrCr refractory complex concentrated alloys (RCCAs)*, *Journal of Alloys and Compounds* **729** (2017) 1004–1019.

[11] J. DiStefano, B. Pint, and J. DeVan, *Oxidation of refractory metals in air and low pressure oxygen gas*, *International Journal of Refractory Metals and Hard Materials* **18** (2000), no. 4-5 237–243.

[12] R. Frank, *Recent advances in columbium alloys*, in *Refractory Metal Alloys Metallurgy and Technology: Proceedings of a Symposium on Metallurgy and Technology of Refractory Metals held in Washington, DC, April 25–26, 1968. Sponsored by the Refractory Metals Committee, Institute of Metals Division, The Metallurgical Society of AIME and the National Aeronautics and Space Administration, Washington, DC*, pp. 325–372, Springer, 1968.

[13] C. Reynolds, T. M. Pollock, and A. Van der Ven, *Prediction of Nb-O phase stability and analysis of common defects in bcc Nb and vacancy ordered rocksalt NbO*, *Physcial Review Materials* (2023). Submitted.

[14] M. Saber, C. Reynolds, T. M. Pollock, and A. Van der Ven, *Chemical and structural factors affecting the stability of Wadsley-Roth block phases*, *Inorganic Chemistry* (2023). Submitted.

[15] C. Reynolds, T. M. Pollock, and A. Van der Ven, *Solute-solute interactions in dilute Nb-X-O alloys from first principles*, *Acta Materialia* (2023). Submitted.

[16] K. Naito, N. Kamegashira, and N. Sasaki, *Phase equilibria in the system between NbO_2 and Nb_2O_5 at high temperatures*, *Journal of Solid State Chemistry* **35** (1980), no. 3 305–311.

[17] C. Nico, T. Monteiro, and M. P. Graça, *Niobium oxides and niobates physical properties: Review and prospects*, *Progress in Materials Science* **80** (2016) 1–37.

[18] H. Okamoto, T. Massalski, *et. al.*, *Binary alloy phase diagrams*, *ASM International, Materials Park, OH, USA* (1990) 12.

[19] R. Roth and L. Coughanour, *Phase equilibrium relations in the systems titania-niobia*, *Journal of Research of the National Bureau of standards* **55** (1955), no. 4 209.

[20] R. Roth and A. Wadsley, *Multiple phase formation in the binary system Nb_2O_5–WO_3. I. preparation and identification of phases*, *Acta Crystallographica* **19** (1965), no. 1 26–32.

[21] R. Roth and A. Wadsley, *Multiple phase formation in the binary system Nb_2O_5–WO_3. III. the structures of the tetragonal phases $W_3Nb_{14}O_{44}$ and $W_8Nb_{18}O_{69}$*, *Acta Crystallographica* **19** (1965), no. 1 38–42.

[22] R. Roth and A. Wadsley, *Multiple phase formation in the binary system Nb_2O_5–WO_3. II. the structure of the monoclinic phases $WNb_{12}O_{33}$ and $W_5Nb_{16}O_{55}$*, *Acta Crystallographica* **19** (1965), no. 1 32–38.

[23] R. Roth and A. Wadsley, *Multiple phase formation in the binary system Nb_2O_5–WO_3. IV. the block principle*, *Acta Crystallographica* **19** (1965), no. 1 42–47.

[24] R. Roth and A. Wadsley, *Mixed oxides of titanium and niobium: the crystal structure of $TiNb_{24}O_{62}$, (TiO_2, $12Nb_2O_5$)*, *Acta Crystallographica* **18** (1965), no. 4 724–730.

[25] X. Lou, R. Li, X. Zhu, L. Luo, Y. Chen, C. Lin, H. Li, and X. Zhao, *New anode material for lithium-ion batteries: aluminum niobate ($AlNb_11O_{29}$)*, *ACS Applied Materials & Interfaces* **11** (2019), no. 6 6089–6096.

[26] R. Zheng, S. Qian, X. Cheng, H. Yu, N. Peng, T. Liu, J. Zhang, M. Xia, H. Zhu, and J. Shu, *$FeNb_{11}O_{29}$ nanotubes: Superior electrochemical energy storage performance and operating mechanism*, *Nano Energy* **58** (2019) 399–409.

[27] X. Zhu, J. Xu, Y. Luo, Q. Fu, G. Liang, L. Luo, Y. Chen, C. Lin, and X. Zhao, *$MoNb_{12}O_{33}$ as a new anode material for high-capacity, safe, rapid and durable Li^+ storage: structural characteristics, electrochemical properties and working mechanisms*, *Journal of Materials Chemistry A* **7** (2019), no. 11 6522–6532.

[28] Y. Li, R. Zheng, H. Yu, X. Cheng, T. Liu, N. Peng, J. Zhang, M. Shui, and J. Shu, *Observation of $ZrNb_{14}O_{37}$ nanowires as a lithium container via in situ and ex situ techniques for high-performance lithium-ion batteries*, *ACS Applied Materials & Interfaces* **11** (2019), no. 25 22429–22438.

[29] R. J. Cava, D. W. Murphy, and S. Zahurak, *Lithium insertion in Wadsley-Roth phases based on niobium oxide*, *Journal of the Electrochemical Society* **130** (1983), no. 12 2345.

[30] N. Takami, K. Ise, Y. Harada, T. Iwasaki, T. Kishi, and K. Hoshina, *High-energy, fast-charging, long-life lithium-ion batteries using $TiNb_2O_7$ anodes for automotive applications*, *Journal of Power Sources* **396** (2018) 429–436.

[31] V. Eyert, *The metal-insulator transition of NbO_2: an embedded peierls instability*, *Europhysics letters* **58** (2002), no. 6 851.

[32] R. Janninck and D. Whitmore, *Electrical conductivity and thermoelectric power of niobium dioxide*, *Journal of Physics and Chemistry of Solids* **27** (1966), no. 6-7 1183–1187.

[33] C. Rao, M. Natarajan, G. S. Rao, and R. Loehman, *Phase transitions and conductivity anomalies in solid solutions of VO_2 with TiO_2, NbO_2, and MoO_2*, *Journal of Physics and Chemistry of Solids* **32** (1971), no. 6 1147–1150.

[34] A. K. Efimenko, N. Hollmann, K. Hoefer, J. Weinen, D. Takegami, K. K. Wolff, S. G. Altendorf, Z. Hu, A. D. Rata, A. C. Komarek, *et. al.*, *Electronic signature of the vacancy ordering in NbO (Nb_3O_3)*, *Physical Review B* **96** (2017), no. 19 195112.

[35] J. K. Burdett and J. F. Mitchell, *Pair potentials and the ordered defect structure of niobium monoxide*, *Inorganic Chemistry* **32** (1993), no. 23 5004–5006.

[36] J. K. Burdett and J. F. Mitchell, *Electronic origin of nonstoichiometry in early-transition-metal chalcogenides*, *Chemistry of materials* **5** (1993), no. 10 1465–1473.

[37] A. Seybolt, *Solid solubility of oxygen in columbium*, *JOM* **6** (1954) 774–776.

[38] A. Taylor and N. Doyle, *The solid-solubility of oxygen in Nb and Nb-rich Nb-Hf, Nb-Mo and Nb-W alloys: Part I: the nb-o system*, *Journal of the Less Common Metals* **13** (1967), no. 3 313–330.

[39] C. A. Wert and R. C. Frank, *Trapping of interstitials in metals*, *Annual Review of Materials Science* **13** (1983), no. 1 139–172.

[40] R. Powers and M. V. Doyle, *Diffusion of interstitial solutes in the group V transition metals*, *Journal of Applied Physics* **30** (1959), no. 4 514–524.

[41] O. Florêncio, W. Botta, C. Grandini, H. Tejima, and J. Jordão, *Anelastic behaviour in Nb Ti alloys containing interstitial elements*, *Journal of alloys and compounds* **211** (1994) 37–40.

[42] R. Bryant, *The solubility of oxygen in transition metal alloys*, *Journal of the Less common Metals* **4** (1962), no. 1 62–68.

[43] E. Fromm, *Emf measurements in niobium–oxygen and tantalum–oxygen solid solutions.*, tech. rep., Max-Planck-Institut fuer Metallforschung, Stuttgart, 1970.

[44] A. R. Massih and R. Jerlerud, *Thermodynamic evaluation of the Nb-O system*, 2006.

[45] E. Gebhardt and R. Rothenbacher, *Untersuchungen im system niob-sauerstoff: I. eigenschaftsänderungen von niob durch gelösten sauerstoff*, *International Journal of Materials Research* **54** (1963), no. 8 443–448.

[46] W. Nickerson and C. Altstetter, *A study of the niobium-oxygen solid solution utilizing solid electrolytic cells*, *Scripta Metallurgica* **7** (1973), no. 2 229–232.

[47] C. Briant, *The properties and uses of refractory metals and their alloys*, *MRS Online Proceedings Library (OPL)* **322** (1993).

[48] R. Perkins, L. Riedinger, and S. Sokolsky, *Problems in the oxidation protection of refractory metals in aerospace applications*, *ARMED SERVICES TECHNICAL INFORMATION AGENCY ARLINGTON HALL STATION ARLINGTON 12, VIRGINIA* (1962) 429.

[49] M. D. Novak and C. G. Levi, *Oxidation and volatilization of silicide coatings for refractory niobium alloys*, in *ASME International Mechanical Engineering Congress and Exposition*, vol. 42959, pp. 261–267, 2007.

[50] O. Senkov, J. Scott, S. Senkova, D. Miracle, and C. Woodward, *Microstructure and room temperature properties of a high-entropy TaNbHfZrTi alloy*, *Journal of alloys and compounds* **509** (2011), no. 20 6043–6048.

[51] Haynes International, "Haynes 230 Alloy." https://haynesintl.com/docs/default-source/pdfs/new-alloy-brochures/high-temperature-alloys/brochures/230-brochure.pdf.

[52] Special Metals, "Inconel Alloy 718." https://www.specialmetals.com/documents/technical-bulletins/inconel/inconel-alloy-718.pdf.

[53] D. B. Miracle and O. N. Senkov, *A critical review of high entropy alloys and related concepts*, *Acta Materialia* **122** (2017) 448–511.

[54] W. Ye, H. Yu, X. Cheng, H. Zhu, R. Zheng, T. Liu, N. Long, M. Shui, and J. Shu, *Highly efficient lithium container based on non-wadsley-roth structure $Nb_{18}W_{16}O_{93}$ nanowires for electrochemical energy storage*, *Electrochimica Acta* **292** (2018) 331–338.

[55] O. N. Senkov, D. B. Miracle, K. J. Chaput, and J.-P. Couzinie, *Development and exploration of refractory high entropy alloys—a review*, *Journal of materials research* **33** (2018), no. 19 3092–3128.

[56] O. Senkov, G. Wilks, D. Miracle, C. Chuang, and P. Liaw, *Refractory high-entropy alloys*, *Intermetallics* **18** (2010), no. 9 1758–1765.

[57] D. B. Miracle, M.-H. Tsai, O. N. Senkov, V. Soni, and R. Banerjee, *Refractory high entropy superalloys (RSAs)*, *Scripta Materialia* **187** (2020) 445–452.

[58] O. Kubaschewski and B. Hopkins, *Oxidation mechanisms of niobium, tantalum, molybdenum and tungsten*, *Journal of the Less Common Metals* **2** (1960), no. 2-4 172–180.

[59] O. Senkov, S. Senkova, D. Dimiduk, C. Woodward, and D. Miracle, *Oxidation behavior of a refractory $NbCrMo_{0.5}Ta_{0.5}TiZr$ alloy*, *Journal of Materials Science* **47** (2012) 6522–6534.

[60] S. Sheikh, L. Gan, X. Montero, H. Murakami, and S. Guo, *Forming protective alumina scale for ductile refractory high-entropy alloys via aluminizing*, *Intermetallics* **123** (2020) 106838.

[61] A. Taylor and N. Doyle, *The solid-solubility of oxygen in Nb and Nb-rich, Nb-Hf, Nb-Mo and Nb-W alloys: Part II: the ternary system Nb-Hf-O*, *Journal of the Less Common Metals* **13** (1967), no. 3 331–337.

[62] A. Taylor and N. Doyle, *The solid-solubility of oxygen in Nb and Nb-rich Nb-Hf, Nb-Mo and Nb-W alloys: part III: The ternary systems Nb-Mo-O and Nb-WO*, *Journal of the Less Common Metals* **13** (1967), no. 3 338–351.

[63] W. D. Klopp, D. J. Maykuth, C. T. Sims, and R. I. Jaffee, *Oxidation and contamination reactions of niobium and niobium alloys*, tech. rep., Battelle Memorial Inst., Columbus, Ohio, 1959.

[64] T. Butler, O. Senkov, T. Daboiku, M. Velez, H. Schroader, L. Ware, and M. Titus, *Oxidation behaviors of CrNb, CrNbTi, and CrNbTaTi concentrated refractory alloys*, *Intermetallics* **140** (2022) 107374.

[65] O. Senkov, J. Gild, and T. Butler, *Microstructure, mechanical properties and oxidation behavior of NbTaTi and NbTaZr refractory alloys*, *Journal of Alloys and Compounds* **862** (2021) 158003.

[66] R. Su, H. Zhang, G. Ouyang, L. Liu, D. D. Johnson, and J. H. Perepezko, *Oxidation mechanism in a refractory multiple-principal-element alloy at high temperature*, *Acta Materialia* **246** (2023) 118719.

[67] *CASM*, 2017. version: 0.2.1. https://github.com/prisms-center/CASMcode.

[68] R. M. Martin, *Electronic structure: basic theory and practical methods*. Cambridge university press, 2004.

[69] F. Giustino, *Materials modelling using density functional theory: properties and predictions*. Oxford University Press, 2014.

[70] M. Born and R. Oppenheimer, *Zur quantentheorie der molekeln annalen der physik, v. 84*, .

[71] V. Fock, *Näherungsmethode zur lösung des quantenmechanischen mehrkörperproblems*, *Zeitschrift für Physik* **61** (1930) 126–148.

[72] P. Hohenberg and W. Kohn, *Inhomogeneous electron gas*, *Physical review* **136** (1964), no. 3B B864.

[73] W. Kohn and L. J. Sham, *Self-consistent equations including exchange and correlation effects*, *Physical review* **140** (1965), no. 4A A1133.

[74] J. P. Perdew and Y. Wang, *Accurate and simple analytic representation of the electron-gas correlation energy*, *Physical review B* **45** (1992), no. 23 13244.

[75] J. P. Perdew, K. Burke, and M. Ernzerhof, *Generalized gradient approximation made simple*, *Physical review letters* **77** (1996), no. 18 3865.

[76] G. Kresse and J. Hafner, *Ab initio molecular dynamics for liquid metals*, *Physical Review B* **47** (1993), no. 1 558.

[77] G. Kresse and J. Hafner, *Ab initio molecular-dynamics simulation of the liquid-metal–amorphous-semiconductor transition in germanium*, *Physical Review B* **49** (1994), no. 20 14251.

[78] P. E. Blöchl, *Projector augmented-wave method*, *Physical review B* **50** (1994), no. 24 17953.

[79] G. Kresse and D. Joubert, *From ultrasoft pseudopotentials to the projector augmented-wave method*, *Physical review b* **59** (1999), no. 3 1758.

[80] J. M. Sanchez, F. Ducastelle, and D. Gratias, *Generalized cluster description of multicomponent systems*, *Physica A: Statistical Mechanics and its Applications* **128** (1984), no. 1-2 334–350.

[81] A. Van der Ven, J. C. Thomas, B. Puchala, and A. R. Natarajan, *First-principles statistical mechanics of multicomponent crystals*, *Annual Review of Materials Research* **48** (2018) 27–55.

[82] J. Sanchez, *Cluster expansion and the configurational theory of alloys*, *Physical Review B* **81** (2010), no. 22 224202.

[83] C. Kittel and H. Kroemer, *Thermal physics*, vol. 9690. Wiley New York, 1969.

[84] B. Puchala and A. Van der Ven, *Monte carlo calculations of the thermodynamic and kinetic properties of complex multicomponent crystals*, . In Preparation.

[85] B. Puchala, J. C. Thomas, A. R. Natarajan, J. G. Goiri, S. S. Behara, J. L. Kaufman, and A. Van der Ven, *CASM—a software package for first-principles based study of multicomponent crystalline solids*, *Computational Materials Science* **217** (2023) 111897.

[86] G. L. Hart and R. W. Forcade, *Algorithm for generating derivative structures*, *Physical Review B* **77** (2008), no. 22 224115.

[87] S. Rao, B. Akdim, E. Antillon, C. Woodward, T. Parthasarathy, and O. Senkov, *Modeling solution hardening in bcc refractory complex concentrated alloys: NbTiZr, $Nb_{1.5}TiZr_{0.5}$ and $Nb_{0.5}TiZr_{1.5}$*, *Acta Materialia* **168** (2019) 222–236.

[88] C. Zhang, B. E. MacDonald, F. Guo, H. Wang, C. Zhu, X. Liu, Y. Kang, X. Xie, Y. Zhou, K. S. Vecchio, *et. al.*, *Cold-workable refractory complex concentrated alloys with tunable microstructure and good room-temperature tensile behavior*, *Scripta Materialia* **188** (2020) 16–20.

[89] J. Wadsworth, T. Nieh, and J. Stephens, *Recent advances in aerospace refractory metal alloys*, *International materials reviews* **33** (1988), no. 1 131–150.

[90] R. Begley, D. Harrod, and R. Gold, *High temperature creep and fracture behavior of the refractory metals*, in *Refractory metal alloys metallurgy and technology*, pp. 41–83. Springer, 1968.

[91] R. Cava, B. Batlogg, J. Krajewski, H. Poulsen, P. Gammel, W. Peck Jr, and L. Rupp Jr, *Electrical and magnetic properties of N_2O_5- δ crystallographic shear structures*, *Physical Review B* **44** (1991), no. 13 6973.

[92] C. P. Koçer, K. J. Griffith, C. P. Grey, and A. J. Morris, *First-principles study of localized and delocalized electronic states in crystallographic shear phases of niobium oxide*, *Physical Review B* **99** (2019), no. 7 075151.

[93] K. J. Griffith, K. M. Wiaderek, G. Cibin, L. E. Marbella, and C. P. Grey, *Niobium tungsten oxides for high-rate lithium-ion energy storage*, *Nature* **559** (2018), no. 7715 556–563.

[94] M. B. Preefer, M. Saber, Q. Wei, N. H. Bashian, J. D. Bocarsly, W. Zhang, G. Lee, J. Milam-Guerrero, E. S. Howard, R. C. Vincent, *et. al.*, *Multielectron redox and insulator-to-metal transition upon lithium insertion in the fast-charging, Wadsley-Roth phase PNb_9O_{25}*, *Chemistry of Materials* **32** (2020), no. 11 4553–4563.

[95] M. Saber, M. B. Preefer, S. K. Kolli, W. Zhang, G. Laurita, B. Dunn, R. Seshadri, and A. Van der Ven, *Role of electronic structure in Li ordering and chemical strain in the fast charging wadsley–roth phase PNb_9O_{25}*, *Chemistry of Materials* **33** (2021), no. 19 7755–7766.

[96] A. G. Olabi, Q. Abbas, P. A. Shinde, and M. A. Abdelkareem, *Rechargeable batteries: Technological advancement, challenges, current and emerging applications*, *Energy* (2022) 126408.

[97] L. Ma, T. Yu, E. Tzoganakis, K. Amine, T. Wu, Z. Chen, and J. Lu, *Fundamental understanding and material challenges in rechargeable nonaqueous Li–O_2 batteries: recent progress and perspective*, *Advanced Energy Materials* **8** (2018), no. 22 1800348.

[98] Y. Sun, N. Liu, and Y. Cui, *Promises and challenges of nanomaterials for lithium-based rechargeable batteries*, *Nature Energy* **1** (2016), no. 7 1–12.

[99] T. Mueller and G. Ceder, *Bayesian approach to cluster expansions*, *Physical Review B* **80** (2009), no. 2 024103.

[100] J. Kristensen and N. J. Zabaras, *Bayesian uncertainty quantification in the evaluation of alloy properties with the cluster expansion method*, *Computer Physics Communications* **185** (2014), no. 11 2885–2892.

[101] M. Aldegunde, N. Zabaras, and J. Kristensen, *Quantifying uncertainties in first-principles alloy thermodynamics using cluster expansions*, *Journal of Computational Physics* **323** (2016) 17–44.

[102] W. Tang, E. Sanville, and G. Henkelman, *A grid-based Bader analysis algorithm without lattice bias*, *Journal of Physics: Condensed Matter* **21** (2009), no. 8 084204.

[103] E. Sanville, S. D. Kenny, R. Smith, and G. Henkelman, *Improved grid-based algorithm for Bader charge allocation*, *Journal of computational chemistry* **28** (2007), no. 5 899–908.

[104] G. Henkelman, A. Arnaldsson, and H. Jónsson, *A fast and robust algorithm for Bader decomposition of charge density*, *Computational Materials Science* **36** (2006), no. 3 354–360.

[105] M. Yu and D. R. Trinkle, *Accurate and efficient algorithm for Bader charge integration*, *The Journal of chemical physics* **134** (2011), no. 6 064111.

[106] R. Dronskowski and P. E. Blöchl, *Crystal orbital hamilton populations (COHP): energy-resolved visualization of chemical bonding in solids based on density-functional calculations*, *The Journal of Physical Chemistry* **97** (1993), no. 33 8617–8624.

[107] V. L. Deringer, A. L. Tchougréeff, and R. Dronskowski, *Crystal orbital hamilton population (COHP) analysis as projected from plane-wave basis sets*, *The journal of physical chemistry A* **115** (2011), no. 21 5461–5466.

[108] S. Maintz, V. L. Deringer, A. L. Tchougréeff, and R. Dronskowski, *Analytic projection from plane-wave and PAW wavefunctions and application to chemical-bonding analysis in solids*, *Journal of computational chemistry* **34** (2013), no. 29 2557–2567.

[109] S. Maintz, V. L. Deringer, A. L. Tchougréeff, and R. Dronskowski, *LOBSTER: A tool to extract chemical bonding from plane-wave based DFT*, 2016.

[110] M. E. Tipping, *Sparse bayesian learning and the relevance vector machine*, *Journal of machine learning research* **1** (2001), no. Jun 211–244.

[111] D. J. MacKay, *Bayesian interpolation*, *Neural computation* **4** (1992), no. 3 415–447.

[112] D. Zagorac, H. Müller, S. Ruehl, J. Zagorac, and S. Rehme, *Recent developments in the inorganic crystal structure database: theoretical crystal structure data and related features*, *Journal of applied crystallography* **52** (2019), no. 5 918–925.

[113] M. Blanter, V. Dmitriev, and A. V. Ruban, *Interstitial–interstitial interactions in bcc VB group metals: Ab initiocalculations*, *Journal of Physics and Chemistry of Solids* **74** (2013), no. 5 716–722.

[114] M. Blanter, V. Dmitriev, B. Mogutnov, and A. V. Ruban, *Interaction of interstitial atoms and configurational contribution to their thermodynamic activity in V, Nb, and Ta*, *Physics of Metals and Metallography* **118** (2017), no. 2 105–112.

[115] N. H. Gunda and A. Van der Ven, *Understanding the interactions between interstitial and substitutional solutes in refractory alloys: The case of Ti-Al-O*, *Acta Materialia* **191** (2020) 149–157.

[116] N. H. Gunda, C. G. Levi, and A. Van der Ven, "Factors that affect interactions between substitutional solutes and interstitial oxygen in Ti." unpublished.

[117] J. M. Cowley, *X-ray measurement of order in single crystals of Cu_3Au*, *Journal of Applied Physics* **21** (1950), no. 1 24–30.

[118] J. K. Burdett and T. Hughbanks, *Niobium oxide (NbO) and titanium oxide (TiO): a study of the structural and electronic stability of structures derived from rock salt*, *Journal of the American Chemical Society* **106** (1984), no. 11 3101–3113.

[119] A. Miura, T. Takei, N. Kumada, S. Wada, E. Magome, C. Moriyoshi, and Y. Kuroiwa, *Bonding preference of carbon, nitrogen, and oxygen in niobium-based rock-salt structures*, *Inorganic Chemistry* **52** (2013), no. 17 9699–9701.

[120] S. Maintz, M. Esser, and R. Dronskowski, *Efficient rotation of local basis functions using real spherical harmonics.*, *Acta Physica Polonica B* **47** (2016), no. 4.

[121] M. Asta and V. Ozoliņš, *Structural, vibrational, and thermodynamic properties of Al-Sc alloys and intermetallic compounds*, *Physical Review B* **64** (2001), no. 9 094104.

[122] C. Wolverton, V. Ozoliņš, and M. Asta, *Hydrogen in aluminum: First-principles calculations of structure and thermodynamics*, *Physical Review B* **69** (2004), no. 14 144109.

[123] M. Asta, V. Ozolins, and C. Woodward, *A first-principles approach to modeling alloy phase equilibria*, *JOM* **53** (2001) 16–19.

[124] B. Gorr, S. Schellert, F. Müller, H.-J. Christ, A. Kauffmann, and M. Heilmaier, *Current status of research on the oxidation behavior of refractory high entropy alloys*, *Advanced Engineering Materials* **23** (2021), no. 5 2001047.

[125] R. Elliott, *Columbium-oxygen system*, *Trans. Am. Soc. Metals* **52** (1960).

[126] R. J. Pérez and A. Massih, *Thermodynamic evaluation of the Nb–O–Zr system*, *Journal of nuclear materials* **360** (2007), no. 3 242–254.

[127] J. Gebauer, P. Franke, and H. J. Seifert, *Thermodynamic evaluation of the system Ta–O and Preliminary Assessment of the Systems Al–Nb–O and Al–Ta–O*, *Advanced Engineering Materials* **24** (2022), no. 8 2200162.

[128] N. Dupin, I. Ansara, C. Servant, C. Toffolon, C. Lemaignan, and J. Brachet, *A thermodynamic database for zirconium alloys*, *Journal of nuclear materials* **275** (1999), no. 3 287–295.

[129] N. Dupin and I. Ansara, *Unpublished communication regarding the nb-o system.*, 2001.

[130] A. R. Natarajan, P. Dolin, and A. Van der Ven, *Crystallography, thermodynamics and phase transitions in refractory binary alloys*, *Acta Materialia* **200** (2020) 171–186.

[131] R. Cava, D. Murphy, E. Rietman, S. Zahurak, and H. Barz, *Lithium insertion, electrical conductivity, and chemical substitution in various crystallographic shear structures*, *Solid State Ionics* **9** (1983) 407–411.

[132] R. Cava, D. Murphy, and S. Zahurak, *Secondary lithium cells employing vanadium tungsten oxide positive electrodes*, *Journal of The Electrochemical Society* **130** (1983), no. 1 243.

[133] R. Cava, D. Kleinman, and S. Zahurak, *$V_{3.2}W_{1.8}O_{13}$ and studies of the V_2O_5-WO_3- VO_2 ternary system*, *Materials research bulletin* **18** (1983), no. 7 869–873.

[134] S. Patoux, M. Dolle, G. Rousse, and C. Masquelier, *A reversible lithium intercalation process in an ReO_3 type structure PNb_9O_{25}*, *Journal of The Electrochemical Society* **149** (2002), no. 4 A391.

[135] J.-T. Han, Y.-H. Huang, and J. B. Goodenough, *New anode framework for rechargeable lithium batteries*, *Chemistry of Materials* **23** (2011), no. 8 2027–2029.

[136] J.-T. Han and J. B. Goodenough, *3-V full cell performance of anode framework $TiNb_2O_7$/spinel $LiNi_{0.5}Mn_{1.5}O_4$*, *Chemistry of materials* **23** (2011), no. 15 3404–3407.

[137] V. Augustyn, J. Come, M. A. Lowe, J. W. Kim, P.-L. Taberna, S. H. Tolbert, H. D. Abruña, P. Simon, and B. Dunn, *High-rate electrochemical energy storage through Li^+ intercalation pseudocapacitance*, *Nature materials* **12** (2013), no. 6 518–522.

[138] K. J. Griffith, I. D. Seymour, M. A. Hope, M. M. Butala, L. K. Lamontagne, M. B. Preefer, C. P. Kocer, G. Henkelman, A. J. Morris, M. J. Cliffe, *et. al.*, *Ionic and electronic conduction in $TiNb_2O_7$*, *Journal of the American Chemical Society* **141** (2019), no. 42 16706–16725.

[139] K. J. Griffith, Y. Harada, S. Egusa, R. M. Ribas, R. S. Monteiro, R. B. Von Dreele, A. K. Cheetham, R. J. Cava, C. P. Grey, and J. B. Goodenough, *Titanium niobium oxide: from discovery to application in fast-charging lithium-ion batteries*, *Chemistry of Materials* **33** (2020), no. 1 4–18.

[140] K. J. Griffith and C. P. Grey, *Superionic lithium intercalation through 2× 2 nm^2 columns in the crystallographic shear phase $nb_{18}w_8o_{69}$*, *Chemistry of Materials* **32** (2020), no. 9 3860–3868.

[141] Y. Liu, P. A. Russo, L. A. Montoro, and N. Pinna, *Recent developments in Nb-based oxides with crystallographic shear structures as anode materials for high-rate lithium-ion energy storage*, *Battery Energy* (2023) 0220037.

[142] F. Xie, J. Xu, Q. Liao, Q. Zhang, B. Liu, L. Shao, J. Cai, X. Shi, Z. Sun, and C.-P. Wong, *Progress in niobium-based oxides as anode for fast-charging Li-ion batteries*, *Energy Reviews* (2023) 100027.

[143] Y. Li, C. Sun, and J. B. Goodenough, *Electrochemical lithium intercalation in monoclinic $Nb_{12}O_{29}$*, *Chemistry of Materials* **23** (2011), no. 9 2292–2294.

[144] R. Li, Y. Qin, X. Liu, L. Yang, C. Lin, R. Xia, S. Lin, Y. Chen, and J. Li, *Conductive $Nb_{25}O_{62}$ and $Nb_{12}O_{29}$ anode materials for use in high-performance lithium-ion storage*, *Electrochimica Acta* **266** (2018) 202–211.

[145] J. Anderson, J. Browne, and J. Hutchison, *Electron microscopy of the niobium oxides. I. twinning and defects in H- Nb_2O_5*, *Journal of Solid State Chemistry* **5** (1972), no. 3 419–431.

[146] C. Choi, D. S. Ashby, D. M. Butts, R. H. DeBlock, Q. Wei, J. Lau, and B. Dunn, *Achieving high energy density and high power density with pseudocapacitive materials*, *Nature Reviews Materials* **5** (2020), no. 1 5–19.

[147] K. McColl, K. J. Griffith, R. L. Dally, R. Li, J. E. Douglas, K. R. Poeppelmeier, F. Corà, I. Levin, and M. M. Butala, *Energy storage mechanisms in vacancy-ordered wadsley–roth layered niobates*, *Journal of Materials Chemistry A* **9** (2021), no. 35 20006–20023.

[148] K. J. Griffith, A. C. Forse, J. M. Griffin, and C. P. Grey, *High-rate intercalation without nanostructuring in metastable Nb_2O_5 bronze phases*, *Journal of the American Chemical Society* **138** (2016), no. 28 8888–8899.

[149] A. Wadsley, *Mixed oxides of titanium and niobium. I.*, *Acta Crystallographica* **14** (1961), no. 6 660–664.

[150] V. Plies and R. Gruehn, *Zum thermischen verhalten von R-Nb_2O_5 und strukturverwandtem V_3MoO_{10} und $V_5W_3O_{20}$,* Journal of the Less Common Metals **42** *(1975), no. 1 77–88.*

[151] R. Roth, A. Wadsley, and S. Andersson, The crystal structure of PNb_9O_{25} (P_2O_5. $9Nb_2O_5$), Acta Crystallographica **18** *(1965), no. 4 643–647.*

[152] K. E. Wyckoff, D. D. Robertson, M. B. Preefer, S. M. Teicher, J. Bienz, L. Kautzsch, T. E. Mates, J. A. Cooley, S. H. Tolbert, and R. Seshadri, High-capacity Li^+ storage through multielectron redox in the fast-charging Wadsley–Roth phase $(W_{0.2}V_{0.8})_3O_7$, Chemistry of Materials **32** *(2020), no. 21 9415–9424.*

[153] J. Allpress and R. Roth, The effect of annealing on the concentration of wadsley defects in the Nb_2O_5- WO_3 system, Journal of Solid State Chemistry **3** *(1971), no. 2 209–216.*

[154] J. Allpress and A. Wadsley, Multiple phase formation in the binary system Nb_2O_5- WO_3: VII. intergrowth of H- Nb_2O_5 and $WNb_{12}O_{33}$, Journal of Solid State Chemistry **1** *(1969), no. 1 28–38.*

[155] B. Gatehouse and A. Wadsley, The crystal structure of the high temperature form of niobium pentoxide, Acta Crystallographica **17** *(1964), no. 12 1545–1554.*

[156] Z. Chen, V. Augustyn, J. Wen, Y. Zhang, M. Shen, B. Dunn, and Y. Lu, High-performance supercapacitors based on intertwined CNT/V_2O_5 nanowire nanocomposites, Advanced materials **23** *(2011), no. 6 791–795.*

[157] S. Fleischmann, J. B. Mitchell, R. Wang, C. Zhan, D.-e. Jiang, V. Presser, and V. Augustyn, Pseudocapacitance: from fundamental understanding to high power energy storage materials, Chemical Reviews **120** *(2020), no. 14 6738–6782.*

[158] *Y. Kim, Q. Jacquet, K. J. Griffith, J. Lee, S. Dey, B. L. Rinkel, and C. P. Grey, High rate lithium ion battery with niobium tungsten oxide anode,* Journal of The Electrochemical Society **168** *(2021), no. 1 010525.*

[159] *K. Ise, S. Morimoto, Y. Harada, and N. Takami, Large lithium storage in highly crystalline $TiNb_2O_7$ nanoparticles synthesized by a hydrothermal method as anodes for lithium-ion batteries,* Solid State Ionics **320** *(2018) 7–15.*

[160] *K. J. Griffith, A. Senyshyn, and C. P. Grey, Structural stability from crystallographic shear in TiO_2–Nb_2O_5 phases: Cation ordering and lithiation behavior of $tinb_{24}o_{62}$,* Inorganic chemistry **56** *(2017), no. 7 4002–4010.*

[161] *X. Wu, J. Miao, W. Han, Y.-S. Hu, D. Chen, J.-S. Lee, J. Kim, and L. Chen, Investigation on $Ti_2Nb_{10}O_{29}$ anode material for lithium-ion batteries,* Electrochemistry communications **25** *(2012) 39–42.*

[162] *A. G. Evans, D. Mumm, J. Hutchinson, G. Meier, and F. Pettit, Mechanisms controlling the durability of thermal barrier coatings,* Progress in materials science **46** *(2001), no. 5 505–553.*

[163] *D. Clarke and C. Levi, Materials design for the next generation thermal barrier coatings,* Annual review of materials research **33** *(2003), no. 1 383–417.*

[164] *C. G. Levi, Emerging materials and processes for thermal barrier systems,* Current Opinion in Solid State and Materials Science **8** *(2004), no. 1 77–91.*

[165] *B. Tryon, F. Cao, K. Murphy, C. Levi, and T. Pollock, Ruthenium-containing bond coats for thermal barrier coating systems,* JOM **58** *(2006) 53–59.*

[166] *A. G. Evans, D. R. Clarke, and C. G. Levi, The influence of oxides on the performance of advanced gas turbines,* Journal of the European Ceramic Society **28** *(2008), no. 7 1405–1419.*

[167] *C. A. Stewart, S. P. Murray, A. Suzuki, T. M. Pollock, and C. G. Levi, Accelerated discovery of oxidation resistant CoNi-base γ/γ'alloys with high $L1_2$ solvus and low density,* Materials & Design **189** *(2020) 108445.*

[168] *G. Kresse and J. Furthmüller, Efficient iterative schemes for ab initio total-energy calculations using a plane-wave basis set,* Physical review B **54** *(1996), no. 16 11169.*

[169] *G. Kresse and J. Furthmüller, Efficiency of ab-initio total energy calculations for metals and semiconductors using a plane-wave basis set,* Computational materials science **6** *(1996), no. 1 15–50.*

[170] *Q. Fu, H. Cao, G. Liang, L. Luo, Y. Chen, V. Murugadoss, S. Wu, T. Ding, C. Lin, and Z. Guo, A highly Li^+-conductive $HfNb_{24}O_{62}$ anode material for superior Li^+ storage,* Chemical Communications **56** *(2020), no. 4 619–622.*

[171] *F. Ran, X. Cheng, H. Yu, R. Zheng, T. Liu, X. Li, N. Ren, M. Shui, and J. Shu, Nano-structured $GeNb_{18}O_{47}$ as novel anode host with superior lithium storage performance,* Electrochimica Acta **282** *(2018) 634–641.*

[172] *W. Mertin, S. Andersson, and R. Gruehn, Über die kristallstruktur von M-Nb_2O_5,* Journal of Solid State Chemistry **1** *(1970), no. 3-4 419–424.*

[173] *T. McQueen, Q. Xu, E. Andersen, H. Zandbergen, and R. Cava, Structures of the reduced niobium oxides $Nb_{12}O_{29}$ and $Nb_{22}O_{54}$,* Journal of Solid State Chemistry **180** *(2007), no. 10 2864–2870.*

[174] *D. P. Opra, S. V. Gnedenkov, and S. L. Sinebryukhov, Recent efforts in design of TiO_2 (B) anodes for high-rate lithium-ion batteries: A review,* Journal of Power Sources **442** *(2019) 227225.*

[175] *A. R. Armstrong, G. Armstrong, J. Canales, R. García, and P. G. Bruce, Lithium-ion intercalation into TiO_2-B nanowires,* Advanced Materials **17** *(2005), no. 7 862–865.*

[176] *Y. Ren, Z. Liu, F. Pourpoint, A. R. Armstrong, C. P. Grey, and P. G. Bruce, Nanoparticulate TiO_2 (B): an anode for lithium-ion batteries,* Angewandte Chemie **124** *(2012), no. 9 2206–2209.*

[177] *V. Etacheri, Y. Kuo, A. Van der Ven, and B. M. Bartlett, Mesoporous TiO_2–B microflowers composed of (1 1 - 0) facet-exposed nanosheets for fast reversible lithium-ion storage,* Journal of Materials Chemistry A **1** *(2013), no. 39 12028–12032.*

[178] *S. Qian, H. Yu, L. Yan, H. Zhu, X. Cheng, Y. Xie, N. Long, M. Shui, and J. Shu, High-rate long-life pored nanoribbon VNb_9O_{25} built by interconnected ultrafine nanoparticles as anode for lithium-ion batteries,* ACS applied materials & interfaces **9** *(2017), no. 36 30608–30616.*

[179] *D. Saritha, V. Pralong, U. Varadaraju, and B. Raveau, Electrochemical Li insertion studies on $WNb_{12}O_{33}$—a shear ReO_3 type structure,* Journal of Solid State Chemistry **183** *(2010), no. 5 988–993.*

[180] *Y. Yang, H. Zhu, J. Xiao, H. Geng, Y. Zhang, J. Zhao, G. Li, X.-L. Wang, C. C. Li, and Q. Liu, Achieving ultrahigh-rate and high-safety Li^+ storage based on interconnected tunnel structure in micro-size niobium tungsten oxides,* Advanced Materials **32** *(2020), no. 12 1905295.*

[181] *C. P. Koçer, K. J. Griffith, C. P. Grey, and A. J. Morris, Lithium diffusion in niobium tungsten oxide shear structures,* Chemistry of Materials **32** *(2020), no. 9 3980–3989.*

[182] *P. Kierkegaard and M. Westerlund, The crystal structure of $MoOPO_4$,* Acta. Chem. Scand **18** *(1964) 2217–2225.*

[183] *T. Amos, A. Yokochi, and A. Sleight, Phase transition and negative thermal expansion in tetragonal $NbOPO_4$,* Journal of Solid State Chemistry **141** *(1998), no. 1 303.*

[184] *J. M. Longo and P. Kierkegaard, The crystal structure of $nbopo_4$,* Acta Chem. Scand **20** *(1966) 72–78.*

[185] *J. Longo, J. Pierce, and J. Kafalas, The tetragonal high-pressure form of $TaOPO_4$,* Materials Research Bulletin **6** *(1971), no. 11 1157–1165.*

[186] *S. W. Baek, M. B. Preefer, M. Saber, K. Zhai, M. Frajnkovič, Y. Zhou, B. S. Dunn, A. Van der Ven, R. Seshadri, and L. Pilon, Potentiometric entropy and operando calorimetric measurements reveal fast charging mechanisms in PNb_9O_{25},* Journal of Power Sources **520** *(2022) 230776.*

[187] *C. P. Koçer, K. J. Griffith, C. P. Grey, and A. J. Morris, Cation disorder and lithium insertion mechanism of wadsley–roth crystallographic shear phases from first principles,* Journal of the American Chemical Society **141** *(2019), no. 38 15121–15134.*

[188] *R. Roth and J. Waring, Phase equilibria as related to crystal structure in the system niobium pentoxide-tungsten trioxide,* Journal of Research of the National Bureau of Standards. Section A, Physics and Chemistry **70** *(1966), no. 4 281.*

[189] *Z. Lv, H. Zhu, W. Meng, L. Wei, Y. Yang, Y. Zhang, M. Ye, and C. C. Li, Cation mixing in wadsley-roth phase anode of lithium-ion battery improves cycling stability and fast Li^+ storage,* Applied Physics Reviews **8** *(2021), no. 3 031404.*

[190] *A. A. Voskanyan, M. Abramchuk, and A. Navrotsky, Entropy stabilization of TiO_2–Nb_2O_5 wadsley–roth shear phases and their prospects for lithium-ion battery anode materials,* Chemistry of Materials **32** *(2020), no. 12 5301–5308.*

[191] *C. Yang, S. Deng, C. Lin, S. Lin, Y. Chen, J. Li, and H. Wu, Porous $TiNb_{24}O_{62}$ microspheres as high-performance anode materials for lithium-ion batteries of electric vehicles,* Nanoscale **8** *(2016), no. 44 18792–18799.*

[192] *C. Yang, S. Yu, Y. Ma, C. Lin, Z. Xu, H. Zhao, S. Wu, P. Zheng, Z.-Z. Zhu, J. Li,* et. al., *Cr^{3+} and Nb^{5+} co-doped $Ti_2Nb_{10}O_{29}$ materials for high-performance lithium-ion storage,* Journal of Power Sources **360** *(2017) 470–479.*

[193] *X. Zhu, Q. Fu, L. Tang, C. Lin, J. Xu, G. Liang, R. Li, L. Luo, and Y. Chen, $Mg_2Nb_{34}O_{87}$ porous microspheres for use in high-energy, safe, fast-charging, and stable lithium-ion batteries,* ACS applied materials & interfaces **10** *(2018), no. 28 23711–23720.*

[194] *Q. Fu, X. Liu, J. Hou, Y. Pu, C. Lin, L. Yang, X. Zhu, L. Hu, S. Lin, L. Luo,* et. al.*, Highly conductive $CrNb_{11}O_{29}$ nanorods for use in high-energy, safe, fast-charging and stable lithium-ion batteries,* Journal of Power Sources **397** *(2018) 231–239.*

[195] *C. Lin, S. Yu, S. Wu, S. Lin, Z.-Z. Zhu, J. Li, and L. Lu, $Ru_{0.01}Ti_{0.99}Nb_2O_7$ as an intercalation-type anode material with a large capacity and high rate performance for lithium-ion batteries,* Journal of Materials Chemistry A **3** *(2015), no. 16 8627–8635.*

[196] *A. L. Viet, M. Reddy, R. Jose, B. Chowdari, and S. Ramakrishna, Nanostructured Nb_2O_5 polymorphs by electrospinning for rechargeable lithium batteries,* The Journal of Physical Chemistry C **114** *(2010), no. 1 664–671.*

[197] *C. Lin, G. Wang, S. Lin, J. Li, and L. Lu, $Tinb_6o_{17}$: a new electrode material for lithium-ion batteries,* Chemical Communications **51** *(2015), no. 43 8970–8973.*

[198] *R. Tao, T. Zhang, S. Tan, C. J. Jafta, C. Li, J. Liang, X.-G. Sun, T. Wang, J. Fan, Z. Lu,* et. al.*, Insight into the fast-rechargeability of a novel $Mo_{1.5}W_{1.5}Nb_{14}O_{44}$ anode material for high-performance lithium-ion batteries,* Advanced Energy Materials **12** *(2022), no. 36 2200519.*

[199] *R. Begley and J. Bechtold, Effect of alloying on the mechanical properties of niobium,* Journal of the Less Common Metals **3** *(1961), no. 1 1–12.*

[200] *C. Calhoun, Ductile-to-brittle transition of niobium-vanadium alloys as affected by notches, strain rate, nitrogen, and oxygen, tech. rep., Knolls Atomic Power Lab., Schenectady, NY, 1965.*

[201] *K. Chou, P.-W. Chu, C. G. Levi, and E. A. Marquis, Influence of a silicon-bearing film on the early stage oxidation of pure titanium,* Journal of Materials Science **52** *(2017), no. 16 9884–9894.*

[202] *K. Chou, P.-W. Chu, and E. A. Marquis, Early oxidation behavior of Si-coated titanium,* Corrosion Science **140** *(2018) 297–306.*

[203] *N. H. Gunda and A. Van der Ven, First-principles insights on phase stability of titanium interstitial alloys,* Physical Review Materials **2** *(2018), no. 8 083602.*

[204] *H. H. Wu and D. R. Trinkle, Direct diffusion through interpenetrating networks: Oxygen in titanium,* Physical review letters **107** *(2011), no. 4 045504.*

[205] *N. H. Gunda, C. G. Levi, and A. Van der Ven, Investigating the electronic origins of the repulsion between substitutional and interstitial solutes in hcp Ti,* Physical Review Materials **5** *(2021), no. 7 073604.*

[206] *J. Chen, Y. Tang, F. Liu, J. Shu, Y. Liu, Z. Dong, and Y. Liu, Alloying effects on the oxygen diffusion in Nb alloys: A first-principles study,* Metallurgical and Materials Transactions A **52** *(2021) 270–283.*

[207] *L. Zhu, H. Wang, Q.-M. Hu, G. J. Ackland, and R. Yang, Trapping of interstitial defects: filling the gap between the experimental measurements and DFT calculations,* Journal of Physics: Condensed Matter **25** *(2013), no. 43 435402.*

[208] *N. E. Prasad and R. J. Wanhill,* Aerospace materials and material technologies*, vol. 1. Springer, 2017.*

[209] *J. Shu, Z. Dong, C. Zheng, A. Sun, S. Yang, T. Han, Y. Liu, Z. Wang, S. Wang, and Y. Liu, High-throughput experiment-assisted study of the alloying effects on oxidation of Nb-based alloys,* Corrosion Science **204** *(2022) 110383.*

[210] *R. F. Bader, Atoms in molecules,* Accounts of chemical research **18** *(1985), no. 1 9–15.*

[211] *R. F. Bader, A quantum theory of molecular structure and its applications,* Chemical Reviews **91** *(1991), no. 5 893–928.*

[212] *R. F. Bader, M. T. Carroll, J. R. Cheeseman, and C. Chang, Properties of atoms in molecules: atomic volumes,* Journal of the American Chemical Society **109** *(1987), no. 26 7968–7979.*

[213] *J. C. Slater, Atomic radii in crystals,* The Journal of Chemical Physics **41** *(1964), no. 10 3199–3204.*

[214] *C. Frey, R. Silverstein, and T. M. Pollock, A high stability B2-containing refractory multi-principal element alloy,* Acta Materialia **229** *(2022) 117767.*

[215] *A. H. Cottrell and B. A. Bilby, Dislocation theory of yielding and strain ageing of iron,* Proceedings of the Physical Society. Section A **62** *(1949), no. 1 49.*

[216] *M. Kuzmina, M. Herbig, D. Ponge, S. Sandlöbes, and D. Raabe, Linear complexions: Confined chemical and structural states at dislocations,* Science **349** *(2015), no. 6252 1080–1083.*

[217] *V. Turlo and T. J. Rupert, Interdependent linear complexion structure and dislocation mechanics in Fe-Ni,* Crystals **10** *(2020), no. 12 1128.*

[218] *V. Turlo and T. J. Rupert, Linear complexions: Metastable phase formation and coexistence at dislocations,* Physical Review Letters **122** *(2019), no. 12 126102.*

[219] V. Turlo and T. J. Rupert, Prediction of a wide variety of linear complexions in face centered cubic alloys, Acta Materialia **185** *(2020) 129–141.*

[220] S. Korte-Kerzel, T. Hickel, L. Huber, D. Raabe, S. Sandlöbes-Haut, M. Todorova, and J. Neugebauer, Defect phases–thermodynamics and impact on material properties, International Materials Reviews **67** *(2022), no. 1 89–117.*

[221] L. T. Fey, C. Reynolds, A. Hunter, and I. J. Beyerlein, Phase-field modeling of dislocation-interstitial interactions, Journal of the Mechanics and Physics of Solids *(2023) 105370.*

[222] V. Vitek, Intrinsic stacking faults in body-centred cubic crystals, Philosophical Magazine **18** *(1968), no. 154 773–786.*

[223] A. Van der Ven and G. Ceder, The thermodynamics of decohesion, Acta Materialia **52** *(2004), no. 5 1223–1235.*

[224] J. L. Kaufman, J. Vinckevičiūtė, S. Krishna Kolli, J. Gabriel Goiri, and A. Van der Ven, Understanding intercalation compounds for sodium-ion batteries and beyond, Philosophical Transactions of the Royal Society A **377** *(2019), no. 2152 20190020.*

[225] J. G. Goiri, MultiShifter, 2023. https://github.com/goirijo/multishifter.

[226] J. G. Goiri and A. Van der Ven, MultiShifter: Software to generate structural models of extended two-dimensional defects in 3D and 2D crystals, Computational Materials Science **191** *(2021) 110310.*

[227] J. H. Rose, J. Ferrante, and J. R. Smith, Universal binding energy curves for metals and bimetallic interfaces, Physical Review Letters **47** *(1981), no. 9 675.*

[228] J. H. Rose, J. R. Smith, and J. Ferrante, Universal features of bonding in metals, Physical review B **28** *(1983), no. 4 1835.*

[229] R. A. Enrique and A. Van der Ven, Decohesion models informed by first-principles calculations: The ab initio tensile test, Journal of the Mechanics and Physics of Solids **107** *(2017) 494–508.*

[230] R. A. Enrique and A. Van der Ven, Traction curves for the decohesion of covalent crystals, Applied Physics Letters **110** *(2017), no. 2 021910.*

[231] J. Van Landuyt and S. Amelinckx, On the generation mechanism for shear planes in shear structures, Journal of Solid State Chemistry **6** *(1973), no. 2 222–229.*

[232] J. Cao, J. Xia, X. Li, Y. Li, P. Liu, L. Tian, P. Qiao, C. Liu, Y. Wang, and X. Meng, Defect-mediated growth of crystallographic shear plane, Small *(2023) 2302365.*

[233] A. A. Voskanyan and A. Navrotsky, Shear pleasure: The structure, formation, and thermodynamics of crystallographic shear phases, Annual Review of Materials Research **51** *(2021).*